Spin-Orbit Torque Metrology

A Dissertation

Presented to the Faculty of the Graduate School

of Cornell University

in Partial Fulfillment of the Requirements for the Degree

of

Doctor of Philosophy

Saba Karimeddiny

December 1, 2021

Spin-Orbit Torque Metrology

Saba Karimeddiny, Ph.D.

Cornell University 2021

This dissertation will discuss the recent progress that has been made in the metrology of spin-orbit torques (SOTs). Metrology, the study of measurement(s), is an effective epistemological strategy to improve our understanding of spin-orbit torques, magnetic dynamics, and the additional physical processes that "pervade" the measurements, but can prove to be quite interesting in their own right. In this dissertation, we will focus on three measurements techniques:

1. The lineshape analysis of spin-torque ferromagnetic resonance (ST-FMR), which has been known to be susceptible to other artifact signals that are resonant, such as spin pumping and resonant heating. We find that we are able to cancel these artifacts by performing the measurement in a Hall geometry and exploiting differences in the lineshape symmetries between artifacts and the desired signals generated from SOTs.

2. The linewidth analysis of ST-FMR, which has been shown to give inflated, unrealistic results that disagree with all corroborating measurement techniques in many cases. This turns out to be caused by interface-localized resonant magnetic dynamics that nearly coincide with the bulk resonance. Although small volumetrically, these interfacial dynamics can significantly affect the sensitive measurement of the linewidth modulation by dc current. We find that we are able to minimize the spurious effect of the interfacial magnetic layer through a systematic data analysis prescription.

3. Second-harmonic Hall performed on perpendicularly-magnetized devices, where consideration of the planar Hall magnetoresistance in the measurements of SOTs has resulted in unreasonable and sometimes unphysical

quantifications. Previous results have suggested that ignoring contributions from the planar Hall magnetoresistance brings this technique into agreement with corroborating measurements, and we verify this is a sound procedure by measuring the same magnetic dynamics optically, for the first time.

Biographical Sketch

Saba Karimeddiny grew up in Natick, MA and attended Natick High School. He attended the University of Massachusetts, Amherst where in 2017 he graduated with a B.S. in Physics, a second B.S. in Mathematics, and summa cum laude distinction. He began graduate school at Cornell University in the Fall of 2017 and formally joined Dan Ralph's group in the summer of 2018. He received his M.S. in physics from Cornell University in 2020.

To my parents,

for their courage in immigrating to the USA to ensure a brighter future,

for their constant love and unflinching support.

Acknowledgements

Dan Ralph – for his supervision, insight, and mentorship in teaching me how to be a professional scientist.

Joseph Mittelstaedt – for the frequent, helpful discussions, particularly when it came to coding. For working together with me to figure out what was going on in this field when we both first joined the group.

Kelly Luo – for teaching me how to do optics and helping build the Sagnac interferometer.

Greg Stiehl – for his early mentorship and instructive scientific discussions.

Neal Reynolds – for his mentorship, particularly in teaching me how to do various measurements.

Contents

Introduction

Metrology is the *study* of measurements. It turns out that many of the common measurement techniques we use to quantify SOTs give results that disagree with one another, and depending on the practitioner, can give results that disagree with themselves. These discrepancies are not rarities. In fact they occur frequently and serve as the underpinning motivation for this whole thesis.

As the field of SOTs has progressed, standard measurement techniques have persisted and have been used to measure various material systems, and discrepancies are often chalked up to material complications. However, similar measurement discrepancies exist even for simple, bread-and-butter SOT material systems (e.g. Pt/Py, where, in this work, Py = $Ni_{81}Fe_{19}$ – a very-weakly-magnetoelastic alloy). To re-litigate these measurements and understand the cause of these measurement discrepancies, our studies will focus on standard, widely-studied heavy metal/ferromagnet (HM/FM) bilayers where the understanding and interpretation of measurement results ought to be simple. We will see that measurement results are complicated, even in these systems.

In Chapter 1, we will see that long-known artifacts (spin pumping and resonant heating) affect the *most common* measurement technique used to quantify SOTs in in-plane-magnetized heterostructures in various HM/FM systems: spin-torque ferromagnetic resonance. These artifacts are particularly pronounced when the HM or FM thickness is large. In Chapter 2, we will see that improper data analysis and unintended experimenter bias can have a huge effect on the quantification of SOTs in another very common measurement technique used to quantify SOTs in in-plane-magnetized heterostructures in various HM/FM systems: dc-biased spin-torque ferromagnetic resonance. This bias and discrepancy is abated by following a systematic data analysis framework that we outline. In Chapter 3, we see the very surprising result that the planar Hall magnetoresistance seems to not contribute to the quantifi-

cation of SOTs in the *most common* measurement technique used to quantify SOTs in out-of-plane-magnetized heterostructures in various HM/FM systems: the second-harmonic Hall method. Our suggestion is to ignore the planar Hall magnetoresistance when quantifying the SOT, suggesting that the planar Hall effect manifests differently when the magnetization is tilted with a magnetic field vs. a SOT. This challenges our conventional understanding of the planar Hall magnetoresistance, altogether.

Chapter 0

Preface

In this chapter, we will review a variety of topics ranging from the motivation for my work and thesis to the working details of certain laboratory instrumentation. There is no unifying theme of this chapter – it will be a medley of information that will serve readers from a variety of backgrounds.

0.1 Computer Memory

In this section, we will broadly frame the goal of SOT studies: to use SOTs to create efficient magnetic random access memory (MRAM), a technology that would store information as a remnant magnetic configuration. To supplant current memory technologies and meet future industry demand, MRAM should be fast, non-volatile, and require little power to operate; magnetic heterostructures harnessing SOTs would check all of these boxes.

The Von Neumann computing paradigm has necessitated the engineering of a memory hierarchy that increases the speed of the computation pipeline while preserving information integrity. This hierarchy, shown in Fig. 0.1, connects the (hopefully non-volatile) human user to the CPU through storage media of increasing read/write speed and of increasing volatility.

The speed of MRAM technologies gives it the potential to supplant the current DRAM and SRAM architectures, providing a fast yet non-volatile al-

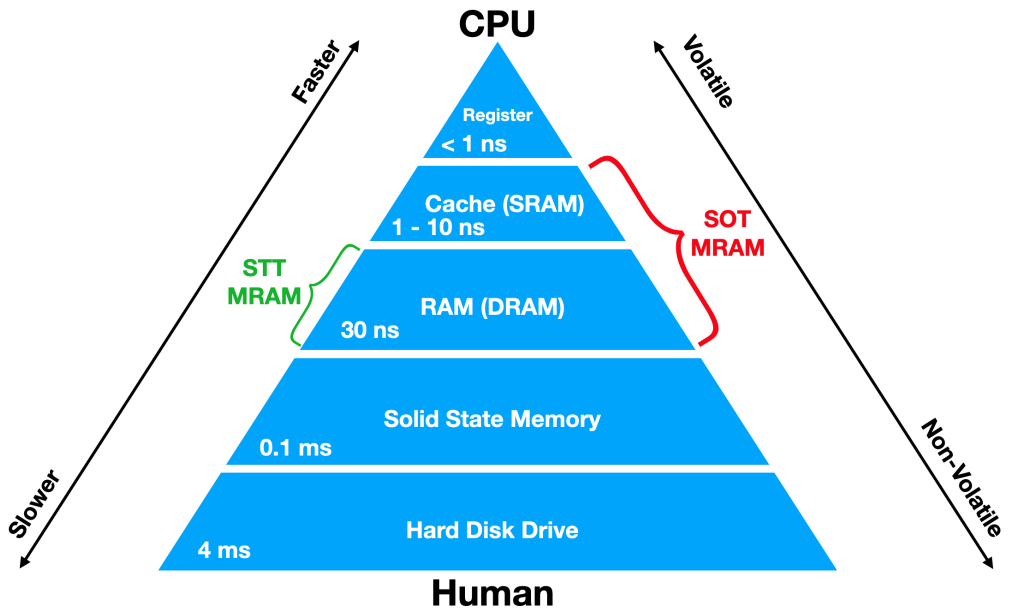

Figure 0.1: Hierarchy of the current paradigm of computing memory.

ternative. The non-volatility is quite important here because the DRAM and SRAM volatility reduces computing efficiency. DRAM and SRAM both require power to retain their information. In the case of DRAM, which stores information in a capacitor, the capacitor charge leaks off into the circuit slowly, so a "refresh" write operation is required for each bit. This of course takes additional power and some time (every 64 ms or less) to perform. SRAM, which stores data in a multi-transistor latch circuit, does not require a refresh, but it does require a constant power input to keep the transistors gated and current flowing. Additionally, SRAM requires multiple transistors so its on-chip footprint is around 0.06 μm^2 as of 2019 [1], quite large even after decades of development. MRAM technology is available from Intel at a density of less than 0.05 μm^2 even in the early stage of its development.

0.2 How do you solve a problem like...the LLGS equation?

In this section we will show the basic recipe for solving the Landau-Lifshitz-Gilbert-Slonczewski (LLGS) equation and the basic results that one should end

up with. This equation is the fundamental differential equation in SOT studies that one ends up frequently solving under various conditions. First, we will do some setup. The system under consideration will be a thin-film magnetic heterostructure. The film extends in the XY-plane and the Z-direction is out-of-plane. We can write the LLGS equation that we'd like to solve as

$$\frac{d\hat{\mathbf{m}}}{dt} = -\gamma\hat{\mathbf{m}} \times \left[\mathbf{H} + \mu_0 M_{\text{eff}}(\hat{\mathbf{m}} \cdot \hat{\mathbf{Z}})\hat{\mathbf{Z}}\right] + \alpha\frac{d\hat{\mathbf{m}}}{dt} + \boldsymbol{\tau} \tag{0.1}$$

where $\gamma = 2\mu_B/\hbar$ is the gyromagnetic ratio (I will let it be $\approx$ 28 GHz/T throughout this document); $\hat{\mathbf{m}}$ is the normalized magnetic moment; $\mathbf{H}$ is the applied magnetic field; α is the Gilbert damping that ensures that the magnetic moment relaxes to the direction of applied field; M_{eff} is the saturation magnetization minus any out-of-plane anisotropy: $\mu_0 M_{\text{eff}} = \mu_0 M_s - 2K_\perp/M_s$; and $\boldsymbol{\tau}$ is some arbitrary torque that is applied to the system that could originate from microwave fields due to a coplanar waveguide in a ferromagnetic resonance (FMR) measurement or damping-like and field-like torques generated from a spin source layer adjacent to the magnetic layer in a ST-FMR measurement. The sign of M_{eff}, which is normally a large number compared to the magnitude of the external field $|\mathbf{H}|$, will determine whether the magnetization prefers to be in-plane or out of plane. With my definition, positive M_{eff} will mean that the magnetization likes to remain in-plane, and we will assume that $M_{\text{eff}} > 0$ in the following. Furthermore, we will also assume that $\mathbf{H}$ lies in the XY-plane and that the within-plane anisotropy is sufficiently weak (we haven't even included a term to account for that) such that $\hat{\mathbf{m}} \parallel \mathbf{H}$ in equilibrium. In the presence of non-equilibrium excitations of the magnetization that are applied at a driving frequency of ω (e.g. by the application of microwave torques $\boldsymbol{\tau} = \boldsymbol{\tau}e^{i\omega t}$), we write the magnetic moment as

$$\hat{\mathbf{m}} = \hat{\mathbf{m}}^0 + \delta\hat{\mathbf{m}}e^{-i\omega t} \tag{0.2}$$

where $\hat{\mathbf{m}}^0 \parallel \mathbf{H}$ is the equilibrium magnetic moment and the $\delta\hat{\mathbf{m}}e^{i\omega t}$ describes (very small) oscillations about that equilibrium at a frequency ω. We want to solve for $\delta\hat{\mathbf{m}}$. We plug this into Eq. (0.1) to get

$$\begin{aligned} -i\omega\delta\hat{\mathbf{m}}e^{-i\omega t} =& -\gamma(\hat{\mathbf{m}}^0 + \delta\hat{\mathbf{m}}e^{-i\omega t}) \times \mathbf{H} + \alpha\left[(\hat{\mathbf{m}}^0 + \delta\hat{\mathbf{m}}e^{-i\omega t}) \times -i\omega\delta\hat{\mathbf{m}}e^{i\omega t}\right] \\ &+ \gamma\mu_0 M_{\text{eff}}((\hat{\mathbf{m}}^0 + \delta\hat{\mathbf{m}}e^{-i\omega t}) \cdot \hat{\mathbf{Z}})((\hat{\mathbf{m}}^0 + \delta\hat{\mathbf{m}}e^{-i\omega t}) \times \hat{\mathbf{Z}}) + \boldsymbol{\tau}e^{-i\omega t}. \end{aligned} \tag{0.3}$$

Already, a few simplifications can be made. First, $\delta\hat{\mathbf{m}}$ is very small so its higher-order terms are negligible. Second, we assumed that $\hat{\mathbf{m}}^0$ lies in the XY-plane so $\hat{\mathbf{m}}^0 \cdot \hat{\mathbf{Z}} = 0$. Lastly, we have assumed no within-plane anisotropy so $\hat{\mathbf{m}}^0 \parallel \mathbf{H}$, which means that $\hat{\mathbf{m}}^0 \times \mathbf{H} = 0$. We have

$$\begin{aligned} -i\omega\delta\hat{\mathbf{m}}e^{-i\omega t} =& -\gamma\delta\hat{\mathbf{m}}e^{-i\omega t} \times \mathbf{H} + \alpha\left[\hat{\mathbf{m}}^0 \times -i\omega\delta\hat{\mathbf{m}}e^{-i\omega t}\right] \\ &+ \gamma\mu_0 M_{\text{eff}}(\delta\hat{\mathbf{m}}e^{-i\omega t} \cdot \hat{\mathbf{Z}})(\hat{\mathbf{m}}^0 \times \hat{\mathbf{Z}}) + \boldsymbol{\tau}e^{-i\omega t}. \end{aligned} \tag{0.4}$$

The simplest next step is to just align the coordinate system so that a principal axis, say $\hat{Y}$, such that $\hat{\mathbf{m}}^0 \parallel \mathbf{H} \parallel \hat{Y}$; no generality is sacrificed here. Now we will write down some vectors explicitly

$$\begin{aligned} \hat{\mathbf{m}} = \hat{\mathbf{m}}^0 + \delta\hat{\mathbf{m}}e^{-i\omega t} &= \begin{pmatrix} \delta m_X e^{-i\omega t} \\ \sqrt{1 - \delta m_X^2 e^{-2i\omega t} - \delta m_Z^2 e^{-2i\omega t}} \\ \delta m_Z e^{-i\omega t} \end{pmatrix} = \begin{pmatrix} 0 \\ 1 \\ 0 \end{pmatrix} + \begin{pmatrix} \delta m_X \\ 0 \\ \delta m_Z \end{pmatrix} e^{-i\omega t} \\ \mathbf{H} &= H \begin{pmatrix} 0 \\ 1 \\ 0 \end{pmatrix} \\ \boldsymbol{\tau} &= \begin{pmatrix} \tau_X \\ \tau_Y \\ \tau_Z \end{pmatrix}. \end{aligned} \tag{0.5}$$

The $\hat{\mathbf{m}}$ vector was be simplified by recognizing that $\delta m_X^2, \delta m_Z^2 << 1$. Simply taking the above vectors and rewriting Eq. (0.4) as a matrix equation gives

$$-i\omega e^{-i\omega t}\begin{pmatrix}\delta m_X\\0\\\delta m_Z\end{pmatrix} = -\gamma H e^{-i\omega t}\begin{pmatrix}\delta m_X\\0\\\delta m_Z\end{pmatrix}\times\begin{pmatrix}0\\1\\0\end{pmatrix} + -i\omega\alpha e^{-i\omega t}\begin{pmatrix}0\\1\\0\end{pmatrix}\times\begin{pmatrix}\delta m_X\\0\\\delta m_Z\end{pmatrix}$$
$$+\gamma\mu_0 M_{\text{eff}}\delta m_Z e^{-i\omega t}\begin{pmatrix}0\\1\\0\end{pmatrix}\begin{pmatrix}0\\0\\1\end{pmatrix} + e^{-i\omega t}\begin{pmatrix}\tau_X\\\tau_Y\\\tau_Z\end{pmatrix}. \tag{0.6}$$

Doing the cross products and canceling the common $e^{-i\omega t}$ gives

$$-i\omega\begin{pmatrix}\delta m_X\\0\\\delta m_Z\end{pmatrix} = \begin{pmatrix}\gamma H\delta m_Z + \gamma\mu_0 M_{\text{eff}}\delta m_Z - i\alpha\omega\delta m_Z + \tau_X\\\tau_Y\\-\gamma H\delta m_X + i\alpha\omega\delta m_X + \tau_Z\end{pmatrix}. \tag{0.7}$$

We rewrite this as a matrix equation

$$-i\omega I_2\delta\hat{\mathbf{m}} = M\delta\hat{\mathbf{m}} + \boldsymbol{\tau} =$$
$$-i\omega\begin{pmatrix}1&0\\0&1\end{pmatrix}\begin{pmatrix}\delta m_X\\\delta m_Z\end{pmatrix} = \begin{pmatrix}0&\gamma H + \gamma\mu_0 M_{\text{eff}} - i\alpha\omega\\-\gamma H + i\alpha\omega&0\end{pmatrix}\begin{pmatrix}\delta m_X\\\delta m_Z\end{pmatrix} + \begin{pmatrix}\tau_X\\\tau_Z\end{pmatrix}. \tag{0.8}$$

We will simplify this equation a little bit by defining some new variables. Let $\omega_1 = \gamma H$ and $\omega_2 = \gamma(H + \mu_0 M_{\text{eff}})$. The equation becomes

$$-i\omega\begin{pmatrix}1&0\\0&1\end{pmatrix}\begin{pmatrix}\delta m_X\\\delta m_Z\end{pmatrix} = \begin{pmatrix}0&\omega_2 - i\alpha\omega\\-\omega_1 + i\alpha\omega&0\end{pmatrix}\begin{pmatrix}\delta m_X\\\delta m_Z\end{pmatrix} + \begin{pmatrix}\tau_X\\\tau_Z\end{pmatrix}. \tag{0.9}$$

One simple thing to do at this stage is to just ignore the effect of the torques and the damping and solve the system to find the resonance frequencies. To do

this, we set $\boldsymbol{\tau} = \alpha = 0$ and calculate the determinant $|M + i\omega I_2| = 0$ to get

$$-i\omega_0 = \pm\gamma\sqrt{-\omega_1\omega_2}, \tag{0.10}$$

but both H and M_{eff} are greater than zero, so $\omega_{1(2)} > 0$ and the square root will always yield an imaginary value and thus (ignoring the negative frequency branch)

$$\omega_0 = \gamma\sqrt{H\,(H + M_{\text{eff}})}. \tag{0.11}$$

This is the Kittel equation [2]. Beginning at Eq. (0.9), we (Mathematica) will now just solve it for δm_X and δm_Z

$$\delta m_X = -\frac{\tau_Z\omega_2 - i\omega(\alpha\tau_Z + \tau_X)}{(\alpha^2+1)\,\omega^2 + i\alpha\omega(\omega_1+\omega_2) - \omega_1\omega_2} \tag{0.12}$$

$$\delta m_Z = \frac{\tau_X\omega_1 - i\omega(\alpha\tau_X - \tau_Z)}{(\alpha^2+1)\,\omega^2 + i\alpha\omega(\omega_1+\omega_2) - \omega_1\omega_2} \tag{0.13}$$

The time dependence of the original trial solution was $e^{-i\omega t}$ for ease of algebra, but only the real part of the solution is meaningful so we will take the real part of the above.

$$\delta m_X = \frac{\alpha\omega^2\omega_1(\alpha\tau_Z + \tau_X) + \omega^2\omega_2(\alpha\tau_X - \tau_Z) + \tau_Z\omega_1\omega_2^2}{\omega^2\left(\alpha^2\left(\omega_1^2+\omega_2^2\right) - 2\omega_1\omega_2\right) + \left(\alpha^2+1\right)^2\omega^4 + \omega_1^2\omega_2^2} \tag{0.14}$$

$$\delta m_Z = \frac{-\tau_X\omega_2\left(\alpha^2\omega^2 + \omega_1^2\right) + \alpha\tau_Z\omega^2(\omega_1+\omega_2) + \tau_X\omega^2\omega_1}{\omega^2\left(\alpha^2\left(\omega_1^2+\omega_2^2\right) - 2\omega_1\omega_2\right) + \left(\alpha^2+1\right)^2\omega^4 + \omega_1^2\omega_2^2} \tag{0.15}$$

In most ferromagnets, α is quite small so we will ignore higher order terms in α

$$\delta m_X = \frac{\alpha\omega^2\omega_1\tau_X + \omega^2\omega_2(\alpha\tau_X - \tau_Z) + \tau_Z\omega_1\omega_2^2}{\omega^2\left(\alpha^2\left(\omega_1^2+\omega_2^2\right) - 2\omega_1\omega_2\right) + \left(2\alpha^2+1\right)\omega^4 + \omega_1^2\omega_2^2} \tag{0.16}$$

$$\delta m_Z = \frac{-\tau_X\omega_2\omega_1^2 + \alpha\tau_Z\omega^2(\omega_1+\omega_2) + \tau_X\omega^2\omega_1}{\omega^2\left(\alpha^2\left(\omega_1^2+\omega_2^2\right) - 2\omega_1\omega_2\right) + \left(2\alpha^2+1\right)\omega^4 + \omega_1^2\omega_2^2}. \tag{0.17}$$

Remembering that $\omega_0^2 = \omega_1\omega_2$ and defining $\omega^+ = \omega_1 + \omega_2$, we can simplify to

$$\delta m_X = \frac{\alpha\omega^2\omega^+\tau_X + \omega_2(\omega^2 - \omega_0^2)\tau_Z}{(\omega^2 - \omega_0^2)^2 + \alpha^2\omega^2(\omega^+)^2} \tag{0.18}$$

$$\delta m_Z = \frac{\alpha\omega^2\omega^+\tau_Z - \omega_1(\omega^2 - \omega_0^2)\tau_X}{(\omega^2 - \omega_0^2)^2 + \alpha^2\omega^2(\omega^+)^2}. \tag{0.19}$$

0.2.1 Now the Antiferromagnets

In an collinear antiferromagnet, magnetism is carried by two lattices that interact with exchange to keep their respective magnetic moments antiparallel. We model the antiferromagnet explicitly as two lattices that are coupled via exchange using a two-lattice LLG model:

$$\frac{d\hat{\mathbf{m}}_{A(B)}}{dt} = -\gamma\hat{\mathbf{m}}_{A(B)} \times \Big(\mathbf{H} - H_E\hat{\mathbf{m}}_{B(A)} - \mu_0 M_{\text{eff}}(\hat{\mathbf{m}}_{A(B)} \cdot \hat{\mathbf{Z}})\hat{\mathbf{Z}}\Big) \tag{0.20}$$

where A and B are the two sublattices and H_E is the effective (mean-field) exchange field felt by one lattice due to the moment of the other. Again we expand $\hat{\mathbf{m}}$ as the sum of equilibrium and oscillatory components

$$\hat{\mathbf{m}}_{A(B)} = \hat{\mathbf{m}}^0_{A(B)} + \delta\hat{\mathbf{m}}_{A(B)}e^{-i\omega t}. \tag{0.21}$$

We will also let $\mathbf{H} \parallel \hat{y}$. Plugging in, we get

$$\begin{aligned} -i\omega\delta\hat{\mathbf{m}}_{A(B)}e^{-i\omega t} = &-\gamma(\hat{\mathbf{m}}^0_{A(B)} + \delta\hat{\mathbf{m}}_{A(B)}e^{-i\omega t}) \times \big[\mathbf{H} - H_E(\hat{\mathbf{m}}^0_{B(A)} + \delta\hat{\mathbf{m}}_{B(A)}e^{-i\omega t}) - \\ &\mu_0 M_{\text{eff}}((\hat{\mathbf{m}}^0_{A(B)} + \delta\hat{\mathbf{m}}_{A(B)}e^{-i\omega t}) \cdot \hat{\mathbf{Z}})\hat{\mathbf{Z}}\big]. \end{aligned} \tag{0.22}$$

We will simply multiply the terms through

$$\begin{aligned}-i\omega\delta\hat{\mathbf{m}}_{A(B)}e^{-i\omega t} = -\gamma(&\hat{\mathbf{m}}^0_{A(B)}\times\mathbf{H} - H_E(\hat{\mathbf{m}}^0_{A(B)}\times\hat{\mathbf{m}}^0_{B(A)} + \hat{\mathbf{m}}^0_{A(B)}\times\delta\hat{\mathbf{m}}_{B(A)}e^{-i\omega t})\\ &-\mu_0 M_{\text{eff}}((\hat{\mathbf{m}}^0_{A(B)} + \delta\hat{\mathbf{m}}_{A(B)}e^{-i\omega t})\cdot\hat{\mathbf{Z}})(\hat{\mathbf{m}}^0_{A(B)}\times\hat{\mathbf{Z}})\\ &+\delta\hat{\mathbf{m}}_{A(B)}e^{-i\omega t}\times\mathbf{H}\\ &-H_E(\delta\hat{\mathbf{m}}_{A(B)}e^{-i\omega t}\times\hat{\mathbf{m}}^0_{B(A)} + \delta\hat{\mathbf{m}}_{A(B)}e^{-i\omega t}\times\delta\hat{\mathbf{m}}_{B(A)}e^{-i\omega t})\\ &-\mu_0 M_{\text{eff}}((\hat{\mathbf{m}}^0_{A(B)} + \delta\hat{\mathbf{m}}_{A(B)}e^{-i\omega t})\cdot\hat{\mathbf{Z}})(\delta\hat{\mathbf{m}}_{A(B)}e^{-i\omega t}\times\hat{\mathbf{Z}}))\end{aligned} \tag{0.23}$$

We will ignore the small terms, keeping only terms that are linear in $\delta\hat{\mathbf{m}}_{A(B)}$. We will also make some simplifications, assuming that $\hat{\mathbf{m}}_{A(B)}$ lies with the XY-plane

$$\begin{aligned}-i\omega\delta\hat{\mathbf{m}}_{A(B)}e^{-i\omega t} = -\gamma(&\hat{\mathbf{m}}^0_{A(B)}\times\mathbf{H} - H_E(\hat{\mathbf{m}}^0_{A(B)}\times\hat{\mathbf{m}}^0_{B(A)} + \hat{\mathbf{m}}^0_{A(B)}\times\delta\hat{\mathbf{m}}_{B(A)}e^{-i\omega t})\\ &-\mu_0 M_{\text{eff}}(\delta\hat{\mathbf{m}}_{A(B)}e^{-i\omega t}\cdot\hat{\mathbf{Z}})(\hat{\mathbf{m}}^0_{A(B)}\times\hat{\mathbf{Z}})\\ &+\delta\hat{\mathbf{m}}_{A(B)}e^{-i\omega t}\times\mathbf{H} - H_E(\delta\hat{\mathbf{m}}_{A(B)}e^{-i\omega t}\times\hat{\mathbf{m}}^0_{B(A)}))\end{aligned} \tag{0.24}$$

Now we are a bit stuck. In the equation above, there are some terms that are not oscillatory, which would make the rest of the derivation quite challenging. The solution is to invoke a property of antiferromagnets: that when a strong enough external field is applied the moments of the two sublattices "flop" to be aligned perpendicular to the external field but still almost antiparallel to one another. This is called a "spin-flop." After this occurs, the external magnetic field cants the moments of the two sublattices to have a components along the field, which creates a net magnetization in the system. By minimizing the free energy, we can express this cant angle, ϕ, as $\sin\phi = H/2H_E$ [3]. Thus assuming the spins have flopped already and are being canted by the external field, the

following is true [4]

$$\hat{\mathbf{m}}^0_{A(B)} \times \mathbf{H} - H_E \hat{\mathbf{m}}^0_{A(B)} \times \hat{\mathbf{m}}^0_{B(A)} = 0. \tag{0.25}$$

This conveniently cancels all of the non-oscillatory terms in the expression leaving us with

$$\begin{aligned} -i\omega\delta\hat{\mathbf{m}}_{A(B)}e^{-i\omega t} = -\gamma(&-H_E\hat{\mathbf{m}}^0_{A(B)} \times \delta\hat{\mathbf{m}}_{B(A)}e^{-i\omega t} \\ &-\mu_0 M_{\text{eff}}(\delta\hat{\mathbf{m}}_{A(B)}e^{-i\omega t} \cdot \hat{\mathbf{Z}})(\hat{\mathbf{m}}^0_{A(B)} \times \hat{\mathbf{Z}}) \\ &+\delta\hat{\mathbf{m}}_{A(B)}e^{-i\omega t} \times \mathbf{H} - H_E(\delta\hat{\mathbf{m}}_{A(B)}e^{-i\omega t} \times \hat{\mathbf{m}}^0_{B(A)})). \end{aligned} \tag{0.26}$$

Now we will define a new effective field

$$\mathbf{H}_{\text{eff}} = \mathbf{H} - H_E\hat{\mathbf{m}}^0_{B(A)} \tag{0.27}$$

$$\implies \mathbf{H}_{\text{eff}} = H_E\hat{\mathbf{m}}^0_{A(B)} \text{ and } \delta\hat{\mathbf{m}}_{A(B)}e^{-i\omega t} \times \mathbf{H}_{\text{eff}} = -H_{\text{eff}}\hat{\mathbf{m}}^0_{A(B)} \times \delta\hat{\mathbf{m}}_{A(B)}e^{-i\omega t}. \tag{0.28}$$

We now have the much simpler expression

$$\begin{aligned} -i\omega\delta\hat{\mathbf{m}}_{A(B)}e^{-i\omega t} = -\gamma(&-H_E\hat{\mathbf{m}}^0_{A(B)} \times \delta\hat{\mathbf{m}}_{B(A)}e^{-i\omega t} \\ &-\mu_0 M_{\text{eff}}(\delta\hat{\mathbf{m}}_{A(B)}e^{-i\omega t} \cdot \hat{\mathbf{Z}})(\hat{\mathbf{m}}^0_{A(B)} \times \hat{\mathbf{Z}}) \\ &-H_{\text{eff}}\hat{\mathbf{m}}^0_{A(B)} \times \delta\hat{\mathbf{m}}_{A(B)}e^{-i\omega t}), \end{aligned} \tag{0.29}$$

which through factoring and canceling the common $e^{-i\omega t}$ simplifies to

$$-i\omega\delta\hat{\mathbf{m}}_{A(B)} = \gamma\hat{\mathbf{m}}^0_{A(B)} \times (H_{\text{eff}}\delta\hat{\mathbf{m}}_{A(B)} + H_E\delta\hat{\mathbf{m}}_{B(A)} + \mu_0 M_{\text{eff}}(\delta\hat{\mathbf{m}}_{A(B)} \cdot \hat{\mathbf{Z}})\hat{\mathbf{Z}}). \tag{0.30}$$

At this point, it is convenient to write down the vectors explicitly and solve the equation

$$\hat{\mathbf{m}}^0_{A(B)} = \begin{pmatrix} \pm\cos\phi \\ \sin\phi \\ 0 \end{pmatrix} \tag{0.31}$$

$$\delta\hat{\mathbf{m}}_{A(B)} = \begin{pmatrix} \delta m^x_{A(B)} \\ \delta m^y_{A(B)} \\ \delta m^z_{A(B)} \end{pmatrix} \tag{0.32}$$

$$\mathbf{H} = \begin{pmatrix} 0 \\ H \\ 0 \end{pmatrix}, \tag{0.33}$$

where the $\pm$ in the $\hat{\mathbf{m}}^0$ expression accounts for sublattice A and B respectively. We will plug these in and rewrite as a matrix equation like so

$$M \cdot \delta\hat{\mathbf{m}} = 0. \tag{0.34}$$

To find the dispersion of this system, we will set $\det[M] = 0$ and solve to get

$$\omega_1 = \gamma\sqrt{2H_E M_s\left(1 - \frac{H^2}{4H_E^2}\right)} \tag{0.35}$$

$$\omega_2 = \gamma H\sqrt{\frac{M_s + 2H_E}{2H_E}} \tag{0.36}$$

0.2.2 An Antiferromagnet (AF) with anisotropy and the hard axis along external field

We will start with the two-lattice LLG equation again, but with an added hard-axis, uniaxial anisotropy within the XY-plane and along the $\hat{\mathbf{k}}$-direction i.e. the

magnetic moment does *not* want to lie along $\hat{\mathbf{k}}$

$$\frac{d\hat{\mathbf{m}}_{A(B)}}{dt} = -\gamma\hat{\mathbf{m}}_{A(B)} \times (\mathbf{H} - H_E\hat{\mathbf{m}}_{B(A)} - M_s(\hat{\mathbf{m}}_{A(B)} \cdot \hat{\mathbf{Z}})\hat{\mathbf{Z}} - H_A(\hat{\mathbf{m}}_{A(B)} \cdot \hat{\mathbf{k}})\hat{\mathbf{k}}). \tag{0.37}$$

In this specific case, we will let $\hat{\mathbf{k}} \parallel \mathbf{H}$ and the same assumptions as in the last section

$$\hat{\mathbf{m}}_{A(B)} = \hat{\mathbf{m}}^0_{A(B)} + \delta\hat{\mathbf{m}}_{A(B)}e^{-i\omega t} \tag{0.38}$$

$$\mathbf{H} \parallel \hat{y}. \tag{0.39}$$

Plugging these in, we have

$$\begin{aligned} -i\omega\delta\hat{\mathbf{m}}_{A(B)}e^{-i\omega t} = -\gamma(\hat{\mathbf{m}}^0_{A(B)} + \delta\hat{\mathbf{m}}_{A(B)}e^{-i\omega t}) \times (\mathbf{H} - H_E(\hat{\mathbf{m}}^0_{B(A)} + \delta\hat{\mathbf{m}}_{B(A)}e^{-i\omega t}) \\ -M_s((\hat{\mathbf{m}}^0_{A(B)} + \delta\hat{\mathbf{m}}_{A(B)}e^{-i\omega t}) \cdot \hat{\mathbf{Z}})\hat{\mathbf{Z}} \\ -H_A((\hat{\mathbf{m}}^0_{A(B)} + \delta\hat{\mathbf{m}}_{A(B)}e^{-i\omega t}) \cdot \hat{\mathbf{k}})\hat{\mathbf{k}}). \end{aligned} \tag{0.40}$$

Multiplying through

$$\begin{aligned} -i\omega\delta\hat{\mathbf{m}}_{A(B)}e^{-i\omega t} = -\gamma(\hat{\mathbf{m}}^0_{A(B)} \times \mathbf{H} - H_E(\hat{\mathbf{m}}^0_{A(B)} \times \hat{\mathbf{m}}^0_{B(A)} + \hat{\mathbf{m}}^0_{A(B)} \times \delta\hat{\mathbf{m}}_{B(A)}e^{-i\omega t}) \\ -M_s((\hat{\mathbf{m}}^0_{A(B)} + \delta\hat{\mathbf{m}}_{A(B)}e^{-i\omega t}) \cdot \hat{\mathbf{Z}})(\hat{\mathbf{m}}^0_{A(B)} \times \hat{\mathbf{Z}}) \\ -H_A((\hat{\mathbf{m}}^0_{A(B)} + \delta\hat{\mathbf{m}}_{A(B)}e^{-i\omega t}) \cdot \hat{\mathbf{k}})(\hat{\mathbf{m}}^0_{A(B)} \times \hat{\mathbf{k}}) \\ +\delta\hat{\mathbf{m}}_{A(B)}e^{-i\omega t} \times \mathbf{H} \\ -H_E(\delta\hat{\mathbf{m}}_{A(B)}e^{-i\omega t} \times \hat{\mathbf{m}}^0_{B(A)} + \delta\hat{\mathbf{m}}_{A(B)}e^{-i\omega t} \times \delta\hat{\mathbf{m}}_{B(A)}e^{-i\omega t}) \\ -M_s((\hat{\mathbf{m}}^0_{A(B)} + \delta\hat{\mathbf{m}}_{A(B)}e^{-i\omega t}) \cdot \hat{\mathbf{Z}})(\delta\hat{\mathbf{m}}_{A(B)}e^{-i\omega t} \times \hat{\mathbf{Z}}) \\ -H_A((\hat{\mathbf{m}}^0_{A(B)} + \delta\hat{\mathbf{m}}_{A(B)}e^{-i\omega t}) \cdot \hat{\mathbf{k}})(\delta\hat{\mathbf{m}}_{A(B)}e^{-i\omega t} \times \hat{\mathbf{k}})). \end{aligned} \tag{0.41}$$

Ignoring the small terms

$$
\begin{aligned}
-i\omega\delta\hat{\mathbf{m}}_{A(B)}e^{-i\omega t} = -\gamma(&\hat{\mathbf{m}}^0_{A(B)} \times \mathbf{H} - H_E(\hat{\mathbf{m}}^0_{A(B)} \times \hat{\mathbf{m}}^0_{B(A)} + \hat{\mathbf{m}}^0_{A(B)} \times \delta\hat{\mathbf{m}}_{B(A)}e^{-i\omega t}) \\
&-M_s(\delta\hat{\mathbf{m}}_{A(B)}e^{-i\omega t} \cdot \hat{\mathbf{Z}})(\hat{\mathbf{m}}^0_{A(B)} \times \hat{\mathbf{Z}}) \\
&-H_A((\hat{\mathbf{m}}^0_{A(B)} + \delta\hat{\mathbf{m}}_{A(B)}e^{-i\omega t}) \cdot \hat{\mathbf{k}})(\hat{\mathbf{m}}^0_{A(B)} \times \hat{\mathbf{k}}) \\
&+\delta\hat{\mathbf{m}}_{A(B)}e^{-i\omega t} \times \mathbf{H} - H_E(\delta\hat{\mathbf{m}}_{A(B)}e^{-i\omega t} \times \hat{\mathbf{m}}^0_{B(A)}) \\
&-H_A(\hat{\mathbf{m}}^0_{A(B)} \cdot \hat{\mathbf{k}})(\delta\hat{\mathbf{m}}_{A(B)}e^{-i\omega t} \times \hat{\mathbf{k}})). \qquad (0.42)
\end{aligned}
$$

Again we are stuck and must invoke a similar relation to the last time. Thankfully the non-oscillatory terms cancel with one another because the new cant angle ϕ with anisotropy can be expressed as $\sin\phi = H/(2H_E + H_A)$, so the following is true

$$
\hat{\mathbf{m}}^0_{A(B)} \times \mathbf{H} - H_E\hat{\mathbf{m}}^0_{A(B)} \times \hat{\mathbf{m}}^0_{B(A)} - H_A(\hat{\mathbf{m}}^0_{A(B)} \cdot \hat{\mathbf{k}})(\hat{\mathbf{m}}^0_{A(B)} \times \hat{\mathbf{k}}) = 0. \qquad (0.43)
$$

The non-oscillatory terms are canceled leaving us with

$$
\begin{aligned}
-i\omega\delta\hat{\mathbf{m}}_{A(B)}e^{-i\omega t} = -\gamma(&-H_E(\hat{\mathbf{m}}^0_{A(B)} \times \delta\hat{\mathbf{m}}_{B(A)}e^{-i\omega t}) \\
&-M_s(\delta\hat{\mathbf{m}}_{A(B)}e^{-i\omega t} \cdot \hat{\mathbf{Z}})(\hat{\mathbf{m}}^0_{A(B)} \times \hat{\mathbf{Z}}) \\
&-H_A(\delta\hat{\mathbf{m}}_{A(B)}e^{-i\omega t} \cdot \hat{\mathbf{k}})(\hat{\mathbf{m}}^0_{A(B)} \times \hat{\mathbf{k}}) \\
&+\delta\hat{\mathbf{m}}_{A(B)}e^{-i\omega t} \times \mathbf{H} - H_E(\delta\hat{\mathbf{m}}_{A(B)}e^{-i\omega t} \times \hat{\mathbf{m}}^0_{B(A)}) \\
&-H_A(\hat{\mathbf{m}}^0_{A(B)} \cdot \hat{\mathbf{k}})(\delta\hat{\mathbf{m}}_{A(B)}e^{-i\omega t} \times \hat{\mathbf{k}})). \qquad (0.44)
\end{aligned}
$$

We will write out the vectors explicitly again and begin to solve the equation

$$\hat{\mathbf{m}}^0_{A(B)} = \begin{pmatrix} \pm\cos\phi \\ \sin\phi \\ 0 \end{pmatrix} \tag{0.45}$$

$$\delta\hat{\mathbf{m}}_{A(B)} = \begin{pmatrix} \delta m^x_{A(B)} \\ \delta m^y_{A(B)} \\ \delta m^z_{A(B)} \end{pmatrix} \tag{0.46}$$

$$\mathbf{H} = \begin{pmatrix} 0 \\ H \\ 0 \end{pmatrix} \tag{0.47}$$

$$\hat{\mathbf{k}} = \begin{pmatrix} 0 \\ 1 \\ 0 \end{pmatrix}, \tag{0.48}$$

which we again rewrite as a matrix equation like so

$$M \cdot \delta\hat{\mathbf{m}} = 0. \tag{0.49}$$

Letting $\det[M] = 0$ and solve for ω again

$$\omega_1 = \mathrm{Re}\left[-i\gamma\sqrt{\frac{(H^2(H_A - 2H_E) - H_A(H_A + 2H_E)^2)(2H_E + M_s))}{(H_A + 2H_E)^2}}\right] \tag{0.50}$$

$$\omega_2 = \mathrm{Re}\left[-i\gamma\sqrt{\frac{(H^2 - (H_A + 2H_E)^2)M_s}{H_A + 2H_E}}\right], \tag{0.51}$$

where in this case we explicitly take the real part because the relative magnitudes of the effective fields can affect the real/imaginary components of the resonance frequencies.

0.2.3 An AF with anisotropy and the hard axis perpendicular to the external field

This derivation is similar to the previous, and results in

$$\omega_1 = \mathrm{Re}\left[-i\gamma\sqrt{\frac{(-H_A(H_A-2H_E)^2+H^2(H_A+2H_E))(H_A-2H_E-M_s)}{(H_A-2H_E)^2}}\right] \tag{0.52}$$

$$\omega_2 = \mathrm{Re}\left[-i\gamma\sqrt{\frac{(H^2-(H_A-2H_E)^2(H_A-M_s)}{H_A-2H_E}}\right] \tag{0.53}$$

0.2.4 An AF with anisotropy strong enough such that the external field did not cause a spin flop

If there is strong enough (usually crystalline) anisotropy in an AFM, the external field may be too weak to overcome the anistropy and cause the lattice moments to align perpendicular to the external field in a spin flop. This situation can still be analyzed to find the resonance frequencies, and the derivation is a bit simpler than those above. Again, we will start with the two-lattice LLG equation

$$\frac{d\hat{\mathbf{m}}_{A(B)}}{dt} = -\gamma\hat{\mathbf{m}}_{A(B)}\times(\mathbf{H}-H_E\hat{\mathbf{m}}_{B(A)}-M_s(\hat{\mathbf{m}}_{A(B)}\cdot\hat{\mathbf{Z}})\hat{\mathbf{Z}}-H_A(\hat{\mathbf{m}}_{A(B)}\cdot\hat{\mathbf{k}})\hat{\mathbf{k}}) \tag{0.54}$$

with $\hat{\mathbf{k}}\perp\mathbf{H}$ (recall $\hat{\mathbf{k}}$ is the hard axis). We will make the same initial assumptions as before

$$\hat{\mathbf{m}}_{A(B)} = \hat{\mathbf{m}}^0_{A(B)} + \delta\hat{\mathbf{m}}_{A(B)}e^{-i\omega t} \tag{0.55}$$

$$\mathbf{H}\parallel\hat{y}. \tag{0.56}$$

Plugging this in again we have

$$-i\omega\delta\hat{\mathbf{m}}_{A(B)}e^{-i\omega t} = -\gamma(\hat{\mathbf{m}}^0_{A(B)} + \delta\hat{\mathbf{m}}_{A(B)}e^{-i\omega t}) \times (\mathbf{H} - H_E(\hat{\mathbf{m}}^0_{B(A)} + \delta\hat{\mathbf{m}}_{B(A)}e^{-i\omega t}) - M_s((\hat{\mathbf{m}}^0_{A(B)} + \delta\hat{\mathbf{m}}_{A(B)}e^{-i\omega t}) \cdot \hat{\mathbf{Z}})\hat{\mathbf{Z}} - H_A((\hat{\mathbf{m}}^0_{A(B)} + \delta\hat{\mathbf{m}}_{A(B)}e^{-i\omega t}) \cdot \hat{\mathbf{k}})\hat{\mathbf{k}}), \tag{0.57}$$

but now there is the added assumption that the external field has not caused a spin flop event prior to the measurement, so we have $\hat{\mathbf{m}}^0_{A(B)} \parallel \mathbf{H} \perp \hat{\mathbf{k}}$, which leads to a great deal of simplification when we multiply through

$$\begin{aligned}-i\omega\delta\hat{\mathbf{m}}_{A(B)}e^{-i\omega t} = -\gamma(&- H_E(\hat{\mathbf{m}}^0_{A(B)} \times \delta\hat{\mathbf{m}}_{B(A)}e^{-i\omega t}) \\ &- M_s((\hat{\mathbf{m}}^0_{A(B)} + \delta\hat{\mathbf{m}}_{A(B)}e^{-i\omega t}) \cdot \hat{\mathbf{Z}})(\hat{\mathbf{m}}^0_{A(B)} \times \hat{\mathbf{Z}}) \\ &+ \delta\hat{\mathbf{m}}_{A(B)}e^{-i\omega t} \times \mathbf{H} \\ &- H_E(\delta\hat{\mathbf{m}}_{A(B)}e^{-i\omega t} \times \hat{\mathbf{m}}^0_{B(A)} + \delta\hat{\mathbf{m}}_{A(B)}e^{-i\omega t} \times \delta\hat{\mathbf{m}}_{B(A)}e^{-i\omega t}) \\ &- M_s((\hat{\mathbf{m}}^0_{A(B)} + \delta\hat{\mathbf{m}}_{A(B)}e^{-i\omega t}) \cdot \hat{\mathbf{Z}})(\delta\hat{\mathbf{m}}_{A(B)}e^{-i\omega t} \times \hat{\mathbf{Z}}) \\ &- H_A((\hat{\mathbf{m}}^0_{A(B)} + \delta\hat{\mathbf{m}}_{A(B)}e^{-i\omega t}) \cdot \hat{\mathbf{k}})(\delta\hat{\mathbf{m}}_{A(B)}e^{-i\omega t} \times \hat{\mathbf{k}})).\end{aligned} \tag{0.58}$$

Ignoring the small terms again we have

$$\begin{aligned}-i\omega\delta\hat{\mathbf{m}}_{A(B)}e^{-i\omega t} = -\gamma(&- H_E(\hat{\mathbf{m}}^0_{A(B)} \times \delta\hat{\mathbf{m}}_{B(A)}e^{-i\omega t}) \\ &- M_s((\hat{\mathbf{m}}^0_{A(B)} + \delta\hat{\mathbf{m}}_{A(B)}e^{-i\omega t}) \cdot \hat{\mathbf{Z}})(\hat{\mathbf{m}}^0_{A(B)} \times \hat{\mathbf{Z}}) \\ &+ \delta\hat{\mathbf{m}}_{A(B)}e^{-i\omega t} \times \mathbf{H} - H_E(\delta\hat{\mathbf{m}}_{A(B)}e^{-i\omega t} \times \hat{\mathbf{m}}^0_{B(A)}) \\ &- M_s(\hat{\mathbf{m}}^0_{A(B)} \cdot \hat{\mathbf{Z}})(\delta\hat{\mathbf{m}}_{A(B)}e^{-i\omega t} \times \hat{\mathbf{Z}}) \\ &- H_A(\hat{\mathbf{m}}^0_{A(B)} \cdot \hat{\mathbf{k}})(\delta\hat{\mathbf{m}}_{A(B)}e^{-i\omega t} \times \hat{\mathbf{k}})).\end{aligned} \tag{0.59}$$

In this non-spin-flopped case, all of the terms are oscillatory so we can just solve this equation by plugging in the vectors

$$\hat{\mathbf{m}}^0_{A(B)} = \begin{pmatrix} 0 \\ \pm 1 \\ 0 \end{pmatrix} \tag{0.60}$$

$$\delta\hat{\mathbf{m}}_{A(B)} = \begin{pmatrix} \delta m^x_{A(B)} \\ \delta m^y_{A(B)} \\ \delta m^z_{A(B)} \end{pmatrix} \tag{0.61}$$

$$\mathbf{H} = \begin{pmatrix} 0 \\ H \\ 0 \end{pmatrix} \tag{0.62}$$

$$\hat{\mathbf{k}} = \begin{pmatrix} 1 \\ 0 \\ 0 \end{pmatrix}, \tag{0.63}$$

which finally results in

$$\omega_1 = \mathrm{Re}\Bigg[-i\gamma\Bigg(-\Bigg(\sqrt{H^2(H_A + M_s)(H_A + 4H_E + M_s) + H_E^2(H_A - M_s)^2} + H^2 + H_A(H_E + M_s) + H_E M_s\Bigg)\Bigg)^{1/2}\Bigg] \tag{0.64}$$

$$\omega_2 = \mathrm{Re}\Bigg[-i\gamma\Bigg(\sqrt{H^2(H_A + M_s)(H_A + 4H_E + M_s) + H_E^2(H_A - M_s)^2} - H^2 - H_A(H_E + M_s) - H_E M_s\Bigg)^{1/2}\Bigg]. \tag{0.65}$$

0.3 Homodyne Detection

0.3.1 Basics

How do we measure a weak signal that results from a external drive in the presence of overwhelming noise? A smart thing to do is have the external drive turn on and off periodically to see if the signal buried in the noise changes. A smarter thing to do is to just vary the external drive with a smooth periodic function such as a $\sin \omega t$ and use the convenient properties Fourier transforms/expansions to extract the periodic signal buried in the noise. This is known as homodyne (means: same frequency) detection and it can drastically decrease the noise present in the system by rejecting noise that does not vary at the drive frequency as the signal does. A number of instruments can perform a homodyne measurement, but the workhorse instrument of the Ralph group is the lock-in amplifier.

Knowing the detailed working principles of a lock-in amplifier can help one avoid common measurement pitfalls, improve one's understanding of the physics being measured, and help with the theoretical modeling of measurement outcomes. At a very simplified level, a lock-in amplifier is just an adjustable mixer that feeds into a low-pass filter that feeds into a voltmeter as shown in Fig. 0.2. An input signal, $V_s(t) = V_s \sin \omega t$ comes into a homodyne mixer which will have the effect of

$$\text{Mixer}\left[V_s(t)\right] = V_s(t)V_r(t) = V_s \sin \omega t \times \sin \omega t/\sqrt{2} = \frac{V_s}{\sqrt{2}} \sin^2 \omega t = \frac{V_s}{2\sqrt{2}}(1 - \cos 2\omega t) \tag{0.66}$$

Next, this signal is fed into a low-pass filter, the effect of which can be expressed as an integration

$$\text{LP}\left[\frac{V_s}{2\sqrt{2}}(1 - \cos 2\omega t)\right] = \frac{\omega}{\pi} \int_0^{2\pi/\omega} dt \frac{V_s}{2\sqrt{2}}(1 - \cos 2\omega t) = \frac{V_s}{\sqrt{2}}. \tag{0.67}$$

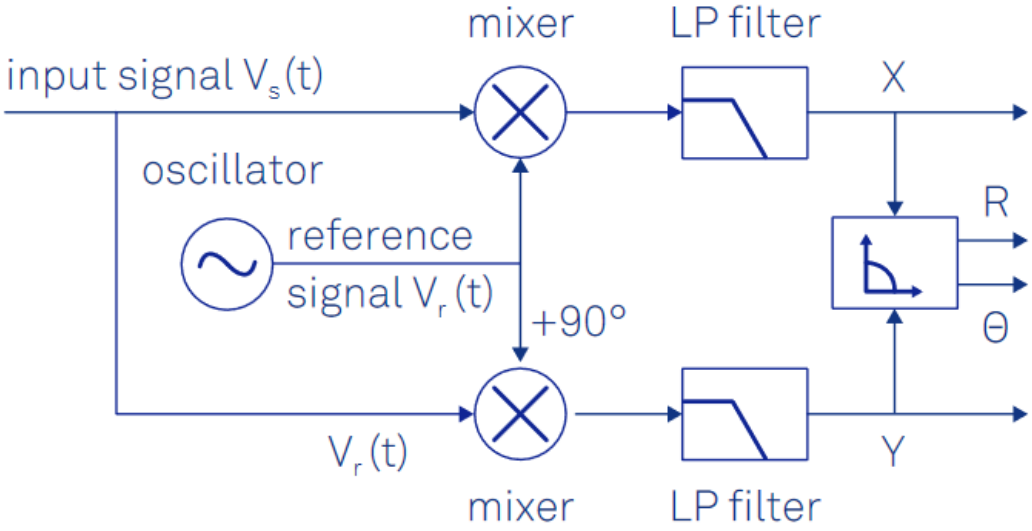

Figure 0.2: This figure was adapted from [5].

The voltmeter measures this signal, which is the root-mean-squared (RMS) input voltage.

0.3.2 Filter minutiae

How do we think of a lock-in amplifier more formally and get an intuition for the time constants and filters? A lock-in amplifier is, in terms of control theory, a first-order linear, time-invariant (LTI) system. LTI systems are characterized by a differential equation like so

$$\frac{dV(t)}{dt} + \frac{V(t)}{\tau} = \frac{f(t)}{\tau} \tag{0.68}$$

where τ is the time constant, V is the output response, and $f(t)$ is the external force/drive. Let us assume that $f(t) = Ae^{i\omega t}$, which matches many of our homodyne experimental setups. Define

$$\frac{du(t)}{dt} = e^{\int_0^t dt \frac{1}{\tau}} = e^{\frac{t}{\tau}}. \tag{0.69}$$

Multiplying both sides of Eq. (0.68) by $u(t)$, we get

$$\frac{dV(t)}{dt}e^{\frac{t}{\tau}} + \frac{V(t)}{\tau}e^{\frac{t}{\tau}} = \frac{f(t)}{\tau}e^{\frac{t}{\tau}}, \tag{0.70}$$

which is quite convenient because the left hand side can now be re-expressed like so:

$$\frac{d}{dt}\left(V(t)u(t)\right) = \frac{f(t)}{\tau}u(t). \tag{0.71}$$

Now, we can just perform a direct integration

$$\int_0^t dt' \frac{d}{dt'}\left(V(t')u(t')\right) = \int_0^t dt' \frac{f(t')}{\tau}u(t'). \tag{0.72}$$

The solution of this is just

$$V(t) = \frac{\int_0^t dt' \frac{f(t')}{\tau}u(t') + V(0)u(0)}{u(t)}. \tag{0.73}$$

Plugging in all of the functions

$$V(t) = e^{-t/\tau}\left(\frac{A}{\tau}\int_0^t dt' e^{i\omega t' + t'/\tau} + V(0)\right), \tag{0.74}$$

which has the simple solution

$$V(t) = V_0 e^{-t/\tau} + A\frac{1/\tau}{i\omega + 1/\tau}\left(e^{i\omega t} - e^{-t/\tau}\right), \tag{0.75}$$

where we have just enfored $V(t=0) = V_0$. Let's look at the real part of this solution for a few different values of τ in Fig. 0.3(a). As we can see, the curve in blue with the smallest time constant achieves the steady state oscillations the fastest. The longer the time constant the longer it takes these signals to achieve a steady state. In Fig. 0.3(b) we show the steady-state frequency response of the LTI solution where we have achieved steady-state by letting $t \to \infty$ in

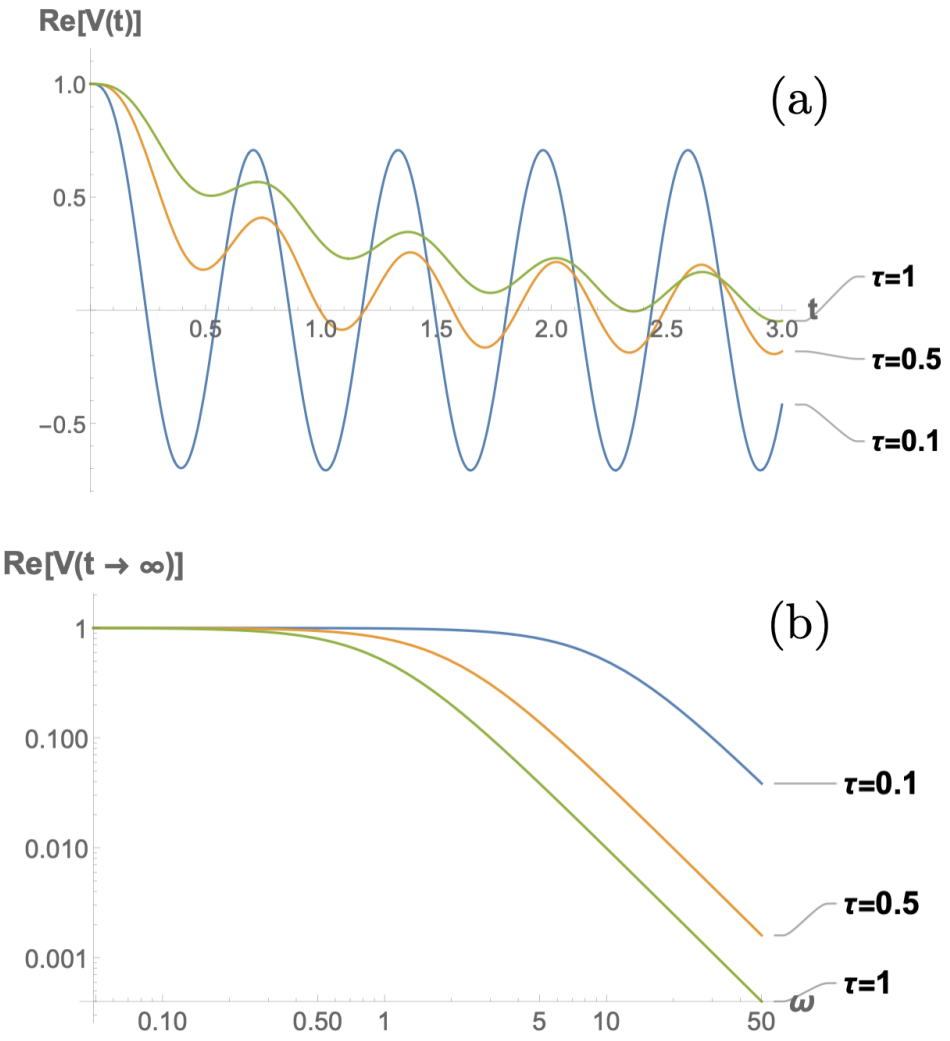

Figure 0.3: **(a)** The real part of the LTI solution (Eq. (0.75)) as a function of time for three different values of the time constant, τ. We have set $V_0 = A = 1$ and $\omega = 10$. **(b)** The frequency response of the steady-state solutions (Eq. (0.75) with $t \to \infty$).

Eq. (0.75). These curves are just equivalent to low-pass filters. As the time constant (τ) is increased, the bandwidth decreases, too. This is of course why the amplitude of the signals diminishes for larger time constants in Fig. 0.3(a) where we chose $\omega = 10$.

During lock-in measurements, the input signal is mixed with a homodyne reference signal to a produce an ideally dc (zero-frequency) signal, so the bandwidth set by the time constant will not cut off the desired signal from the measurement – the desired signal has a center frequency of 0. The reduced bandwidth set by the time constant will, however, filter resultant nonzero-

frequency signals due to noise and higher-harmonics. Therefore, setting the time constant to a larger values reduces the noise present in the system, but this comes at the cost of having to wait longer to achieve steady-state.

When using a lock-in amplifier, the user selects the width and also roll-off (sharpness) of the low-pass filter described above and shown in Fig. 0.3(b). This is a good feature because the width and roll-off together determine accuracy of the measurement, the SNR of the measurement, and also length of time that a measurement will take. Fig. 0.4 (available on [5]) is the perfect reference for determining the timing of a measurement when using a lock-in amplifier. Here

Order	Time	Roll-off		Bandwidth in units of 1/τ			Settling times in units of τ			
n	constant τ	dB/oct	dB/dec	f_{-3dB}	f_{NEP}	f_{NEP}/f_{-3dB}	63.2%	90%	99%	99.9%
1	1	6	20	0.159	0.250	1.57	1.00	2.30	4.61	6.91
2	1	12	40	0.102	0.125	1.23	2.15	3.89	6.64	9.23
3	1	18	60	0.081	0.094	1.16	3.26	5.32	8.41	11.23
4	1	24	80	0.069	0.078	1.13	4.35	6.68	10.05	13.06
5	1	30	100	0.061	0.069	1.12	5.43	7.99	11.60	14.79
6	1	36	120	0.056	0.062	1.11	6.51	9.27	13.11	16.45
7	1	42	140	0.051	0.057	1.11	7.58	10.53	14.57	18.06
8	1	48	160	0.048	0.053	1.10	8.64	11.77	16.00	19.62

Figure 0.4: This figure was adapted from [5].

is how this figure (table) ought to be consulted:

1. Determine how much time you have and want to spend on a measurement.

2. Figure out what you would like your settling time to be. This number is the wall-clock time that you will have to wait between changing an external parameter of the measurement and measuring *each* data point.

3. Determine the accuracy you want from those numbers on the right-hand-side of the table (63.2%, 90%, 99%, or 99.9%. You probably want at least 90%), and also the roll-off your lockin amplifier is capable of. (The DSPs go up to 24 dB/oct, while the Zurichs can go up to 48 dB/oct. In general, it pays to use a sharper filter roll-off and reduce your time constant to compensate. By this we mean: you will get the same SNR in a shorter

amount of wall-clock time by using a sharper filter. You can see this is the case by looking at the $f_{\mathrm{NEP}}/f_{\text{-3dB}}$ column.

4. Take your settling time from step 2 and consult the right-hand-side of the table to determine the settling time factor for your measurement from the accuracy and roll-off you determined in step 3.

5. Divide your settling time from step 2 by that number and set the time constant of your lockin to the quotient.

6. Set your measurement settling time to the number from step 2.

0.4 Microwave Calibration and Measurement Using a Vector Network Analyzer

A vector network analyzer (VNA) is a very useful tool for calibrating a microwave electronic circuit and also for performing high-frequency measurements of e.g. FMR.

0.4.1 Calibrating Microwave Current

ST-FMR measurements are performed with microwave currents and microwave currents are not always easy to deal with mathematically i.e. one cannot just discuss electric currents and voltages, one must treat all signals as waves. A more detailed microwave analysis is needed to be quantitative about the actual currents in the circuit and measured device. This is where the VNA comes in. The VNA is a highly-sensitive, multi-port microwave current generator and detector. The VNA has two ports that can each output a microwave current of known power and each read a microwave current, distinguishing both the magnitude and phase of the received signal, and even comparing the phase with the outputted signal. The two ports of the VNA are usually just called port 1 and port 2. The quantities that one usually measures with a VNA are complex scattering parameters $S_{11}, S_{12}, S_{21}, S_{22}$ that populate the scattering matrix for "power waves" in a two-port network where signals are just incident on a "black box."

$$\begin{pmatrix} b_1 \\ b_2 \end{pmatrix} = \begin{pmatrix} S_{11} & S_{12} \\ S_{21} & S_{22} \end{pmatrix} \begin{pmatrix} a_1 \\ a_2 \end{pmatrix}. \tag{0.76}$$

Here, $|a_1|^2$ is the incident power at port 1, $|b_1|^2$ is the reflected power at port 1, $|a_2|^2$ is the incident power at port 2, $|b_2|^2$ is the reflected power at port 2.

Figure 0.5: A two-port network with labels for the transmitted and reflected "power waves."

This is all well and good, but how do we actually use these numbers? Our goal is to determine a quantity usually denoted by Γ, which is the known as the reflection coefficient. This quantity is complex and, in a two-port network, is conveniently equal to S_{11}. Before we can do this, we need to *calibrate* the VNA. The calibration is essential because it discounts all of the other elements of the circuit except the device under test (DUT), so when we actually do the measurement, we only get information about the DUT. To use the jargon: the calibration procedure sets the "reference plane" of the VNA as close to the DUT as possible. To perform the calibration we essentially connect the network exactly as we would if we were doing the measurement, but we replace the DUT with certain calibration standards. For a reflection measurement (what we use when calibrating ST-FMR current), we only need to do a one-port calibration. Calibration is simple, just follow the instructions on the calibration menu on the VNA, which will have us calibrate the network by replacing the DUT with an open, a short, and a 50 Ω load. There is a calibration wafer with these three devices lithographically patterned on it so that we can connect to them with the microwave probe. Just touch the probe down to each device and press the corresponding button on the VNA calibration menu. For an FMR measurement that uses both ports, we need to perform the full two-port calibration, which requires a few more calibration standards. In this calibration, we use the microwave calibration kit with screw-on SMA open/short/loads.

Once the calibration is complete, we can measure S_{11}. The VNA will by

default measure all of the quantities while varying the frequency of applied microwave current. Make sure the range of frequencies at which you perform the measurements are contained within or equal to the VNA's range *during* calibration. After we measure complex S_{11} as a function of frequency, we have Γ because $\Gamma = S_{11}$. Now Γ is the complex reflection coefficient and we want the power transmitted to the device, so we want $1 - |\Gamma|^2$. The power transferred to the device for an input power P_0 is

$$P_{\text{dev}} = \left(1 - |\Gamma|^2\right) P_0. \tag{0.77}$$

The current is

$$I_{\text{dev}} = \sqrt{\frac{P_{\text{dev}}}{Z_0}\left(\frac{|\Gamma| - 1}{|\Gamma| + 1}\right)} = \sqrt{\frac{\left(1 - |\Gamma|^2\right) P_0}{Z_0}\left(\frac{|\Gamma| - 1}{|\Gamma| + 1}\right)}. \tag{0.78}$$

The quantity $(|\Gamma| - 1)/(|\Gamma| + 1)$ is the reciprocal of the "standing wave ratio" (SWR). The input power, P_0, is just what we read off of the microwave generator. Recall that to get the power in Watts we must convert the power that we read off the microwave generator like so

$$P(\text{W}) = \frac{10^{P(\text{dBm})/10}}{1000}. \tag{0.79}$$

An alternative, but equivalent, way to calculate the current is by just measuring the complex impedance of the device rather than S_{11}. We can do this by calibrating the VNA as we did before, but now reading off the complex impedance from the Smith chart view of the VNA. Once we have the complex impedance Z_L, we can calculate the current like so [6]

$$P_{\text{dev}} = \left(1 - \left|\frac{Z_L - Z_0}{Z_L + Z_0}\right|^2\right) P_0 \tag{0.80}$$

$$I_{\text{dev}} = \sqrt{\frac{P_{\text{dev}}}{Z_0}}. \tag{0.81}$$

If a device is mostly resistive and not very reactive i.e. $\mathrm{Re}[Z_L] \gg \mathrm{Im}[Z_L]$, then we can settle for measuring Z_L with a dc current using a multimeter, and plug in that value (again $Z_0 = 50\ \Omega$ and is real). This is not a bad assumption for most of the devices we fabricate, but a VNA should be used to test it if we are being careful.

0.5 Measuring FMR with a VNA

Because the VNA functions simultaneously as signal generator and detector, it may be conveniently used to measure FMR. This is particularly useful for exploring the parameter space of FMR, when the resonance conditions may not be known a priori as shown in Fig. 0.6. To do an FMR measurement, we can hook up the VNA to a waveguide (such as the one shown in Chapter 1, Fig. 1.1). It is important to first calibrate the VNA because we want all of the parts of the network, other than the DUT, to be considered as background and subtracted. A full 2-port calibration procedure must be followed because the FMR mesurement is a transmission measurement and not a reflection measurement as in ST-FMR. Once the calibration is completed, we perform an S_{21} measurement with the DUT on the CPW. What we get is shown in Fig. 0.6.

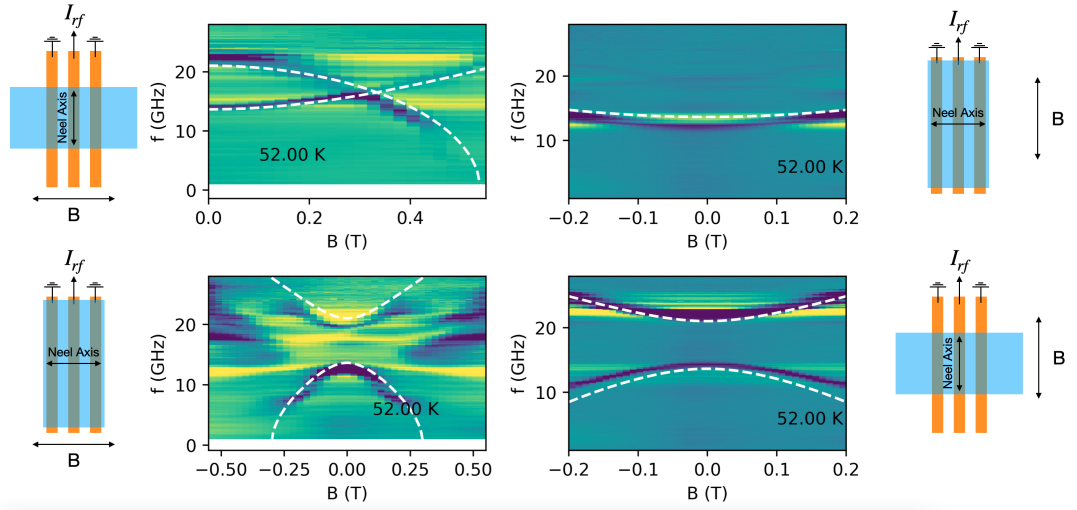

Figure 0.6: S_{21} as a function of the applied external magnetic field and applied microwave frequency from the VNA.

Here, we have measured a bulk crystal of CrSBr, which is a layered, 2D antiferromagnet [7]. The 4 figures reflect the 2 degrees-of-freedom we have when doing this measurement: because the CrSBr crystal has crystalline anisotropy (defined by the Neel axis), we can orient the Neel axis along or perpendicular to the CPW, and we can orient the external magnetic field along or perpendicular to the external applied magnetic field. The resonance conditions for these different situations are derived in the previous sections and the best-fits to these resonance conditions are the white, dashed lines overlayed on the figures. Fitting in this figure was simultaneously performed to all data across all 4 figures shown, with only 3 free parameters: $\mu_0 M_{\text{eff}} = 1.04(3)$ T, $\mu_0 H_E = 0.186(7)$ T, and $\mu_0 H_A = 0.167(4)$ T. All of the defintions for these parameters are described in the previous sections where we derive the equations. The fitting itself was an interesting and valuable exercise. To accomplish this, we first had to convert the dark absorption curves in Fig. 0.6 to data points because the actual magnitude of the S_{21} that is measured is not so meaningful, and we would like to dimension-reduce to get fit-able 2d data. To accomplish this, we scanned along vertical linecuts in each figure and put a data point at the minima along that line (always minima because this is an absorption measurement). After we had data points that we could fit to, we concatenated all of the data together into a piecewise data set, then fit to a piecewise function that was constructed by concatenating the appropriate fit functions together. The piecewise data and piecewise fit functions have a 1-to-1 correspondence. Once have these, we can do a global least squares optimization with the piecewise fit function over the piecewise data. That results in a combined fit over all data sets with consistent best-fit free parameters.

Chapter 1

ST-FMR, Artifacts and Hall ST-FMR

1.1 Introduction

The discovery of SOTs prompted the need for reliable measurement techniques to quantify them. It is also desireable to have measurement techniques that allow the quantification of SOTs without fully switching a FM's moment; this can make fabrication simpler, as one does not need to fabricate nanopillars or magnetic tunnel junctions (MTJs), allowing for more throughput in device measurement. A natural alternative to applying enough current to fully switch is to apply a small current that torques the magnetic moment perturbatively. Luckily, FMs often have anisotropic magnetoresistance (AMR), so the resistance of a simple HM/FM device will depend on the orientation of the magnetic moment and the perturbation can be read out as a change in the device resistance.

ST-FMR was one of the first techniques developed to measure the strength of SOTs [8]. This technique measures SOTs perturbatively and reads out the perturbation as a change in the device resistance, as described above. The measurement is performed by applying a microwave current on the order of a few GHz over a HM/FM bilayer device because this is the frequency regime of ferromagnetic resonance. Ordinarily, the microwave current is modulated by

amplitude modulation (AM, we will see how this can lead to some issues in the next chapter), and the AM is referenced by a lock-in amplifier that measures the *voltage* across the device. The voltage is measured because the resistance oscillations due to the AMR are homodyne with the applied microwave current, which means the two mix to produce a dc voltage. In the most popular version of this measurement, an external magnetic field is applied and swept to meet the Kittel resonance condition (Eq. 0.11), resulting in a resonant lineshape from which one can extract the magnitude of the SOTs that caused the perturbations by fitting.

One key assumption in the modeling used to fit is that the resonance lineshape is wholly due to the SOTs acting on the magnetization, and not additional processes that could produce spurious resonant voltages. However, it has been known that additional phenomenon, most saliently spin pumping [9], can produce resonant lineshapes that have the same structure as those produced by SOTs [10]. Dealing with the spin pumping addition to the ST-FMR signal from the SOTs has been difficult in the past because there is no endogenous parameter of the technique to vary that allows for a distinguishing of spin pumping from the SOT signal. Many previous works have used the derived equations of the spin pumping signal to either argue it is negligible or simply subtract the theoretically-determined value from the measurement. The problem with both of these methods is that spin pumping can be difficult to quantify from theory because some parameters that go into the model are difficult to measure accurately (e.g. $g_{\text{eff}}^{\uparrow\downarrow}$, the effective spin mixing conductance at the interface).

A more reliable and consistent method is therefore needed to determine the true contribution of spin pumping (and other artifacts) to the measured ST-FMR signals. In this chapter, we present such a method, which we call "Hall ST-FMR" because it is a Hall measurement of ST-FMR signal. This method is simple in that it does not complicate the conventional technique much – Hall leads are added to the second-level lithography mask and the

Hall voltage is measured simultaneously to the conventional longitudinal. The Hall voltage that is read out is a result of different magnetoresistances from that of the conventional longitudinal. Most importantly, the anomalous Hall effect (AHE, couples to the out of plane magnetization component) will also contribute to the Hall measurement and can be separated from the signal due to the planar Hall effect (PHE, the Hall analogue of the AMR, both couple to the in-plane magnetization component). This separation allows us to leverage the differences in the measured signals due to the AHE vs. the PHE/AMR to fully cancel artifacts such as spin pumping, experimentally. What's more, is that the method of cancellation is robust enough to cancel *any* resonant signal that depends *only* on the amplitude of the magnetic perturbations and not the phase. We describe this technique below.

In the following, much is taken and adapted from Ref. [11].

1.2 Preface

I will begin by reviewing the basic working principles of ferromagnetic resonance (FMR) measurements and then spin-torque ferromagnetic resonance (ST-FMR) measurements [8], the latter of which is most popular method for measuring SOTs on a heterostructure with in-plane magnetization.

1.2.1 FMR

The magnetization of a film can be reoriented using magnetic fields, and the equations of motion for a film magnetization can be written as the LLG equation (Eq. 0.1, reproduced here):

$$\frac{d\hat{\mathbf{m}}}{dt} = -\gamma\hat{\mathbf{m}} \times \left[\mathbf{H} + \mu_0 M_{\text{eff}}(\hat{\mathbf{m}} \cdot \hat{\mathbf{Z}})\hat{\mathbf{Z}}\right] + \alpha\frac{d\hat{\mathbf{m}}}{dt} + \boldsymbol{\tau} \tag{1.1}$$

Like many equations of motion, this is nothing more than a (excusing the oxymoron) more complicated damped simple harmonic oscillator. If an external

drive is added to the system, there will be a condition under which the oscillator (magnetic moment) will be in resonance. From the derivation in the preface, we got Eq. (0.11), which is the exactly the resonance condition of an in-plane-magnetized film: $\omega_0 = \gamma\sqrt{H(H + M_{\text{eff}})}$. The drive frequency here is set by the scale of γ. We like the units where $\gamma \approx 28$ GHz/T, and we will treat it as such throughout this document. Clearly from the resonance condition, ω_0 can really be anything because of the proportionality with the external field applied, H; however, to measure a whole resonance lineshape that will be fittable, H will have to be non-zero. This means that, to get a whole resonance lineshape, ω_0 ought to be on the order of GHz.

Something remains that deserves more explanation: what is doing the external drive here? In conventional FMR, the drive is provided by electromagnetic fields that are produced outside of the magnetic film under investigation. For a chunk of magnetic material, this can be done inside a resonant cavity where the magnetic material lies in between signal and receiver antennas. Some of the energy from the electromagnetic fields produced by the signal antenna will be absorbed by the magnetic material as the reorientation or precession of the sample magnetization. This amount of energy absorption is proportional to the precession amplitude of the magnetization, so if the magnet has a larger precession, such as when its resonance condition is met, less energy will make it to the receiver antenna, which will be detectable. For thin films, a cavity is not necessary, and the geometry of the film allows for FMR detection via a coplanar waveguide as shown in Fig. 1.1. This is the Ralph group "flip-chip" FMR apparatus. In the figure, there is an upside-down wafer with a thin magnetic film on it in contact with a copper ground-signal-ground coplanar waveguide. Microwave SMA cables carry a microwave current through the signal stripline of the coplanar waveguide, which produces microwave electromagnetic fields. These microwave electromagnetic fields reorient the film magnetization, absorbing some of the electromagnetic energy, just as in the case of the cavity FMR.

Once magnetization precesses, a mutual inductance with the film and stripline changes the current that makes it through the stripline. The current that makes it through the coplanar waveguide is again related to the precession amplitude of the magnetization in the thin film and may be detected.

It is difficult to get any quantitative information out of the amplitudes of these FMR signals. This is not so difficult to see because, just by looking at Fig. 1.1, one can see that this wafer piece with a strange shape feels many non-trivial stray fields from the coplanar waveguide. Something like finite element simulation with the exact shape of the wafer piece could be a solution to this issue. Usually, FMR like this is used to determine specific parameters that are not as sensitive to these "edge effects." For example, FMR makes for an excellent measurement of the effective magnetization, M_{eff}, or the Gilbert damping, α. These two parameters can be measured via the frequency dependences of the resonant field (Eq. 0.11) and the resonance linewidth $\Delta = f\alpha/\gamma$.

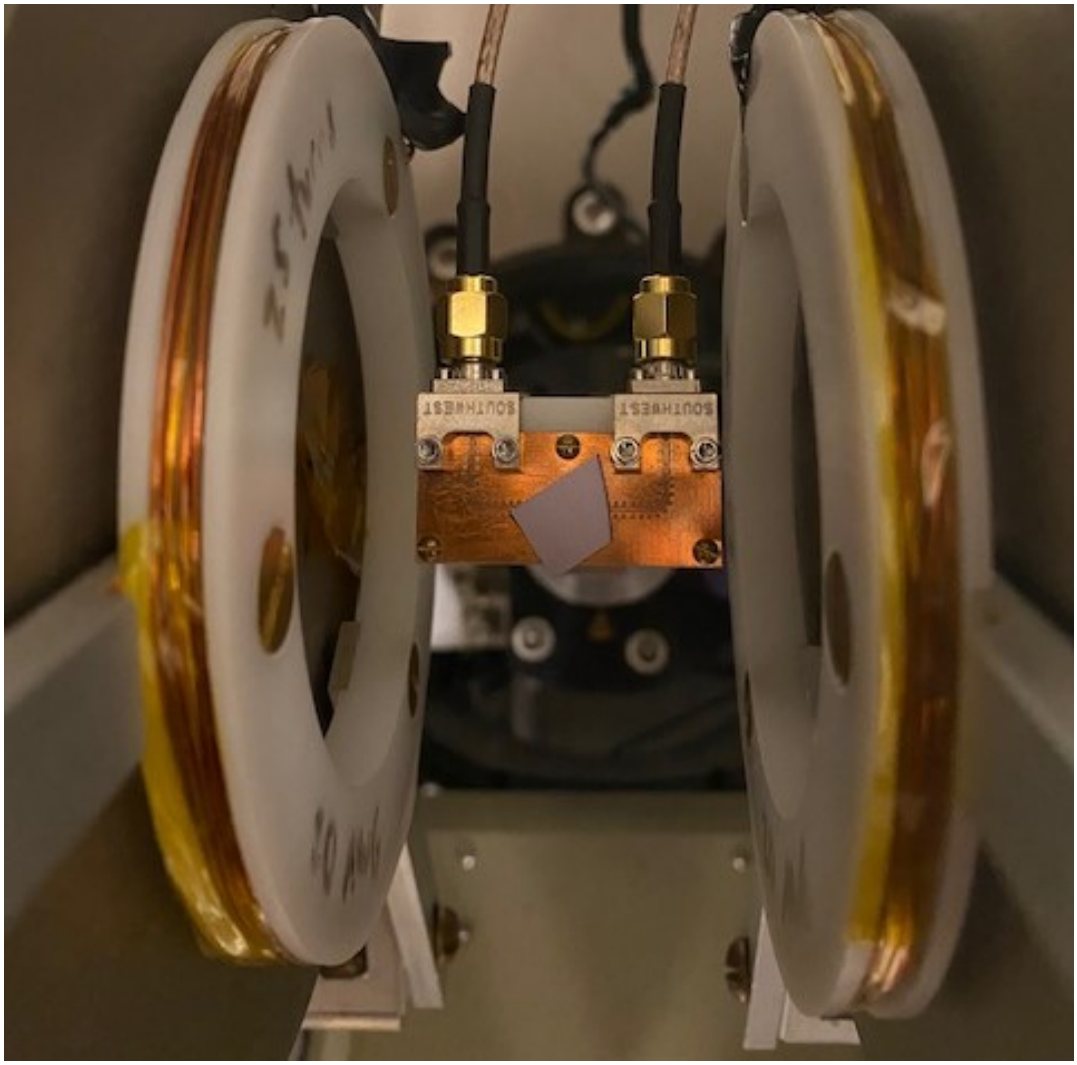

Figure 1.1: The Ralph Group "flip-chip" FMR apparatus. In the center there is an upside-down wafer chip with a thin-film magnetic layer on the bottom. This thin film is in close proximity with the copper coplanar waveguide that carries microwave current from the SMA cables above it. Two wound-coil electromagnets on either side of the coplanar waveguide carry a small, AC magnetic field that is used for homodyne detection. On the left and right edges of the figure, the core poles of the larger electromagnet are shown. These apply the DC magnetic field, H, that is used to meet the resonance condition.

1.2.2 An On-Chip CPW

One can extract useful information from the amplitudes of an FMR measurement by fabricating a CPW on-chip i.e. lithographically patterning a channel made of a bilayer of a ferromagnetic film interfaced with a generic, non-magnetic, conducting metal with with small spin-orbit coupling such as Cu. By having a channel of known size, one can easily determine the magnetic fields acting on the magnetic layer produced by the current flowing in the non-magnetic conducting layer via Ampere's law applied to an infinite sheet of current:

$$\mathbf{H}_{\emptyset} = \frac{\mu_0 J_c t_{\mathrm{NM}}}{2} \hat{Y} \tag{1.2}$$

where J_c is the charge current density flowing through the non-magnetic material, t_{NM} is the thickness of the non-magnetic layer, and the charge current flows in the $\hat{X}$-direction. This works because the thickness of these thin films is orders of magnitude smaller than the lateral dimensions even when nanofabricated. We usually call this current-induced magnetic field the Ørsted field. Of course, there will still be stray fields near the edges of the device i.e. there will be components of $\mathbf{H}_{\emptyset}$ that are along the $\hat{Z}$ axis. One can usually see effects such as this when the measurement of magnetization can be resolved spatially e.g. in a MOKE measurement [12]. These edge effects normally cancel out or account for a very small part of the total measured signal in electrical measurements that effectively integrate over the path connecting the leads that measure the device voltage.

1.3 ST-FMR

ST-FMR relies on the same device principle introduced in the previous subsection (on-chip CPW) where now, instead of using a metal such as Cu to carry the current, a heavy metal with strong spin-orbit coupling is used (e.g. Pt). Now there will be additional fields/torques affecting the magnetic moment due to the spin Hall effect in the heavy metal and spin accumulation at the interface of the ferromagnet and heavy metal. In conventional ST-FMR, a microwave current is injected along a rectangular sample of a heavy metal (HM)/ferromagnet (FM) bilayer to induce FMR through current-induced torques acting on the magnetization. Within a simple macrospin model, the Landau-Lifshitz-Gilbert-Slonczewski (LLGS) equation captures the resulting dynamics of the magnetic moment:

$$\begin{aligned}\dot{\hat{m}} = \gamma \hat{m} \times \frac{dF}{d\hat{m}} \; + \; \alpha \hat{m} \times \dot{\hat{m}} \\ + \tau_{\mathrm{DL}}^{0} \hat{m} \times (\hat{\sigma} \times \hat{m}) \; + \; \tau_{\mathrm{FL}}^{0} \hat{\sigma} \times \hat{m}\end{aligned} \tag{1.3}$$

where $\hat{m}$ is the normalized magnetic moment of the FM, F is the free energy density of the FM, $\gamma = 2\mu_B/\hbar$ is the gyromagnetic ratio with μ_B the Bohr magneton, and α is the Gilbert damping parameter. The final two terms represent the current-induced damping-like and field-like torques, with prefactors

$$\tau_{\mathrm{DL}}^{0} = \xi_{\mathrm{DL}} \frac{\mu_B J_e}{e M_S t_{\mathrm{FM}}} \tag{1.4}$$

$$\tau_{\mathrm{FL}}^{0} = \xi_{\mathrm{FL}} \frac{\mu_B J_e}{e M_S t_{\mathrm{FM}}} + \frac{\mu_B \mu_0 J_e t_{\mathrm{HM}}}{\hbar}. \tag{1.5}$$

Here ξ_{DL} and ξ_{FL} are dimensionless spin-torque efficiencies that one might wish to measure for a given material system. J_e is the charge current density in the HM, e is the magnitude of the electron charge, M_S is the saturation magnetization of the FM, $t_{\mathrm{FM(HM)}}$ is the thickness of the ferromagnetic (heavy metal) layer, and $\hat{\sigma}$ denotes the polarization of the spin current incident on the ferro-

magnet. The second term in Eq. (1.5) comes from the current-induced Ørsted field. For a non-magnetic heavy metal with an ordinary high-symmetry crystal structure, $\hat{\sigma}$ is required by symmetry to be in-plane and perpendicular to the applied current so that, for an in-plane magnetization, the damping-like torque points in the sample plane and the field-like torque points out of plane; we will assume this to be the case throughout this document.

The magnetic resonance can be detected via a rectified longitudinal DC voltage (oriented along the length of the wire parallel to the current) caused by the mixing of the microwave current with resistance oscillations produced by the precessing magnet via the anisotropic magnetoresistance (AMR) or spin Hall magnetoresistance (SMR) [13, 14]. The resonance peak shape as a function of magnetic field magnitude at a constant field angle for this rectified signal is the sum of symmetric and antisymmetric Lorentzian functions. For a magnetic layer with in-plane anisotropy and and in-plane magnetic field, the symmetric component arises from τ_{DL}^{0} and the antisymmetric component from τ_{FL}^{0}: the combination of the current-induced Ørsted field and field-like SOT. Once the microwave current is calibrated, the measurement allows determinations of both ξ_{DL} and ξ_{FL}, assuming there are no other artifacts contaminating the signal.

When the FM layer is resonantly excited, a pure spin current resulting from spin pumping (SP) or the longitudinal spin Seebeck effect (LSSE) can also flow from the FM layer into the HM layer and produce a measurable voltage through the ISHE of the HM [9, 15, 10, 16, 17, 18, 19, 20, 21]. Furthermore, an out-of-plane temperature gradient within the heterostructure due to resonant heating can produce a thermoelectric voltage from ordinary or anomalous Nernst effects [22, 23]. In all of these processes, the result is a DC voltage perpendicular to the magnetization axis with a symmetric Lorentzian lineshape [24, 25, 10]. Consequently, if these artifact signals are sufficiently large, they can contaminate ST-FMR measurements of τ_{DL}^{0}. The signals from spin-torque rectification and the spin-pumping/resonant-heating artifacts all have the same dependence

on the angle of an in-plane magnetic field: $\propto \sin(2\phi)\cos(\phi)$, with ϕ measured relative to the positive applied current direction [10, 26, 27, 28], making artifact effects difficult to disentangle.

In what follows, we demonstrate that if one performs a ST-FMR experiment as a function of the angle of an in-plane magnetic field by measuring the resonant DC voltage *transverse* to the current (i.e., in a Hall geometry) the rectified spin-torque contribution and the spin pumping/resonant heating can be distinguished.Previous works have performed ST-FMR in the transverse geometry [29, 27], but these studies did not illustrate how to separate the rectified spin-torque contribution from the artifact signals. A closely-related idea was used previously in experiments which studied SP/ISHE signals from magnetic precession excited using oscillating magnetic fields, in order to separate out unwanted (in that context) rectification signals [18, 30]. Harder et al. have published a review mapping out the field-angle dependence expected for resonance experiments in both longitudinal and transverse geometries for different orientations of excitation [31].

1.4 ST-FMR Theory

1.4.1 Conventional (Longitudinal)

We consider a thin-film macrospin magnet with in-plane anisotropy subject to an external in-plane magnetic field oriented at an angle ϕ with respect to the positive current direction, that aligns the equilibrium direction of the magnetization (see Fig. 1.2). We define the $\hat{y}$ axis to be parallel to the equilibrium direction of the magnetization and $\hat{z}$ to be perpendicular to the sample plane so that $\hat{x} = \hat{y} \times \hat{z}$ is in-plane. We will also use capital letters to indicate a separate coordinate system fixed with respect to the sample, where $\hat{X}$ is along the current direction, $\hat{Z} = \hat{z}$, and $\hat{Y} = \hat{Z} \times \hat{X}$. Spherical polar coordinates θ, ϕ for the magnetization orientation are defined relative to the X, Y, Z axes.

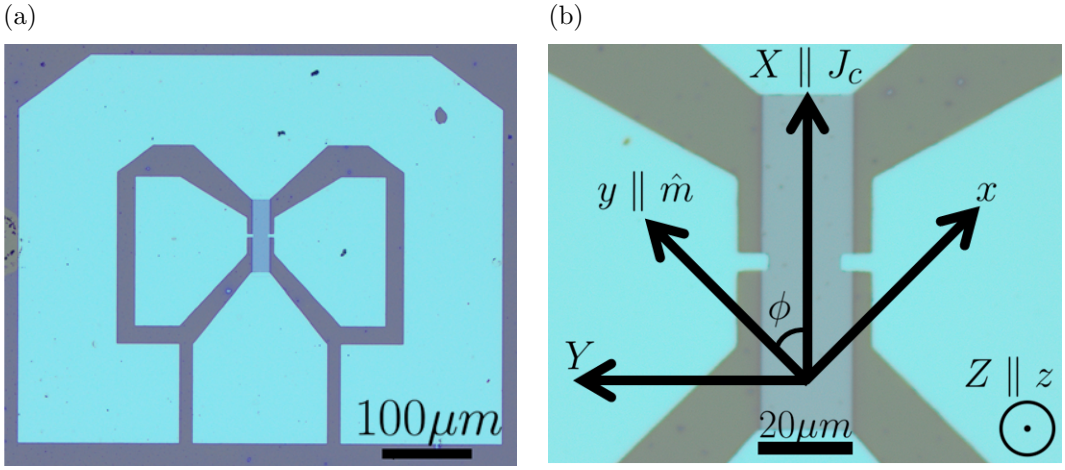

Figure 1.2: **(a)** Optical image of our Hall ST-FMR device, showing the geometry of the contact pads. This particular device featured a Pt(6)/CoFeB(6) bilayer measuring 20×80 μm^2 (in the center, dark blue). The scale bar is 100 μm. **(b)** Zoomed-in optical image of the bilayer and contacts with our coordinate definitions. The XYZ (capital) coordinates are fixed relative to the device geometry while xyz (lowercase) coordinates are relative to the equilibrium orientation of the magnetization. The scale bar is 20 μm.

A microwave current $I_{\mathrm{RF}}\mathrm{Re}\left[e^{-i\omega t}\right]$ is applied, producing alternating torques with amplitudes $\tau_x = \tau_{\mathrm{DL}}^0\cos(\phi)$ and $\tau_z = \tau_z^0\cos(\phi) = (\tau_{\mathrm{FL}}^0 + \tau_{\mathrm{Oe}}^0)\cos(\phi)$ in the $\hat{x}$ and $\hat{z}$ directions. With these definitions, τ_{Oe}^0 takes a positive value by Ampere's Law and τ_{DL}^0 is positive for the spin Hall effect of Pt. Linearization and solution of the LLGS equation (see Chapter 0) allows us to calculate the oscillatory components of the magnetic moment, in complex notation,

$$\begin{aligned} m_x &= \frac{-\omega_2\tau_z + i\omega\tau_x}{-\gamma(B-B_0)\omega^+ + i\alpha\omega\omega^+} \\ m_z &= \frac{\omega_1\tau_x + i\omega\tau_z}{-\gamma(B-B_0)\omega^+ + i\alpha\omega\omega^+}. \end{aligned} \tag{1.6}$$

Here B_0 is the resonance field, B is the applied external field, $\omega_1 = \gamma B_0$, $\omega_2 = \gamma(B_0 + \mu_0 M_{\mathrm{eff}})$, and $\omega^+ = \omega_1 + \omega_2$; M_{eff} is the in-plane saturation magnetization (M_S) minus any out-of-plane anisotropy. Note that by our definition of coordinate axes, during the precession $m_x = -d\phi$ and $m_z = -d\theta$.

Assuming that the anisotropic magnetoresistance has the form $R_{XX} = R_0 + R_{\mathrm{AMR}}m_X^2$, the spin-torque mixing voltage in conventional ST-FMR can be

written

$$V_{XX}^{\text{mix}} = \frac{I_{\text{RF}}}{2} R_{\text{AMR}} \text{Re}\left[m_x\right] \sin 2\phi, \tag{1.7}$$

or

$$\begin{aligned} V_{XX}^{\text{mix}} = \frac{I_{\text{RF}} R_{\text{AMR}}}{2\alpha\omega^{+}} \sin(2\phi)\cos(\phi) \\ \times \left(S(B)\tau_{\text{DL}}^{0} + A(B)\frac{\omega_2}{\omega}\tau_z^0 \right) \end{aligned} \tag{1.8}$$

where we have defined the symmetric and antisymmetric Lorentzians

$$S(B) = \frac{\Delta^2}{(B - B_0)^2 + \Delta^2} \tag{1.9}$$

$$A(B) = \frac{(B - B_0)\Delta}{(B - B_0)^2 + \Delta^2} \tag{1.10}$$

and the half-width at half-maximum linewidth $\Delta = \alpha\omega/\gamma$. Here R_{AMR} includes contributions from both the anisotropic magnetoresistance in the magnet and the spin Hall magnetoresistance in the Pt layer, as these produce identical contributions to the ST-FMR signals for our sample geometry. Indeed, the total magnetoresistance for a longitudinal measurement can be written in spherical coordinates as

$$R_{XX} = R_0 + R_{\text{AMR}} \sin^2\theta \cos^2\phi - R_{\text{SMR}} \sin^2\theta \sin^2\phi. \tag{1.11}$$

where R_0 is a constant offset, R_{AMR} is the scale of the anisotropic magnetoresistance, and R_{SMR} is the scale of the spin Hall magnetoresistance [32]. We consider small angle precession such that $\theta = \theta_0 + \Delta\theta$ and $\phi = \phi_0 + \Delta\phi$ with $\Delta\theta, \Delta\phi \ll 1$ and expand to get

$$\begin{aligned} R_{XX} = R_0 + R_{\text{AMR}} \left(\sin^2\theta_0 \cos^2\phi_0 + \Delta\theta \sin 2\theta_0 \cos^2\phi_0 - \Delta\phi \sin^2\theta_0 \sin 2\phi_0 \right) \\ - R_{\text{SMR}} \left(\sin^2\theta_0 \sin^2\phi_0 + \Delta\theta \sin 2\theta_0 \sin^2\phi_0 + \Delta\phi \sin^2\theta_0 \sin 2\phi_0 \right). \end{aligned} \tag{1.12}$$

The only pieces of Eq. (1.12) that are current-rectifiable (able to produce a mixing voltage with the rf current) are the terms linear in $\Delta\theta$ and $\Delta\phi$. For an in-plane magnet we have $\theta_0 = \pi/2$, and therefore the mixing voltage becomes

$$V_{XX}^{\text{mix}} = \frac{I_{\text{RF}}}{2}(R_{\text{AMR}} + R_{\text{SMR}})\,(-\Delta\phi \sin 2\phi_0) = \frac{I_{\text{RF}}}{2}(R_{\text{AMR}} + R_{\text{SMR}})\,(\text{Re}[m_x] \sin 2\phi_0)\,. \tag{1.13}$$

Only the in-plane deflections of the magnet are rectified to produce a mixing voltage, and the AMR and SMR contributions simply add. For simplicity of notation in the main text, we therefore incorporate both the AMR and SMR contributions in one magnetoresistance amplitude R_{AMR}.

1.4.2 Hall

We can compute the transverse spin-torque mixing voltage within the same framework. We assume that the Hall resistance has the symmetry $R_{XY} = R_{\text{PHE}} m_X m_Y + R_{\text{AHE}} m_Z$, where R_{PHE} is the scale of the planar Hall effect and R_{AHE} is the scale of the anomalous Hall effect, in which case [33]

$$V_{XY}^{\text{mix}} = \frac{I_{\text{RF}}}{2}\left(-R_{\text{PHE}} \cos 2\phi\, \text{Re}\left[m_x\right] + R_{\text{AHE}} \text{Re}\left[m_z\right]\right). \tag{1.14}$$

Using the results from Eq. (1.6),

$$\begin{aligned} V_{XY}^{\text{mix}} = &-\frac{I_{\text{RF}} R_{\text{PHE}}}{2\alpha\omega^{+}} \cos\left(2\phi\right) \cos(\phi) \\ &\times \left(S(B)\tau_{\text{DL}}^{0} + A(B)\frac{\omega_2}{\omega}\tau_{z}^{0}\right) \\ &+ \frac{I_{\text{RF}} R_{\text{AHE}}}{2\alpha\omega^{+}} \cos(\phi) \\ &\times \left(S(B)\tau_{z}^{0} - A(B)\frac{\omega_1}{\omega}\tau_{\text{DL}}^{0}\right). \end{aligned} \tag{1.15}$$

1.4.3 Artifacts

The artifact signals due to spin pumping and resonant heating can also contribute to both the longitudinal and transverse ST-FMR voltages [26, 6, 27]. All

of the artifacts we consider, spin pumping/inverse spin Hall effect (SP/ISHE), longitudinal spin Seebeck effect/inverse spin Hall effect (LSSE/ISHE), and Nernst effect (NE), produce resonant DC electric fields that are in-plane and perpendicular to the magnetization axis, and proportional to the square of the precession amplitude (with the precession amplitude $\propto \cos\phi$). Because these signals depend only on the precession amplitude and not phase, they have symmetric lineshapes. Taking the components in the longitudinal and transverse directions, the artifact voltages are therefore

$$V_{\mathrm{art}} = E^0_{\mathrm{art}} S(B) \cos^2\phi \begin{cases} L\sin\phi & \text{longitudinal} \\ W\cos\phi & \text{transverse} \end{cases} \tag{1.16}$$

where $E^0_{\mathrm{art}} = E^0_{\mathrm{SP}} + E^0_{\mathrm{LSSE}} + E^0_{\mathrm{NE}}$ is the total electric field generated by all artifact signals. The artifact voltages for the longitudinal and transverse measurements differ only by geometric factors and angular symmetry: L is the device length (parallel to the current flow) and W is the transverse device width.

Spin Pumping

The electric field due to the spin pumping/inverse spin Hall effect can be calculated following the methods of refs. [9, 10]. SP describes a process where the precessing magnetization at FMR causes the ferromagnetic layer to inject a spin current into the heavy metal layer; this can create a voltage through the ISHE. The time-averaged spin current in the heavy-metal layer can be written as [9, 15, 10]

$$\overleftrightarrow{j}^{\mathrm{SP}}_{\hat{\sigma}}(z) = \hat{\sigma} \otimes \vec{j}^{\mathrm{SP}}(z) = \frac{\hbar}{4\pi} g^{\uparrow\downarrow}_{\mathrm{eff}} \frac{\sinh\left[(t_{\mathrm{HM}} + z)/\lambda_{\mathrm{sd}}\right]}{\sinh\left[t_{\mathrm{HM}}/\lambda_{\mathrm{sd}}\right]} \left\langle \hat{m} \times \dot{\hat{m}} \right\rangle \otimes (-\hat{z}) \tag{1.17}$$

where $\vec{j}^{\mathrm{SP}} \propto -\hat{z}$ is the direction of the spin current flow, $\hat{\sigma} \propto \left|\left\langle \hat{m} \times \dot{\hat{m}} \right\rangle\right| \parallel -\hat{m}$ is the polarization of the pumped spin current (where the negative sign is to

account for *enhanced* Gilbert Damping due to Spin pumping [34, 35]), $g_{\text{eff}}^{\uparrow\downarrow}$ is the effective spin mixing conductance at the interface, and λ_{sd} is the spin diffusion length of the HM. The resultant voltage is

$$V_{\text{ISHE}} = -R_{\text{tot}} I = -R_{\text{tot}} \int_{\Sigma_{\text{HM}}} \vec{j}_e^{\text{HM}} \cdot d\vec{A} \tag{1.18}$$

where R_{tot} is the total device resistance (that will differ for the longitudinal and transverse cases), Σ_{HM} is the cross-section of the heavy-metal layer, $\vec{j}_e^{\text{HM}} = (2e/\hbar)\theta_{\text{SH}}\vec{j}^{\text{SP}} \times \hat{\sigma}$ is the charge current arising from the ISHE [10] and $d\vec{A}$ is a differential surface area normal, which points along the vector connecting the leads that we are measuring across. The negative sign in Eq. (1.18) is due to the fact that we are measuring the electric field that arises from the open circuit condition of the device [10]. Simplifying the integrals we have (for the longitudinal geometry)

$$\begin{aligned} V_{\text{ISHE}} &= -R_{\text{tot}} \int_{\Sigma_{\text{HM}}} \vec{j}_e^{\text{HM}} \cdot d\vec{A} \\ &= -R_{\text{tot}} \int_{-W/2}^{W/2} \int_{0}^{-t_{\text{HM}}} \vec{j}_e^{\text{HM}} \cdot d\vec{A} \\ &= -R_{\text{tot}} W \sin\phi \int_{0}^{-t_{\text{HM}}} \left| \vec{j}_e^{\text{HM}} \right| dz \end{aligned} \tag{1.19}$$

where W is the width of the Hall bar (dimension along $\hat{Y}$). Note that in the transverse measurement $W \sin\phi \to L\cos\phi$ where L is the device bar length. The only part of $\vec{j}_e^{\text{HM}}$ that depends on the thickness is

$$\int_0^{-t_{\text{HM}}} \frac{\sinh((t_{\text{HM}} + z)/\lambda_{\text{sd}})}{\sinh(t_{\text{HM}}/\lambda_{\text{sd}})}\, dz = \lambda_{\text{sd}} \tanh\left(\frac{t_{\text{HM}}}{2\lambda_{\text{sd}}}\right). \tag{1.20}$$

At this point, we have (for the longitudinal geometry)

$$V_{\text{ISHE}} = -\frac{2e}{\hbar}\theta_{\text{SH}} R_{\text{tot}} W \sin\phi \frac{\hbar}{4\pi} g_{\text{eff}}^{\uparrow\downarrow} \lambda_{\text{sd}} \left| \left\langle \hat{m} \times \dot{\hat{m}} \right\rangle \right| \tanh\left(\frac{t_{\text{HM}}}{2\lambda_{\text{sd}}}\right). \tag{1.21}$$

We now only need to calculate $\left\langle \hat{m} \times \dot{\hat{m}} \right\rangle$, but we already have the oscillatory

magnetization components from before (Eq. (1.6)). We can write $\left\langle \hat{m} \times \dot{\hat{m}} \right\rangle = \omega \mathrm{Im}\left[m_x m_z^*\right](-\hat{m})$, so therefore

$$\omega \mathrm{Im}\left[m_x m_z^*\right] = \frac{\omega^2}{(\gamma\omega^+)^2(B-B_0)^2 + (\omega\alpha\omega^+)^2}\left[\omega_1\tau_x^2 + \omega_2\tau_z^2\right] \tag{1.22}$$

$$= \frac{\omega_1\tau_x^2 + \omega_2\tau_z^2}{(\alpha\omega^+)^2} S(B), \tag{1.23}$$

where $S(B) = \Delta^2/\left[(B-B_0)^2 + \Delta^2\right]$ is a symmetric Lorentzian and $\Delta \equiv \omega\alpha/\gamma$. The voltage in the device resulting from the pumped spin can then be written as (for the longitudinal geometry)

$$V_{\mathrm{ISHE}} = -\frac{2e}{\hbar}\theta_{\mathrm{SH}} R_{\mathrm{tot}} W \sin\phi \frac{\hbar}{4\pi} g_{\mathrm{eff}}^{\uparrow\downarrow} \lambda_{\mathrm{sd}} \left[\frac{\omega_1\tau_x^2 + \omega_2\tau_z^2}{(\alpha\omega^+)^2} S(B)\right] \tanh\left(\frac{t_{\mathrm{HM}}}{2\lambda_{\mathrm{sd}}}\right). \tag{1.24}$$

Putting all of this together, using that $\omega_1 = \gamma B_0$, $\omega_2 = \gamma(B_0 + \mu_0 M_{\mathrm{eff}})$, and $\omega^+ = \omega_1 + \omega_2 = \gamma(2B_0 + \mu_0 M_{\mathrm{eff}})$, noting that τ_x and τ_z have the angular dependence specified in Eq. (8), and that for the transverse case one has $W \sin\phi \to L\cos\phi$, the spin-pumping voltages in the longitudinal and transverse directions become

$$V_{\mathrm{ISHE}} = -\frac{eB_0 R_{\mathrm{tot}}\theta_{\mathrm{SH}}}{2\pi\alpha^2\gamma(2B_0 + \mu_0 M_{\mathrm{eff}})^2} g_{\mathrm{eff}}^{\uparrow\downarrow}\lambda_{\mathrm{sd}} \tanh\left(\frac{t_{\mathrm{HM}}}{2\lambda_{\mathrm{sd}}}\right)\left[(\tau_{\mathrm{DL}}^0)^2 + \left(1 + \frac{\mu_0 M_{\mathrm{eff}}}{B_0}\right)(\tau_{\mathrm{z}}^0)^2\right]$$
$$\times S(B)\cos^2\phi \begin{cases} W\sin\phi, & \text{longitudinal} \\ L\cos\phi, & \text{transverse} \end{cases} \tag{1.25}$$

$$= -\frac{eB_0\theta_{\mathrm{SH}}}{2\pi\alpha^2\gamma(2B_0 + \mu_0 M_{\mathrm{eff}})^2} \frac{1}{\sum_i t_i\sigma_i} g_{\mathrm{eff}}^{\uparrow\downarrow}\lambda_{\mathrm{sd}} \tanh\left(\frac{t_{\mathrm{HM}}}{2\lambda_{\mathrm{sd}}}\right)\left[(\tau_{\mathrm{DL}}^0)^2 + \left(1 + \frac{\mu_0 M_{\mathrm{eff}}}{B_0}\right)(\tau_{\mathrm{z}}^0)^2\right]$$
$$\times S(B)\cos^2\phi \begin{cases} L\sin\phi, & \text{longitudinal} \\ W\cos\phi, & \text{transverse} \end{cases}. \tag{1.26}$$

In the final equation we have expressed the values of R_{tot} for the longitudinal and transverse cases in terms of the conductivities of the $i = \mathrm{HM}$ and FM layers

added as parallel conductors. The final, simplified expression we use for the electric field due to SP/ISHE is

$$E_{\mathrm{SP}}^{0} = \frac{e\theta_{\mathrm{SH}} g_{\mathrm{eff}}^{\uparrow\downarrow}}{2\pi \sum_i \sigma_i t_i} \lambda_{\mathrm{sd}} \tanh\left(\frac{t_{\mathrm{HM}}}{2\lambda_{\mathrm{sd}}}\right) \times \left[\frac{(\tau_{\mathrm{DL}}^{0})^2 \omega_1 + (\tau_z^0)^2 \omega_2}{\alpha^2 \left(\omega^+\right)^2}\right]. \tag{1.27}$$

Recall θ_{SH} is the spin Hall ratio in the HM (related to the damping-like spin torque efficiency by $\theta_{\mathrm{SH}} = \xi_{\mathrm{DL}}/T_{\mathrm{int}}$, where T_{int} is an interfacial spin transmission factor), $g_{\mathrm{eff}}^{\uparrow\downarrow}$ is the real part of the effective spin mixing conductance, σ_i (t_i) the charge conductivity (thickness) of layer i, and λ_{sd} the spin diffusion length of the HM.

Resonant Heating

If one assumes that the artifacts due to resonant heating by the current-induced torques are proportional to the energy absorbed by the magnetic layer during resonant excitation, the peak DC electric field due to LSSE/ISHE and NE can be calculated similarly [22, 36]. Here, we begin with the magnetic free energy per unit area assuming no in-plane anisotropy

$$F/A = -\vec{B} \cdot M + \frac{1}{2}\mu_0 t_{\mathrm{FM}} M_s M_{\mathrm{eff}} m_z^2. \tag{1.28}$$

We assume the external field saturates the magnetization in the y-direction

$$F/A = -B m_y M_s t_{\mathrm{FM}} + \frac{1}{2}\mu_0 t_{\mathrm{FM}} M_s M_{\mathrm{eff}} m_z^2 \tag{1.29}$$

and using $|m| = 1$,

$$F/A = -B M_s t_{\mathrm{FM}} + \frac{M_s t_{\mathrm{FM}}}{2}\left[B m_x^2 + (B + \mu_0 M_{\mathrm{eff}}) m_z^2\right]. \tag{1.30}$$

Taking a time derivative, we have

$$\partial_t F/A = M_s t_{\mathrm{FM}} \left[B m_x \frac{dm_x}{dt} + (B + \mu_0 M_{\mathrm{eff}}) m_z \frac{dm_z}{dt} \right]. \tag{1.31}$$

To calculate the energy absorbed from the current-induced torques, we set $dm_x/dt = \tau_x$ and $dm_z/dt = \tau_z$. Averaging over one precession cycle, the power per unit area absorbed by the magnet is

$$\langle \partial_t F/A \rangle = \frac{M_s t_{\mathrm{FM}}}{2} \{ B \tau_x \mathrm{Re}[m_x] + (B + \mu_0 M_{\mathrm{eff}}) \tau_z \mathrm{Re}[m_z] \} \tag{1.32}$$

$$= \frac{M_s t_{\mathrm{FM}} \alpha \omega^+}{2\gamma} \left[\frac{\omega_1 \tau_x^2 + \omega_2 \tau_z^2}{(\alpha \omega^+)^2} \right] S(B). \tag{1.33}$$

The in-plane torque τ_x contains contributions from both the antidamping spin-orbit torque and the out-of-plane component of the Oersted field, but when averaged over the width of the sample the antidamping spin-orbit torque gives the larger contribution.

Using equation (1.33), with some parameters determined on a Pt(6 nm)/CoFeB(t_{FM}) thickness series, we calculate the power absorbed per unit area within the magnetic layer of the Pt/CoFeB samples as a function of the magnetic layer thickness. This is plotted as a fraction of the Ohmic dissipation in the magnetic layer in Fig. 1.3. The relative amount of heating for the thinnest samples is greater primarily because of increased magnetic damping for the thinnest samples.

The final, simplified form of the resonant heating effects we use is

$$E^0_{\mathrm{LSSE}} + E^0_{\mathrm{NE}} = C \frac{M_s t_{\mathrm{FM}} \alpha \omega^+}{2\gamma \sum_i \sigma_i t_i} \left[\frac{(\tau^0_{\mathrm{DL}})^2 \omega_1 + (\tau^0_z)^2 \omega_2}{\alpha^2 \left(\omega^+\right)^2} \right]. \tag{1.34}$$

Here C is a material-dependent prefactor. Due to the factor of $t_{\mathrm{FM}} \alpha \omega^+$ in the numerator, the resonant heating contributions scale differently than the SP/ISHE as a function of FM thickness, damping, and measurement frequency.

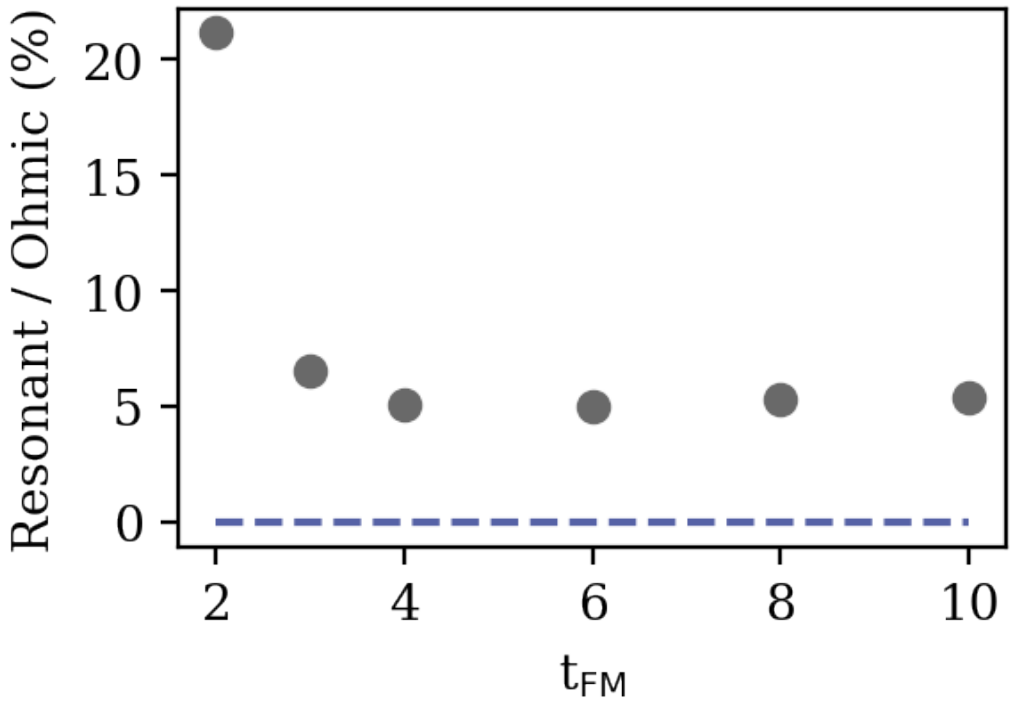

Figure 1.3: The ratio of resonant power absorbed to the Ohmic dissipation in the ferromagnetic layer as a function of the ferromagnetic layer thickness, for the Pt(6 nm)/CoFeB(t_{FM}) series of samples.

1.4.4 Putting it all together

Adding the rectification and artifact contributions [and using that $\cos^2\phi\sin\phi = (\sin 2\phi\cos\phi)/2$ and $\cos^3\phi = (\cos\phi + \cos 2\phi\cos\phi)/2$], the amplitudes of the symmetric and antisymmetric components of the total longitudinal and transverse ST-FMR signals have the angular dependence

$$\begin{aligned} S_{XX}(\phi) &= S_{XX}^{\mathrm{AMR/art}}\sin 2\phi\cos\phi \\ A_{XX}(\phi) &= A_{XX}^{\mathrm{AMR}}\sin 2\phi\cos\phi \\ S_{XY}(\phi) &= S_{XY}^{\mathrm{PHE/art}}\cos 2\phi\cos\phi + S_{XY}^{\mathrm{AHE/art}}\cos\phi \\ A_{XY}(\phi) &= A_{XY}^{\mathrm{PHE}}\cos 2\phi\cos\phi + A_{XY}^{\mathrm{AHE}}\cos\phi \end{aligned} \tag{1.35}$$

with the amplitude coefficients

$$\begin{aligned}
S_{XX}^{\mathrm{AMR/art}} &= \frac{I_{\mathrm{RF}}}{2\alpha\omega^{+}} R_{\mathrm{AMR}} \tau_{\mathrm{DL}}^{0} - \frac{L}{2} E_{\mathrm{art}}^{0} \\
&\equiv S_{XX}^{\mathrm{AMR}} + V_{\mathrm{art}} \\
A_{XX}^{\mathrm{AMR}} &= \frac{I_{\mathrm{RF}}}{2\alpha\omega^{+}} R_{\mathrm{AMR}} \frac{\omega_2}{\omega} \tau_{z}^{0} \\
S_{XY}^{\mathrm{PHE/art}} &= -\frac{I_{\mathrm{RF}}}{2\alpha\omega^{+}} R_{\mathrm{PHE}} \tau_{\mathrm{DL}}^{0} - \frac{W}{2} E_{\mathrm{art}}^{0} \\
A_{XY}^{\mathrm{PHE}} &= -\frac{I_{\mathrm{RF}}}{2\alpha\omega^{+}} R_{\mathrm{PHE}} \frac{\omega_2}{\omega} \tau_{z}^{0} \\
S_{XY}^{\mathrm{AHE/art}} &= \frac{I_{\mathrm{RF}}}{2\alpha\omega^{+}} R_{\mathrm{AHE}} \tau_{z}^{0} - \frac{W}{2} E_{\mathrm{art}}^{0} \\
A_{XY}^{\mathrm{AHE}} &= -\frac{I_{\mathrm{RF}}}{2\alpha\omega^{+}} R_{\mathrm{AHE}} \frac{\omega_1}{\omega} \tau_{\mathrm{DL}}^{0}.
\end{aligned} \tag{1.36}$$

One can see that all of the S_{XX} and S_{XY} rectification signals are contaminated by artifact voltages. If one measures just S_{XX} and A_{XX} for in-plane magnetic fields (as in conventional ST-FMR) there is no way to distinguish τ_{DL}^{0} from the artifact contributions. However, τ_{DL}^{0} appears by itself, without any artifact contamination, in the coefficient A_{XY}^{AHE}. One way to achieve a measurement of τ_{DL}^{0}, free of these artifacts, is therefore to directly use the expression for A_{XY}^{AHE} in Eq. (1.36) along with careful calibration of I_{RF}, α, and R_{AHE}. The out-of-plane torque τ_{z}^{0} can similarly be determined from A_{XX}^{AMR} or A_{XY}^{PHE}. Alternatively, the expressions in Eq. (1.36) also allow E_{art}^{0} and the torque efficiencies ξ_{DL} and ξ_{FL} to be measured without calibrating I_{RF}, α, and the the magnetoresistance scales by taking appropriate ratios to cancel prefactors. We can do so using measurements of either the set of parameters $\{S_{XX}^{\mathrm{AMR/art}}, A_{XX}^{\mathrm{AMR}}, S_{XY}^{\mathrm{AHE/art}}, A_{XY}^{\mathrm{AHE}}\}$ or $\{S_{XY}^{\mathrm{PHE/art}}, A_{XY}^{\mathrm{PHE}}, S_{XY}^{\mathrm{AHE/art}}, A_{XY}^{\mathrm{AHE}}\}$. We do not expect that the equations involving R_{AMR} and R_{PHE} are physically independent because anisotropic magnetoresistance and the planar Hall effect originate from the same microscopic mechanism. Therefore if the assumptions of our model are correct these two strategies for taking ratios to cancel prefactors must agree modulo experimental noise. We will perform both calculations, and test their agreement as a consistency check.

First, using that on resonance $\omega = \sqrt{\omega_1\omega_2}$ we calculate the ratio $\eta \equiv (\tau^0_{\rm DL}/\tau^0_z)\sqrt{\omega_1/\omega_2}$ employing the pair of parameters S and A associated with each of the AMR, PHE, and AHE:

$$\eta = \frac{-A^{\rm AHE}_{XY}}{S^{\rm AHE/art}_{XY} + W(E_{\rm art}/2)} =$$

$$\begin{cases} \dfrac{S^{\rm PHE/art}_{XY} + W(E_{\rm art}/2)}{A^{\rm PHE}_{XY}} & \text{(1.37a)} \\ \dfrac{S^{\rm AMR/art}_{XX} + L(E_{\rm art}/2)}{A^{\rm AMR}_{XX}} & \text{(1.37b)} \end{cases}$$

Using the measured amplitude coefficients, one can solve separately for $E_{\rm art}$ using either equation (1.37a) or (1.37b), and check consistency.

It still remains to determine $\tau^0_{\rm DL}$ and to separate the two contributions to $\tau^0_z = \tau^0_{\rm FL} + \tau^0_{\rm Oe}$. We choose to do this using a method from ref. [37], in a way that determines both the of the spin-torque efficiencies $\xi_{\rm DL}$ and $\xi_{\rm FL}$ at the same time without requiring a separate calibration of $I_{\rm RF}$. We perform measurements for a series of samples with different thicknesses of the ferromagnetic layer and determine $\eta = (\tau^0_{\rm DL}/\tau^0_z)\sqrt{\omega_1/\omega_2}$ for each sample from any of the expressions in Eqs. (1.37a,1.37b), after solving for $E_{\rm art}$. We then define

$$\xi_{\rm FMR} \equiv \eta \frac{e\mu_0 M_s t_{\rm HM} t_{\rm FM}}{\hbar} \sqrt{1 + \frac{\mu_0 M_{\rm eff}}{B_0}} \tag{1.38}$$

so that using Equations (1.4) & (1.5), and that by Ampere's Law $\tau^0_{\rm Oe} = \gamma\mu_0 J_e t_{\rm HM}/2$ one has

$$\frac{1}{\xi_{\rm FMR}} = \frac{1}{\xi_{\rm DL}} \left(1 + \frac{\hbar}{e} \frac{\xi_{\rm FL}}{\mu_0 M_s t_{\rm FM} t_{\rm HM}}\right). \tag{1.39}$$

Performing a linear fit of $1/\xi_{\rm FMR}$ vs. $1/t_{\rm FM}$ then can be used to determine $1/\xi_{\rm DL}$ (from the intercept) and $\xi_{\rm FL}$ (from the slope).

1.5 Results

We used DC-magnetron sputtering to grow multiayers with the structure substrate/Ta(1)/Pt(6)/ferromagnet(t_{FM})/Al(1) (where numbers in parentheses are thicknesses in nm), using three different ferromagnets (FMs): $Co_{40}Fe_{40}B_{20}$ (CoFeB), permalloy ($Ni_{81}Fe_{19}$ = Py) and $Co_{90}Fe_{10}$ (CoFe). Each of the three FMs is expected to have different AMR, PHE, and AHE values, and therefore different strengths of rectified spin-torque signals relative to the artifacts. In particular, CoFeB has weak planar magnetoresistances (AMR and PHE), and has been argued previously to exhibit a significant contribution from SP/ISHE in ST-FMR [26, 6]. The CoFeB devices were grown with $t_{\mathrm{FM}} = \{2, 3, 4, 6, 8, 10\}$ in separate depositions. The Py and $Co_{90}Fe_{10}$ devices were grown with single relatively-large thicknesses to give measurable artifact signals: t_{Py}= 8 nm and t_{CoFe}= 6 nm. All devices were grown on high-resistivity ($> 2 \times 10^4\,\Omega$-cm), thermally-oxidized silicon wafers to prevent RF current leakage or capacitive coupling. The Ta was used as a seed layer and has negligible contribution to the SOTs we measure due to the low conductivity of Ta relative to Pt (ρ_{Pt} = 20.4 $\mu\Omega$cm, ρ_{CoFeB} = 110 $\mu\Omega$cm). The Al cap layer protects the layers below it, and is oxidized upon exposure to atmosphere.

The as-deposited samples were patterned using photolithography and Ar ion-milling to define rectangular bars ranging in size from 20 × 40 μm to 40 × 80 μm with various aspect ratios. The transverse leads and contact pads were then made using a second photolithography step, deposited by sputtering Ti(3 nm)/Pt(75 nm) and formed by lift-off so that the side channels extended a few microns on top of the main bar (see Fig. 1.2). We were careful that the magnetic layer did not extend beyond the defined rectangle into the transverse leads. In early devices, we etched full Hall-bar shapes within the first layer of lithography so that the transverse leads included some of the same magnetic layer as the main channel. For those early devices, we found that the resulting analyses of spin-orbit torques produced anomalous results, varying with the

dimensions of the leads and the contact separation. This could possibly be due to spatial non-uniformities in the magnetic orientation and precession, as was speculated in ref. [29]. Ultimately, the magnetic bilayer was left to be simply rectangular to promote uniform precession modes, and this removed the anomalous geometry dependence.

For the ST-FMR measurements, we connected the devices to an amplitude-modulated ("AM" with $f_{\mathrm{AM}} \approx 1700$ Hz) microwave source through the AC port of a bias tee and to a lock-in amplifier through the DC port, which detected the longitudinal signal. Another lock-in amplifier measured the DC voltage across the Hall leads of the device. Both lock-in amplifiers referenced the same AM signal, and we collected ST-FMR data in both the longitudinal and transverse directions simultaneously. An in-plane applied magnetic field was applied at varying angles ϕ using a projected-field magnet. We used fixed microwave frequencies in the range 7-12 GHz, applied 20 dBm of microwave power, and all measurements were performed at room temperature. In Figs. 1.4(a) and 1.4(d) we show examples of the detected resonant signals from the parallel (XX) and transverse (XY) lock-ins for the Pt(6)/CoFeB(6) sample.

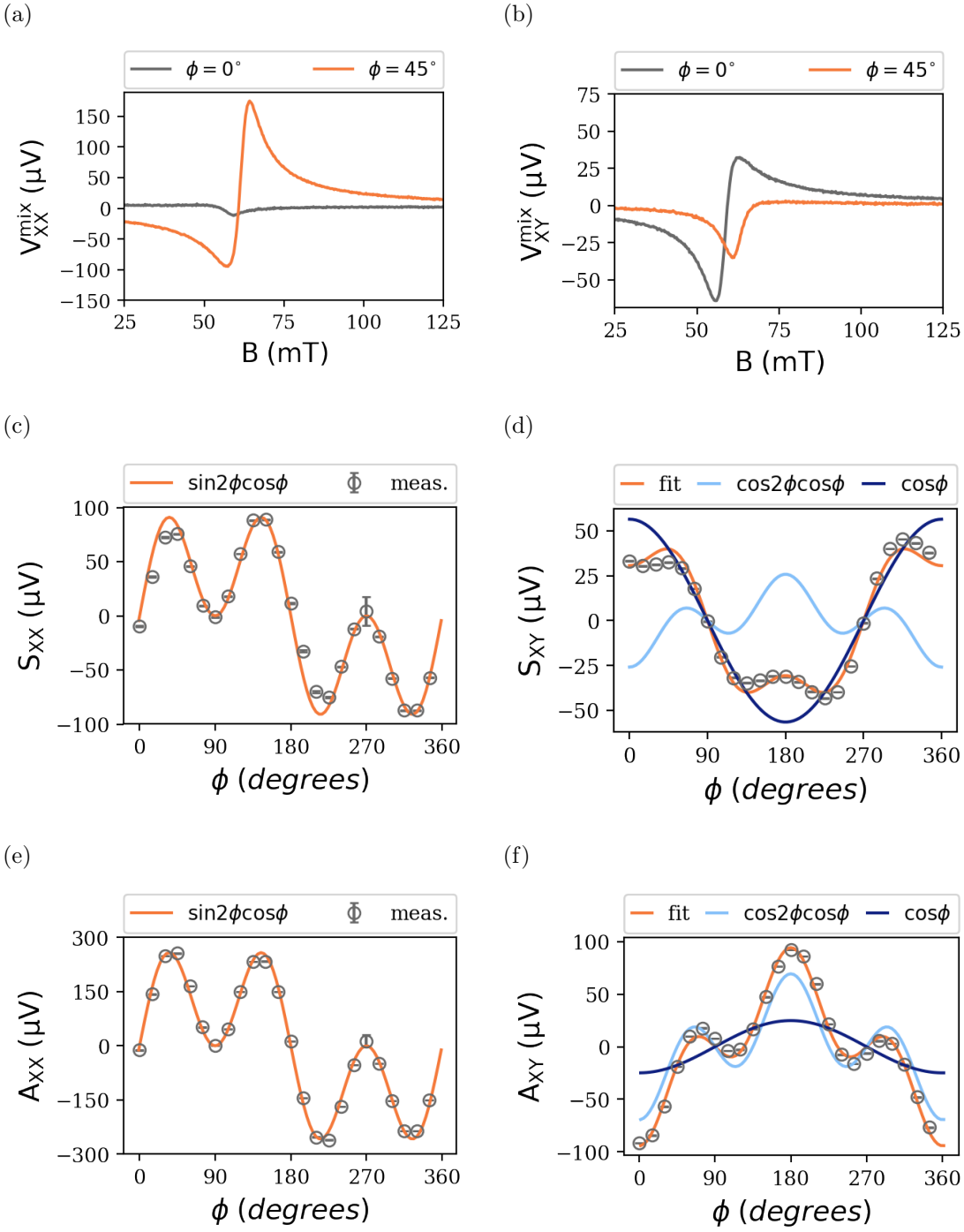

Figure 1.4: ST-FMR measurements of a Pt(6 nm)/CoFeB(6 nm) sample for a measurement frequency $f = 8$ GHz. **(a)** Longitudinal resonant signals for field sweeps with two different field angles. **(b) & (c)** Symmetric (S_{XX}) and antisymmetric (A_{XX}) Lorentzian fit components for the longitudinal resonant signal as a function of the external field angle. **(d)** Transverse resonant signals for field sweeps with two different field angles. **(e) & (f)** Symmetric (S_{XY}) and antisymmetric (A_{XY}) Lorentzian fit components for the transverse resonant signal as a function of the external field angle. The orange fit line in (b) & (c) is a fit to $\sin 2\phi \cos\phi$ (AMR); the light and dark blue fit lines in (e,f) are fits to $\cos 2\phi \cos\phi$ (PHE) and $\cos\phi$ (AHE), respectively, and their sum (orange) fits the data.

Both the longitudinal and transverse resonances are well-fit to a sum of symmetric and antisymmetric Lorentzian peaks, with varying relative weights. For each sample we performed field-swept measurements at a variety of angles ϕ, extracting the symmetric and antisymmetric components of the resonances for both the longitudinal and transverse signals. The results for a Pt(6)/CoFeB(6) sample are shown in Fig. 1.4(b,c,e,f), along with fits to Eq. (1.35). Analogous results for Pt(6)/Py(8) and Pt(6)/CoFe(6) samples are below

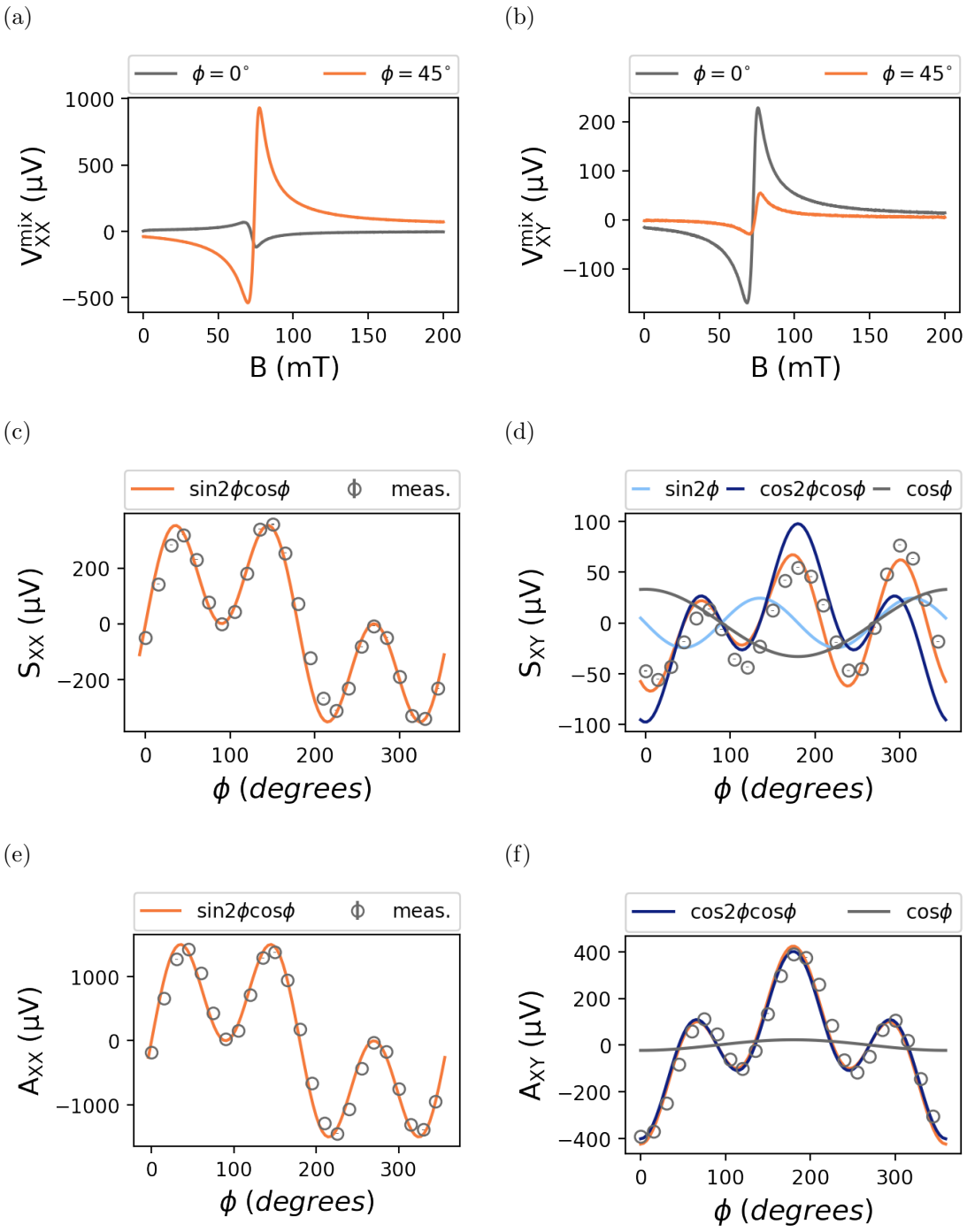

Figure 1.5: Hall ST-FMR results collected on Pt(6)/Py(8).

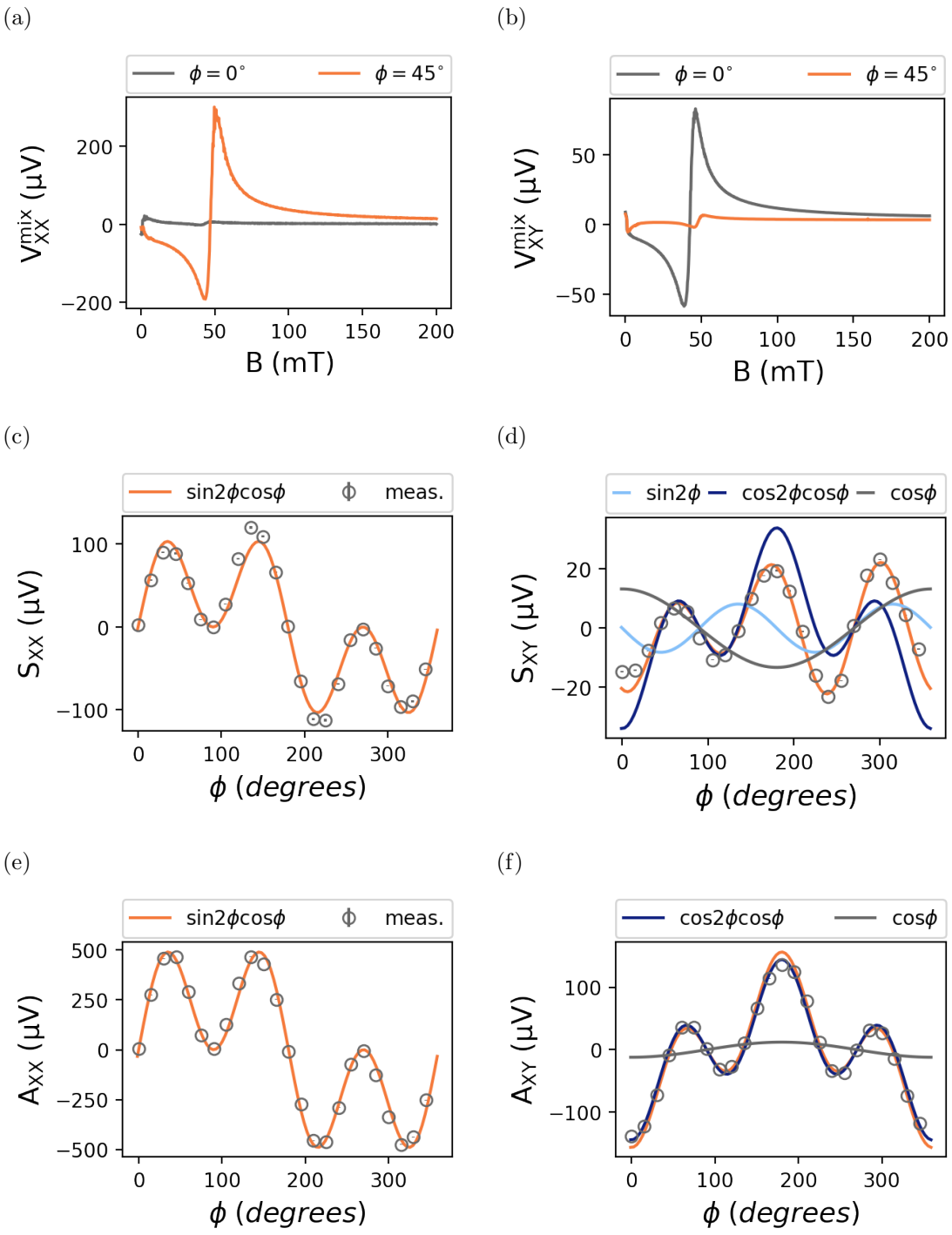

Figure 1.6: Hall ST-FMR results collected on Pt(6)/CoFe(6).

We find excellent agreement with the expected angular dependences for S_{XX}, A_{XX}, and A_{XY}. For S_{XY} the dominant contributions to the angular dependence are, as expected the $\cos 2\phi \cos \phi$ and $\cos \phi$ terms, but in addition, we detect a small component approximately proportional to $\sin 2\phi$. This additional contri-

bution is less than 10% of the larger terms in S_{XY} for all thicknesses of CoFeB, small enough that it is not included in the fit shown in Fig. 1.4(e). It is more significant in the CoFe and Py samples that we measured, though still smaller than the $\cos 2\phi \cos\phi$ and $\cos\phi$ amplitudes in S_{XY}. A $\sin 2\phi$ contribution can only arise from a breaking of mirror symmetry relative to the sample's $\hat{Y}$-$\hat{Z}$ plane. This symmetry is broken in our samples by the different contact geometries on the two ends of the sample wire (see Fig. 1(a)). The form of the $\sin 2\phi$ signal can be explained as due resonant heating that produces an in-plane thermal gradient in the longitudinal direction of the sample (due *e.g.* to differences in heat sinking at the two ends) that is transduced to a tranverse voltage with the symmetry of the planar Hall effect ($\propto m_X m_Y$). We have checked that the signal is not due to a sample tilt or to a non-resonant DC current that might arise from rectification of the applied microwave signal at the sample contacts. All of the other Fourier components that are the main subject of our analysis maintain the $\hat{Y}$-$\hat{Z}$-plane mirror symmetry, and so they cannot be altered at first order by a process that breaks this symmetry. Being a separate Fourier component, the $\sin 2\phi$ contribution also does not affect the fits to Eq. (1.35) to determine the six amplitude coefficients $S_{XX}^{\mathrm{AMR/art}}$, A_{XX}^{AMR}, $S_{XY}^{\mathrm{PHE/art}}$, A_{XY}^{PHE}, $S_{XY}^{\mathrm{AHE/art}}$, and A_{XY}^{AHE}. Using these coefficients, we calculate E_{art} by solving Eqs. (1.37a) or (1.37a). There is a potential ambiguity in which roots of Eqs. (1.37a) and (1.37a) to select when applying the quadratic formula. In our measurements, one root would give unphysical results, e.g. a sign change of ξ_{DL}. An important check of our method (and a check that the $\sin 2\phi$ term in S_{XY} does not contaminate the analysis) is that these two independent methods for determining E_{art}^{0} (Eqs. (1.37a) and (1.37b)) give consistent results. We show below that this is indeed the case.

(a)

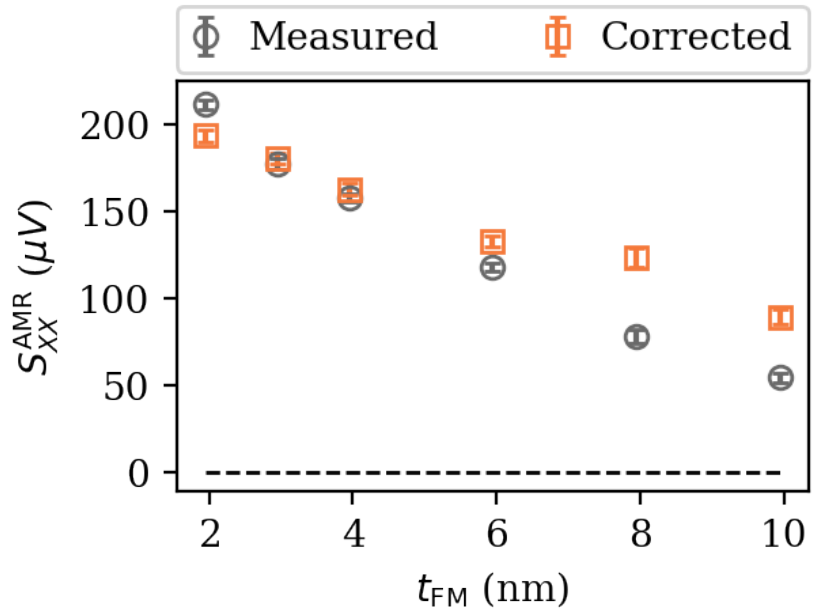

(b)

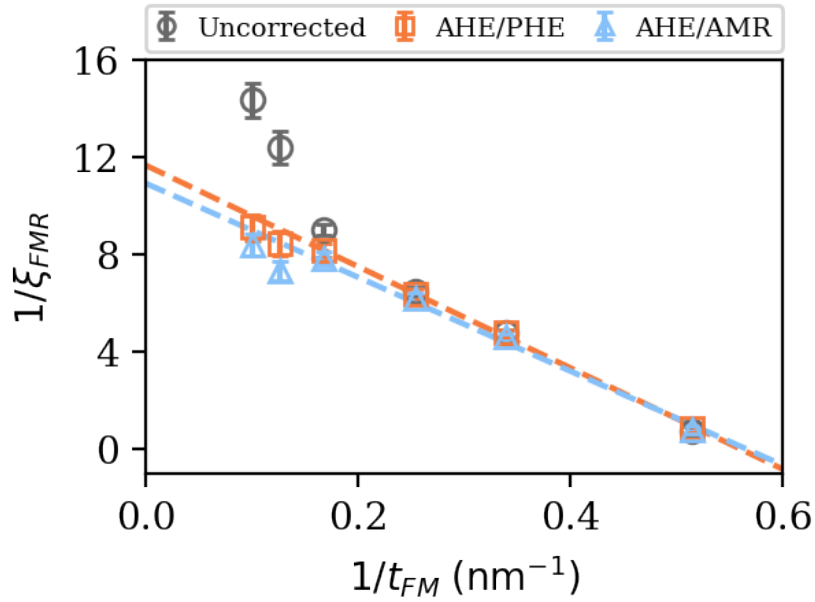

Figure 1.7: **(a)** The uncorrected measured value of S_{XX}^{AMR} vs. t_{FM}, together with the value corrected by removing the artifact voltage. **(b)** The inverse ξ_{FMR} vs. inverse t_{FM}. The y-intercept of the line is $1/\xi_{\mathrm{DL}}$ and the slope is proportional to ξ_{FL} as in Eq. (1.39). The two fit lines are color-matched fits to the data points from the AHE/PHE and AHE/AMR corrections.

Figure 1.7(a) shows the total amplitude of the longitudinal symmetric ST-FMR component (labeled as "Measured"), and the corrected value S_{XX}^{AMR} from which V_{art} has been subtracted. For CoFeB layer thicknesses 6 nm and below, the magnitude of V_{art} is much less than the magnitude of S_{XX}^{AMR}, so that the artifacts have little effect on ST-FMR measurements of the spin-orbit torques. However, with increasing CoFeB thickness the magnitude of S_{XX}^{AMR} decreases and V_{art} grows, so we find experimentally that for the CoFeB layers thicker than 6 nm the artifact voltage becomes a significant fraction of the total signal. In this regime, V_{art} and S_{XX}^{AMR} contribute to $S_{XX}(\phi)$ with opposite signs [38], with the consequence that if the artifact contributions are neglected in the conventional ST-FMR analysis, the result is an underestimate of the strength of τ_{DL}^{0}. In this respect our results conflict with some conclusions [26, 6] that neglecting the SP/ISHE contribution produces an overestimate of τ_{DL}^{0}.

Analysis of the dependence of $1/\xi_{FMR}$ as a function of $1/t_{FM}$ allows a determination of the underlying spin-torque efficiencies ξ_{DL} and ξ_{FL} using Eq. (1.39). The results for the CoFeB series of samples is shown in Fig. 3(b). If one does not correct for the contribution of the artifacts, the calculated values of $1/\xi_{FMR}$ depart upward from the expected linear dependence for $t_{FM} \gtrsim 6$ nm. Similar results have been reported previously in [37] where the non-linearity was speculated to be from SP/ISHE, and the spin-torque efficiencies were determined by fitting only to the thinner FM stacks. After we correct for the artifact contribution, we find good agreement with the expected linear dependence over the full thickness range. From the linear fit, we determine $\xi_{DL} = 0.090(6)$ and $\xi_{FL} = -0.020(2)$.

For the Pt(6 nm)/Py(8 nm) and Pt(6 nm)/CoFe(6 nm) samples we find the same configuration of signs as for the thicker Pt/CoFeB samples: V_{art} partially cancels S_{XX}^{AMR} so that the true mixing signal is larger than the measured

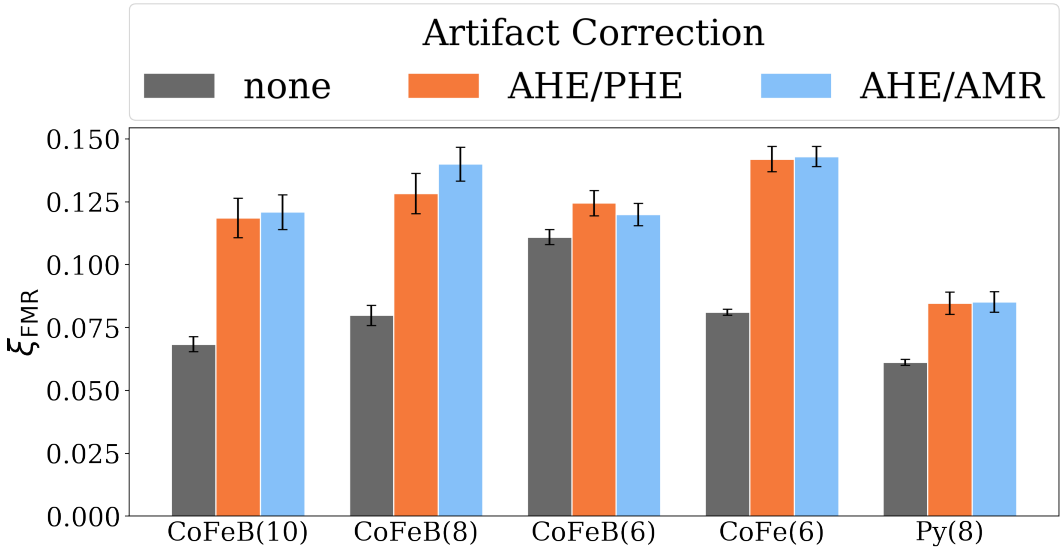

Figure 1.8: ξ_{FMR} for various device stacks. The gray (left) bars show values without correction for the artifacts, and the orange and blue (center, right) bars show values corrected using the determination of the artifact voltages using Eqs. (1.37a) and (1.37b), respectively.

amplitude of $S_{\mathrm{XX}}(\phi)$. The results of the calculation of ξ_{FMR} according to Eq. (1.38) are shown in Fig. 1.8 for five selected samples, both without and with the correction for artifacts. In determining ξ_{FMR} we use values for M_s determined by room temperature vibrating sample magnetometry (VSM) and values for $\mu_0 M_{\mathrm{eff}}$ determined by fits of the ST-FMR resonant fields as a function of frequency. These values are: for CoFeB $M_s = 9.8 \times 10^5$ A/m, $\mu_0 M_{\mathrm{eff}} = 0.6$ – 1.4 T (depending on thickness); for Py $M_s = 7.5 \times 10^5$ A/m, $\mu_0 M_{\mathrm{eff}} = 1.01$ T; and for CoFe $M_s = 9.1 \times 10^5$ A/m, $\mu_0 M_{\mathrm{eff}} = 1.66$ T. If a magnetic dead layer was observed in VSM, the dead layer thickness was subtracted from t_{FM}. In all cases shown in Fig. 4, we find that correcting for the artifact contribution increases our estimates for the values of ξ_{FMR}. The value of ξ_{FMR} is smaller for the Pt/Py sample than for Pt/CoFeB or Pt/CoFe primarily because ξ_{FL} is both small and has a positive sign for Pt/Py [39, 40].

The dependence of the artifact voltage, V_{art}, on the ferromagnetic layer thickness is shown in Fig. 1.9 for the longitudinal ST-FMR component of the Pt/CoFeB series of samples.

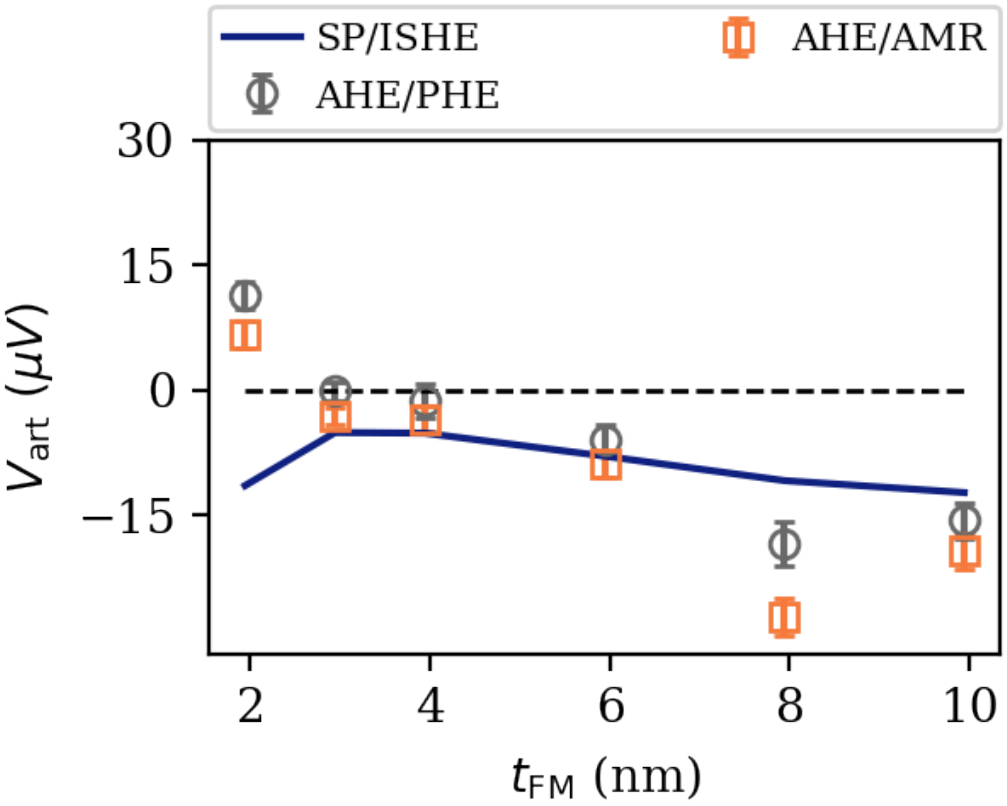

Figure 1.9: The artifact voltage as a function of the FM thickness in Pt(6 nm)/CoFeB samples. The two types of data points reflect the two correction equations ((1.37a) and (1.37b)). The line is the estimated SP/ISHE contribution, determined using the parameters described in the text, with no adjustable parameters.

The data are compared to an estimate of the SP/ISHE contribution from Eq. (1.27), using the parameters (appropriate for the resistivity of our Pt layers, $\rho_{Pt} = 20.4\ \mu\Omega$cm): $\theta_{SH} = 0.32$ [41, 37], $g_{eff}^{\uparrow\downarrow} = 8.26 \times 10^{18}$ m^{-2} [41], and $\lambda_{sd} = 3.7$ nm [42]. The other quantities in Eq. (1.27) were measured for our samples, including the variation as a function of CoFeB thickness. The comparison therefore includes no adjustable fitting parameters, but given that there is considerable disagreement in the literature about the values of the parameters θ_{SH}, $g_{eff}^{\uparrow\downarrow}$, and λ_{sd}, one should still be careful about drawing quantitative conclusions. The comparison indicates to us that for the samples with $t_{FM} \geq 3$ nm the SP/ISHE theory predicts the correct sign and can roughly capture the overall magnitude and thickness-dependence of the measured artifact sig-

nal. However, the measured artifact voltage for t_{FM}= 2 nm has the opposite sign, inconsistent with the SP/ISHE. We are confident that the measured sign change is real, because we have measured and performed the analysis on five Pt(6 nm)/CoFeB(2 nm) devices with varied geometries, with consistent results.

Given that the SP/ISHE cannot explain the sign change in the artifact voltage for our t_{FM}= 2 nm samples, we suggest that resonant heating effects might be comparable to the SP/ISHE in our Pt(6 nm)/CoFeB samples, with sufficient strength to reverse the overall sign of the artifact voltage for our thinnest samples. This suggestion differs from previous studies on Pt/YIG samples, for which frequency-dependent measurements demonstrated that SP/ISHE signals dominate over resonant heating artifacts [25, 43]. However, the relative strength of the heating effects and SP/ISHE should scale proportional to the damping α (compare Eqs. (1.27) and (1.34)), so that the heating effects should be more significant in higher-damping ferromagnetic metals compared to lower-damping YIG. We calculate that the resonant heating due to the excitation of magnetic precession for our 2 nm samples is $\sim 2.5 \times 10^4$ Wm^{-2}, only about a factor of 5 less than the Ohmic heating per unit area in the CoFeB, $\sim 1.2 \times 10^5$ Wm^{-2} (see Fig. 1.3). We suggest that this is sufficient to measurably alter the thermal gradients within the sample at resonance and induce resonant signals from the LSSE and/or Nernst effects. Due to an increase in the damping coefficient α with decreasing magnetic thickness, the ratio of the resonant heating to Ohmic heating is significantly greater for the 2 nm CoFeB samples than for the thicker magnetic layers (see Fig. 1.3)..

As noted in the introduction, past experiments have shown a discrepancy between measurements of ξ_{DL} using low frequency second harmonic Hall and ST-FMR techniques. To see if our correction for the artifact voltages in ST-FMR alleviates the discrepancy between the two techniques, we carried out low frequency second harmonic Hall measurements on the same Pt/CoFeB bilayers, but found that the low frequency second harmonic measurements of ξ_{DL} were

still approximately 60% larger than what we measured by ST-FMR, even after correcting ST-FMR for spin pumping and resonant heating. This persisting quantitative difference suggests that the assumptions used in analyzing one or both of these experiments are missing an important bit of physics. Our analysis indicates that this missing physics is not simply the neglect of spin pumping or a simple heating-induced voltage in the ST-FMR results, and therefore more work must be done to understand the source of the disagreement.

1.6 Conclusions

In conclusion, we have demonstrated that the rectification signal used to measure the strength of spin-orbit torques in spin-torque ferromagnetic resonance (ST-FMR) can be separated from artifact voltages that may arise due to spin pumping and resonant heating by performing ST-FMR in the transverse (Hall) configuration as well as the usual longitudinal configuration. For Pt(6 nm)/ CoFeB(t_{FM}) samples, the artifact voltages are small compared to the rectification signal for $t_{\mathrm{FM}} < 6$ nm, but they can become a significant part of the measured signal for thicker magnetic layers. The sign and overall magnitude of the measured artifact voltage for these thicker layers are consistent with expectations for the SP/ISHE effect signal. However, the sign of the artifact voltage is reversed for our thinnest magnetic layers, with $t_{\mathrm{FM}} = 2$ nm. This sign reversal cannot be explained by the SP/ISHE, so we suggest that it may be caused by a resonant heating effect.

Chapter 2

DC-biased ST-FMR

2.1 Introduction

In addition to the method of ST-FMR described in the previous chapter, where a resonance lineshape (LS) is measured, fitted, and from the fits, SOT magnitudes are extracted, there is another method of doing ST-FMR. In this other method, which we will call dc-biased ST-FMR or the linewidth (LW) analysis of ST-FMR (contrasted with the LS method of ST-FMR described in the previous section), a dc current is applied device in addition to the microwave current along the same path. In a HM/FM bilayer, the dc current produced dc damping-like SOTs (e.g. through the spin Hall effect) in the HM that impinge on the FM causing a rescaling of the FMs damping. Like any harmonic system, the damping is closely related to the LW of the measured resonant signal. Therefore, the applied dc current will rescale the LW of the measured resonance, so a variation of the LW with different amounts of applied dc current is measured and, from this, the size of the damping-like SOTs can be quantified.

There is also a known issue with this LW technique where it can result in very unreasonable numbers for the SOT that very much disagree with other corroborating measurement techniques. This is a common issue in measurements performed by the Ralph/Buhrman groups and has eroded our groups' trust in the technique. Also consistent disagreement between LS and LW methods of

ST-FMR can be found in the literature, e.g. refs. [44, 45]. An explanation for these frequent discrepancies has, so far, been lacking.

In this chapter, we closely analyze both the LS and LW methods of ST-FMR on bread-and-butter Pt/Py samples. We find that the results of the LS and LW methods disagree, and that the disagreement is almost all due to shortcomings of the LW method. Fitting the measured signals to the conventional models of ST-FMR, we find that significant fit residuals remain that originate from periodic heating and from an interface-localized FM layer that has different dynamics from the FM bulk. The latter contribution has a very broad LW is highly sensitive to the application of dc current, so the application of dc current affects this interfacial layer, causing a spurious interfacial contribution to the measured linewidth of the as-measured resonance signal. We also find that there is a reliable, systematic way to remove this spurious LW contribution to the LW method of ST-FMR, which we call "windowed fitting." This entails sequentially fitting the measured data over a smaller and smaller range (window) centered about the resonance field i.e. discounting more and more data. We find that, as the window gets smaller, the result of the LW method of ST-FMR approaches the result measured from the LS analysis and eventually the two agree. This data analysis prescription offers a novel and reliable way to consider the LW ST-FMR data and ensure consistent results, free from spurious effects.

In the following, much is taken and adapted from Ref. [46].

2.2 Background and Theory

During ST-FMR, a microwave current is applied in-plane into a heavy metal/ferromagnet bilayer, so that current-induced SOTs and Ørsted fields induce ferromagnetic precession. Magnetic precession causes resistance variations in the device due to anisotropic magnetoresistance. Mixing between the microwave current and resistance oscillations then produces a DC voltage that is measured. The signal-to-noise ratio (SNR) is vastly improved if an endogenous parameter of the tech-

nique is modulated and the voltage is measured with a lock-in amplifier. There are a number of choices for the modulated parameter: amplitude modulation (AM) [8, 47], magnetic field modulation [48], frequency modulation (FM), or phase modulation (the latter two of which are equivalent). Save a few works that have employed magnetic field modulation [48, 49, 50, 51, 52, 45], almost all experiments featuring ST-FMR employ AM because it is the simplest parameter to modulate – it does not complicate the experimental apparatus nor the fitted model.

Typically, one assumes that a macrospin approximation is appropriate for describing the current-induced magnetic dynamics for experiments performed at sufffficiently large microwave frequencies and magnetic fields, in which case the results of ST-FMR are modeled by the Landau-Lifshitz-Gilbert-Slonczewski (LLGS) equation

$$\dot{\mathbf{m}} = -\gamma \mathbf{m} \times \mathbf{B} + \alpha \mathbf{m} \times \dot{\mathbf{m}} + \boldsymbol{\tau} \tag{2.1}$$

where $\mathbf{m}$ is the magnetic moment, $\gamma = 2\mu_B/\hbar$ is the gyromagnetic ratio, $\mathbf{B}$ is the external field, α is the Gilbert damping constant, and $\boldsymbol{\tau} = \boldsymbol{\tau}_{\mathrm{DL}} + \boldsymbol{\tau}_{\mathrm{z}}$ describes the torque present in our system. The torques produced by a polycrystalline thin film must obey the Rashba symmetry [53]. For a film spanning the $X-Y$ plane, with current flowing along the X-direction we have

$$\boldsymbol{\tau}_{\mathrm{DL}} = \tau^0_{\mathrm{DL}}(\mathbf{m} \times (\mathbf{m} \times Y)) = \frac{\xi_{\mathrm{DL}}\mu_B}{eM_s t_{\mathrm{FM}}} J_e \cos\phi_0 \tag{2.2}$$

$$\begin{aligned} \boldsymbol{\tau}_{\mathrm{z}} &= \tau^0_{\mathrm{z}}(\mathbf{m} \times Y) \\ &= \left[\frac{\xi_{\mathrm{FL}}\mu_B}{eM_s t_{\mathrm{FM}}} + \frac{\gamma\mu_0 t_{\mathrm{HM}}}{2}\right] J_e \cos\phi_0. \end{aligned} \tag{2.3}$$

$\xi_{\mathrm{DL(FL)}}$ is the damping-like (field-like) SOT efficiency, μ_B is the Bohr magneton, M_s is the saturation magnetization of the ferromagnet, $t_{\mathrm{F(N)}}$ is the thickness of the ferromagnet (normal metal) layer, μ_0 is the vacuum permeability, J_e is the electric current density flowing through the heavy metal, and ϕ_0 is the angle

between the direction of applied field and current flow (X-direction). Solutions to the LLGS equation for a sample with in-plane magnetic anisotropy predict that resonant ferromagnetic precession will occur when the Kittel equation, $\omega_0 = \gamma\sqrt{B(B+\mu_0 M_{\text{eff}})}$ [2], is satisfied. Here, $\mu_0 M_{\text{eff}} = \mu_0 M_s - 2K_\perp/M_s$ accounts for shape anisotropy minus any out-of-plane anisotropy. The total resonance lineshape will have contributions from symmetric (S) and antisymmetric (A) Lorentzians [54, 8], which we define as

$$S = \frac{\Delta^2}{(B-B_0)^2+\Delta^2} \tag{2.4}$$

$$A = \frac{\Delta(B-B_0)}{(B-B_0)^2+\Delta^2} \tag{2.5}$$

where B_0 is the resonance field, and Δ is the half-width-at-half-maximum linewidth related to the Gilbert damping by $\Delta = \alpha\omega/\gamma$. The DC mixing signal is a weighted sum of these two lineshapes with coefficients V_S and V_A determined by the the torques and material parameters in our system [8, 54, 11]

$$V_{\text{mix}} = V_S S + V_A A + C \tag{2.6}$$

with

$$\begin{aligned} V_S &= \frac{I_{\text{rf}}}{2\alpha\omega^+} R_{\text{AMR}} \tau_{\text{DL}}^0 \sin 2\phi_0 \cos\phi_0 \\ V_A &= \frac{I_{\text{rf}}}{2\alpha\omega^+} R_{\text{AMR}} \frac{\omega_2}{\omega} \tau_{\text{z}}^0 \sin 2\phi_0 \cos\phi_0. \end{aligned} \tag{2.7}$$

I_{rf} is the total microwave current that flows through the bilayer, $\omega^+ = \gamma(2B_0 + \mu_0 M_{\text{eff}})$, R_{AMR} is the amplitude of the anisotropic magnetoresistance of the whole bilayer, and $\omega_2 = \gamma(B_0 + \mu_0 M_{\text{eff}})$. C is a constant voltage offset that is included to account for non-resonant signals. For samples with thick magnetic layers, there can also be a significant additional contribution to the symmetric resonance component from spin pumping/resonant heating and the inverse spin Hall effect [11] that we will mention below.

The experimental signal-to-noise ration (SNR) is significantly improved by modulating the microwave amplitude; this is captured by letting $V_{\text{mix}}(I_{\text{rf}}) \to V_{\text{mix}}(I_{\text{rf}}(1+\mu\cos\omega_m t)) \approx V_{\text{mix}} + 2\mu V_{\text{mix}}\cos\omega_m t$ where $\mu \in [0,1]$ is the AM-depth. A lock-in amplifier demodulates the total signal by mixing with a $\cos\omega_m t$ reference and applying a low-pass filter. The AM signal is therefore simply: $2\mu V_{\text{mix}}$.

If, alternatively, frequency modulation is used instead of amplitude modulation, the expected FM signal can be derived in a similar manner. We let $V_{\text{mix}}(\omega) \to V_{\text{mix}}(\omega + \delta\omega\cos\omega_m t)$ where $\delta\omega \ll \omega$; this admits the simple expansion near the microwave carrier frequency, ω_c

$$\begin{aligned} &V_{\text{mix}}^{\text{FM}}(\omega) = V_{\text{mix}}(\omega + \delta\omega\cos\omega_m t) \implies \\ &V_{\text{mix}}^{\text{FM}}(\omega) \approx V_{\text{mix}}(\omega_c) + \frac{dV_{\text{mix}}}{d\omega}\Big|_{\omega=\omega_c}\delta\omega\cos\omega_m t. \end{aligned} \tag{2.8}$$

$V_{\text{mix}}^{\text{FM}}$ is again demodulated by a lock-in amplifier, which leaves us with only $\frac{dV_{\text{mix}}}{d\omega}\big|_{\omega=\omega_c}\delta\omega$. Therefore, the ratio of the detected mixing signal to the amplitude of the frequency modulation is

$$\begin{aligned} V_{\text{mix}}^{\text{FM}}/\delta\omega &= \frac{\partial V_{\text{mix}}}{\partial\omega}\Big|_{\omega=\omega_c} \\ &= \frac{\partial V_S}{\partial\omega}S + \frac{\partial V_A}{\partial\omega}A \\ &+ \frac{1}{\omega_c}\left[2V_S A^2 + V_A\left(2A^3/S - A\right)\right] \\ &+ \frac{\omega_c}{M_{\text{eff}}\gamma^2\Delta}\left[2V_S SA + V_A\left(A^2 - S^2\right)\right] + C. \end{aligned} \tag{2.9}$$

Here we have used that $\partial_\omega S = 2S\left[(1-S)\partial_\omega\Delta + A\partial_\omega B_0\right]/\Delta$ and $\partial_\omega A = \left[A(1-2S)\partial_\omega\Delta - (S+2A^2)\partial_\omega B_0\right]/\Delta$. Equation (2.9) is nearly identical to a previously derived result where the magnetic field was modulated [48]. Compared to the AM result, Eq. (2.6), the FM result has two additional fit parameters, $dV_S/d\omega$ and $dV_A/d\omega$ to account for possible frequency dependence of microwave transmission through the measuring circuit to the device.

Lineshape (LS) Analysis

After measuring with either amplitude or frequency modulation and then fitting the ST-FMR resonance to determine V_S and V_A using either Eq. (2.6) or Eq. (2.9), the torque efficiencies may be determined directly from Eq. (2.7) if I_{rf} is well-calibrated, since the other parameters in Eq. (2.7) are independently-measurable. However, since it is often challenging to determine accurately the value of I_{rf} within the sample, we generally prefer to determine the torque efficiencies by taking appropriate ratios of V_S and V_A [37]. We first calculate an intermediate quantity, ξ_{FMR}, defined as

$$\xi_{\mathrm{FMR}} = \frac{V_S}{V_A} \frac{e \mu_0 M_s t_{\mathrm{HM}} t_{\mathrm{FM}}}{\hbar} \sqrt{1 + \frac{\mu_0 M_{\mathrm{eff}}}{B_0}}. \tag{2.10}$$

By using Eqs. (2.2), (2.3), & (2.10), as long as the torque efficiencies are independent of the ferromagnetic-layer thickness in the range of thickness we analyze, then ξ_{FMR} can be related to the damping-like and field-like torque efficiencies as [37]

$$\frac{1}{\xi_{\mathrm{FMR}}} = \frac{1}{\xi_{\mathrm{DL}}} \left(1 + \frac{\hbar}{e} \frac{\xi_{\mathrm{FL}}}{\mu_0 M_s t_{\mathrm{HM}} t_{\mathrm{FM}}} \right). \tag{2.11}$$

Therefore, by taking results form a series of samples with different ferromagnet thicknesses, t_{FM}, we can then determine ξ_{DL} and ξ_{FL} from a linear fit of $1/\xi_{\mathrm{FMR}}$ versus $1/t_F$.

Linewidth (LW) Analysis: Change of Linewidth Versus DC Current

In DC-biased ST-FMR, a DC current is applied parallel to the microwave current, such that the damping-like torque from the DC current rescales the effective Gilbert damping of the magnetic layer and causes the resonance linewidth to change linearly as a function of I_{DC}. The damping-like SOT efficiency can

be calculated from DC-current linewidth modulation as [8, 40]

$$\xi_{\mathrm{DL}} = \frac{eM_s\omega^+ t_{\mathrm{FM}}}{\hbar\omega_c \sin\phi_0}\frac{Wt_{\mathrm{HM}}}{x}\frac{d\Delta}{dI_{\mathrm{DC}}} \tag{2.12}$$

where W is the width of the current-carrying channel and x is the fraction of the total DC current that flows through the HM.

2.3 Measurements

All our samples are grown using DC-magnetron sputtering (in a system with base pressure $< 4 \times 10^{-8}$ torr) onto a surface-passivated high-resistivity Si wafer ($\rho >$ 20,000 Ωcm). Each sample is grown in an independent deposition. Samples shown in the main text have the stacking order: Substrate/Ta(1 nm)/Pt(6 nm)/Py(t_{FM})/Al(1 nm), with the magnetic layer being Permalloy (Py = $Ni_{81}Fe_{19}$). The Ta is used as a seed layer to promote smooth growth and the Al is oxidized upon exposure to air an is used as a capping layer to prevent oxidation of the Py. The Pt ($\rho = 20.4$ $\mu\Omega$cm) and Py ($\rho = 25$ $\mu\Omega$cm) are far more conductive than the Ta or oxidized Al so we assume all of the current flows through just the Pt and Py layers. Analogous results for which the Py is substituted with $Co_{40}Fe_{40}B_{20}$ are also shown.

After growth, we pattern the samples into rectangular bars of varying dimension using photolithography and Ar ion milling. The devices have dimensions: 40 μm $\times$ 80 μm, 20 μm $\times$ 60 μm, or 20 μm $\times$ 80 μm. All measurements shown in this work are taken on 20 μm $\times$ 80 μm devices, and the quantitative conclusions do not depend on the device geometry. We attach Ti(3 nm)/Pt(75 nm) contacts to the devices by another step of photolithography, DC-magnetron sputtering, and lift-off.

All data shown are measured on microwave-compatible Hall-bar structures that allow measurements of both longitudinal and transverse mixing voltages, as described in ref. [11]. Here, we will analyze only the longitudinal mixing

voltages, as that is the usual ST-FMR measurement geometry. The devices are connected to the circuit shown in Fig. 2.1(b). A RF source inputs a microwave current into the device through the AC port of a bias tee with either amplitude or frequency modulation (Fig. 2.1(a)), while the magnitude of an external magnetic field is swept at a fixed angle ϕ_0 through the Kittel resonance condition. The DC voltage along the longitudinal direction generated by mixing is detected with a lock-in amplifier that references the modulating signal. For the DC-biased measurements, an additional DC current is applied through the DC port of the bias tee to flow through the device in addition to the microwave current. All measurements are performed at room temperature.

Measurements in the main text are performed at a 10 GHz carrier frequency ($f_c = \omega_c/2\pi$). The modulating signal for both AM and FM measurements is applied at 1.7 kHz modulation frequency ($f_m = \omega_m/2\pi$). The external magnetic field is applied at $\phi_0 = 45°$ with respect to the direction of applied microwave current. The AM measurements are done with 100% AM-depth as depicted in Fig. 2.1(a) to maximize the measured signal. We find that reducing the AM-depth has no effect on the results shown. The FM measurements are done with a frequency deviation ($\delta f = \delta\omega/2\pi$) of 16 MHz. Both the AM and FM are applied by the internal circuitry of the RF source, an Agilent 8257D. Both the 16 MHz frequency deviation and the 1.7 kHz modulation frequency are far smaller than the carrier frequency of 10 GHz, so that within either measurement mode the modulation has negligible effect on the microwave current over one precession cycle, a key assumption of the modeling.

2.3.1 Results of Lineshape Analyses

Examples of the longitudinal resonant mixing signals from a Pt(6 nm)/Py(5 nm) sample for both the AM and FM measurements are shown in Fig. 2.2.

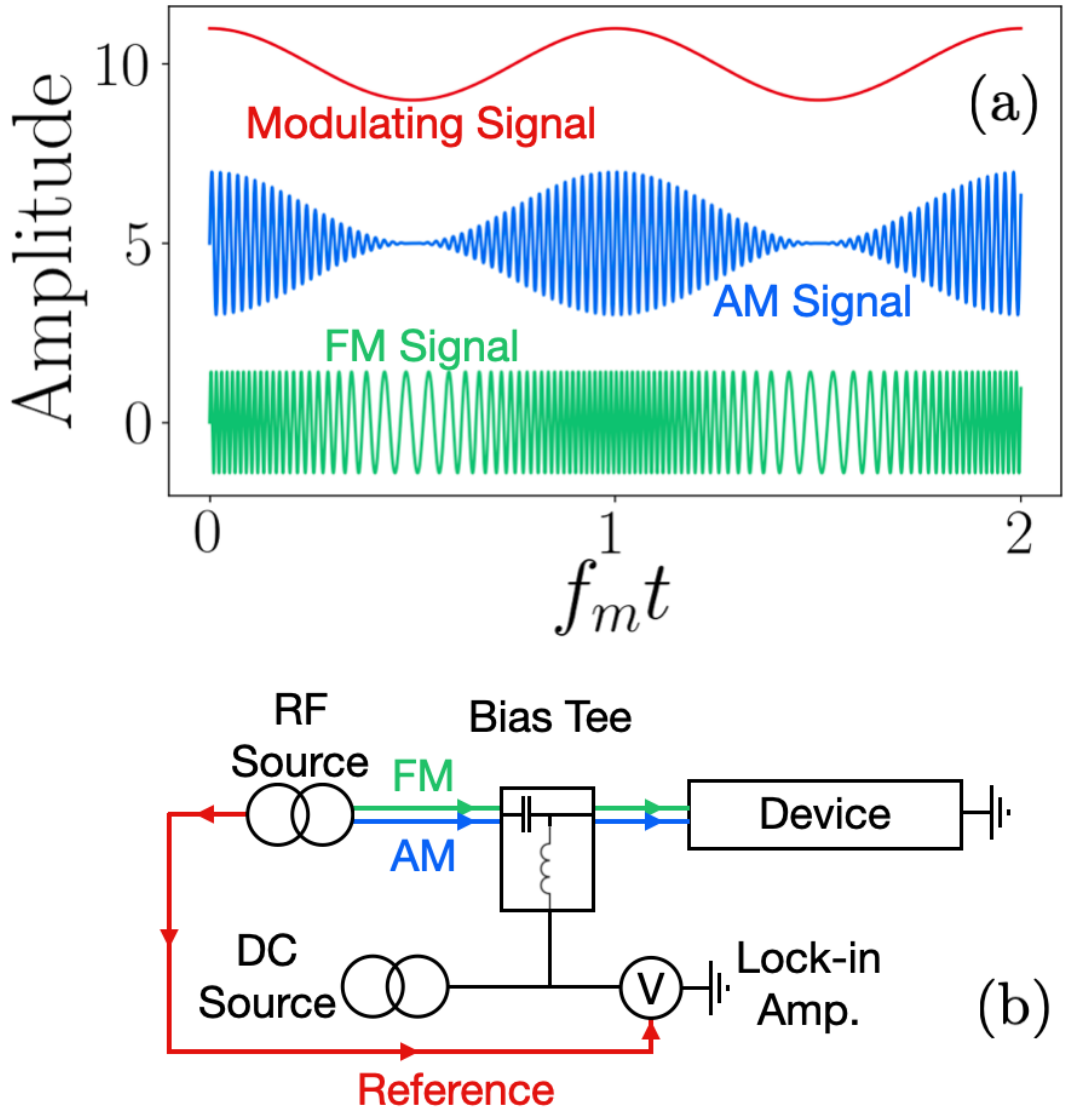

Figure 2.1: The measurement setup used in this Chapter. **(a)** Schematic representations of the time dependence of microwave current that is injected into the device under test for amplitude-modulated and frequency-modulated experiments. Offsets are added and the scale of the frequency modulation is exaggerated for clarity. **(b)** The circuit used in this measurement. The colors of the wires correspond to the colors of the signals in the top panel which the wire carries.

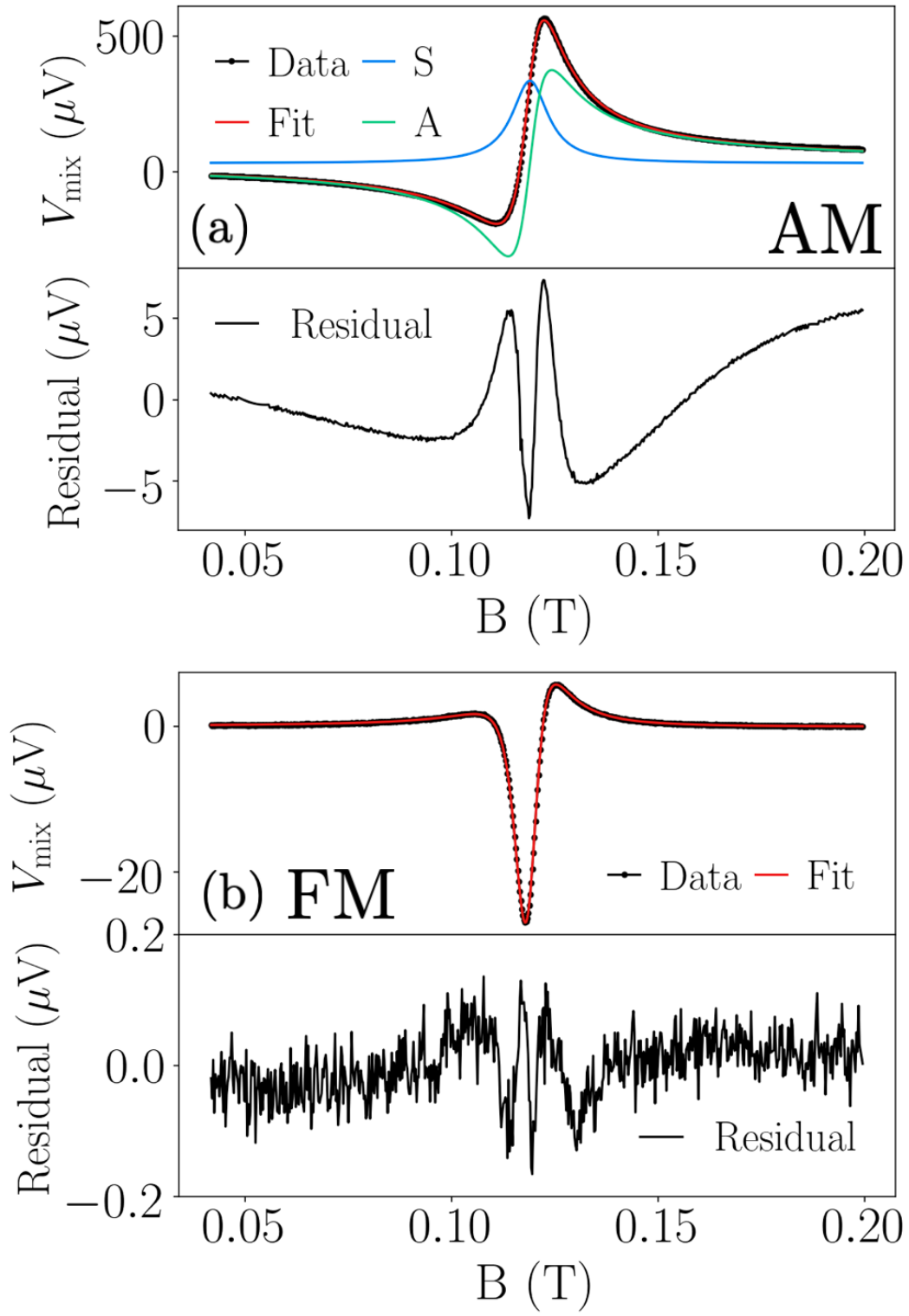

Figure 2.2: Examples of measured resonances and fit residuals for a Pt(6 nm)/Py(5 nm) sample at 20 dBm, 10 GHz, $\phi_0 = 45°$, $f_m = 1.7$ kHz, $I_{\mathrm{DC}} = 0$. **(a)** AM resonance taken at 100% AM-depth with a fit to Eq. (2.6). **(b)** FM resonance taken $\Delta f = 16$ MHz with a fit to Eq. (2.9). The range of magnetic field shown here corresponds to $[B_0 - 15\Delta,\ B_0 + 15\Delta]$ for the primary resonance.

The AM measurement (Fig. 2.2(a)) is fit to Eq. (2.6) with the five fit parameters V_S, V_A, C, B_0, Δ while the FM measurement (Fig. 2.2(b)) is fit to Eq. (2.9) including the two additional fit parameters $dV_S/d\omega, dV_A/d\omega$. The fit to the AM measurement looks good by eye, but the best fit nevertheless produces significant systematic residuals ($=V_{\text{mix}}^{\text{measured}} - V_{\text{mix}}^{\text{best-fit}}$), which hints that the framework of conventional ST-FMR analysis (Eq. (2.6)) gives an incomplete description.

To rule out spurious measurement artifacts, we have repeated the AM measurements on three independent ST-FMR apparatuses at Cornell and have also performed measurements on different sample stacks; all of these measurements show the same systematic residuals for the AM fits. In contrast, for the FM measurements the scale of the residuals after fitting to Eq. (2.9) is significantly smaller relative to the full signal magnitude.

For the AM fits in Fig. 2.2(a), we see that the residuals have a lineshape near the resonance field that closely resembles a Lorentzian derivative, suggesting that an additional parameter in Eq. (2.6) is varying at the modulation frequency and contributing to the homodyne mixing signal. Quantitative estimates suggest that a varying M_{eff} will contribute far more than other candidate sample parameters and that an M_{eff} oscillating at the AM frequency, presumably due to heating, can result in the residual lineshape we observe near the resonance field. That is, suppose (in addition to the amplitude modulation of I_{RF}) that M_{eff} also varies periodically as $M_{\text{eff}} \rightarrow M_{\text{eff}} + \delta M_{\text{eff}} \cos \omega_m t$; this, analogously to the frequency modulation, would allow the expansion

$$\begin{aligned} &V_{\text{mix}}(M_{\text{eff}} + \delta M_{\text{eff}} \cos \omega_m t) \\ &\approx V_{\text{mix}}(M_{\text{eff}}) + \frac{\partial V_{\text{mix}}}{\partial M_{\text{eff}}} \delta M_{\text{eff}} \cos \omega_m t. \end{aligned} \tag{2.13}$$

The total mixing signal will thus consist of the sum of two terms that vary

periodically with the AM

$$\left(2\mu V_{\text{mix}} + \frac{\partial V_{\text{mix}}}{\partial M_{\text{eff}}}\delta M_{\text{eff}}\right)\cos\omega_m t \tag{2.14}$$

and *both* will be demodulated by the lock-in amplifier. To confirm that the residuals can arise from heat-driven M_{eff} oscillation, we measure M_{eff} while heating the sample. We find that the measured M_{eff} is sensitive to the sample temperature as shown in Fig. 2.3.

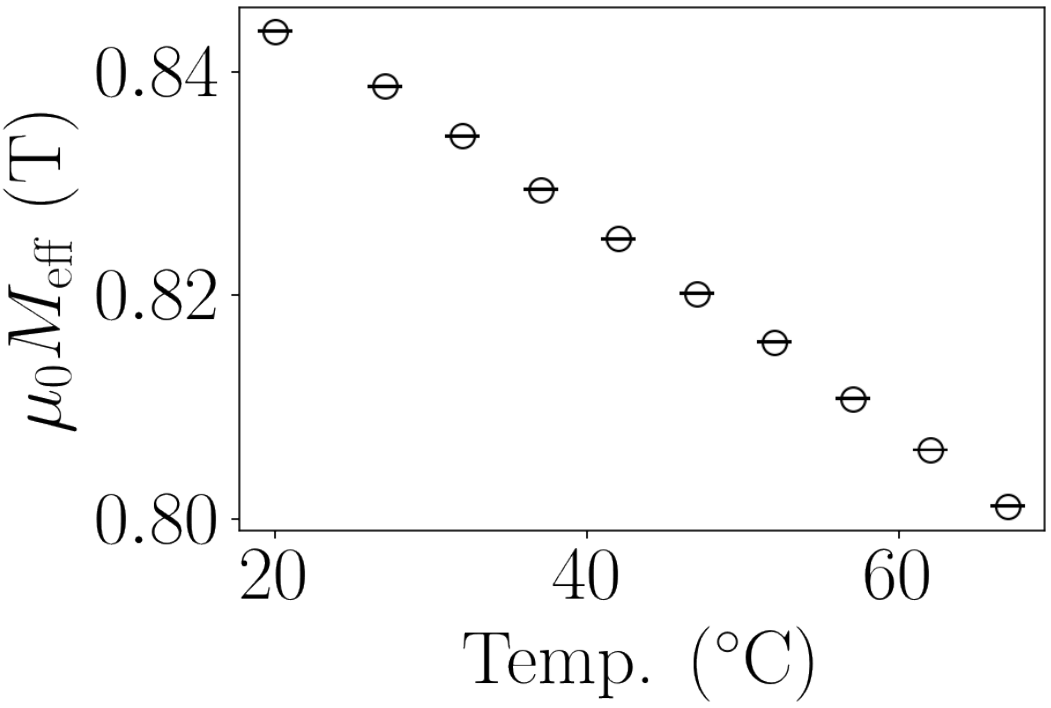

Figure 2.3: The effective magnetization $\mu_0 M_{\text{eff}}$ vs. sample temperature. The sample was heated with a substrate heater placed under the device substrate.

A homodyne signal from an oscillating value of M_{eff} cannot by itself explain the full residual in the AM fits; in addition the AM residuals appear to contain an ordinary AM resonance lineshape (Eq. (2.6)) with a very large linewidth. In Fig. 2.4 we show the fit residuals of an AM measurement taken on a Py(3 nm) sample (with no DC current bias). We fit the residuals to the sum of a homodyne signal corresponding to an oscillating value of M_{eff} (green curve) and a large-Δ resonant background (Eq. (2.6)) (blue) with $\Delta_{\text{large}} = 41.6$ mT, much larger than the value $\Delta = 7.3$ mT for the primary resonance. The sum of

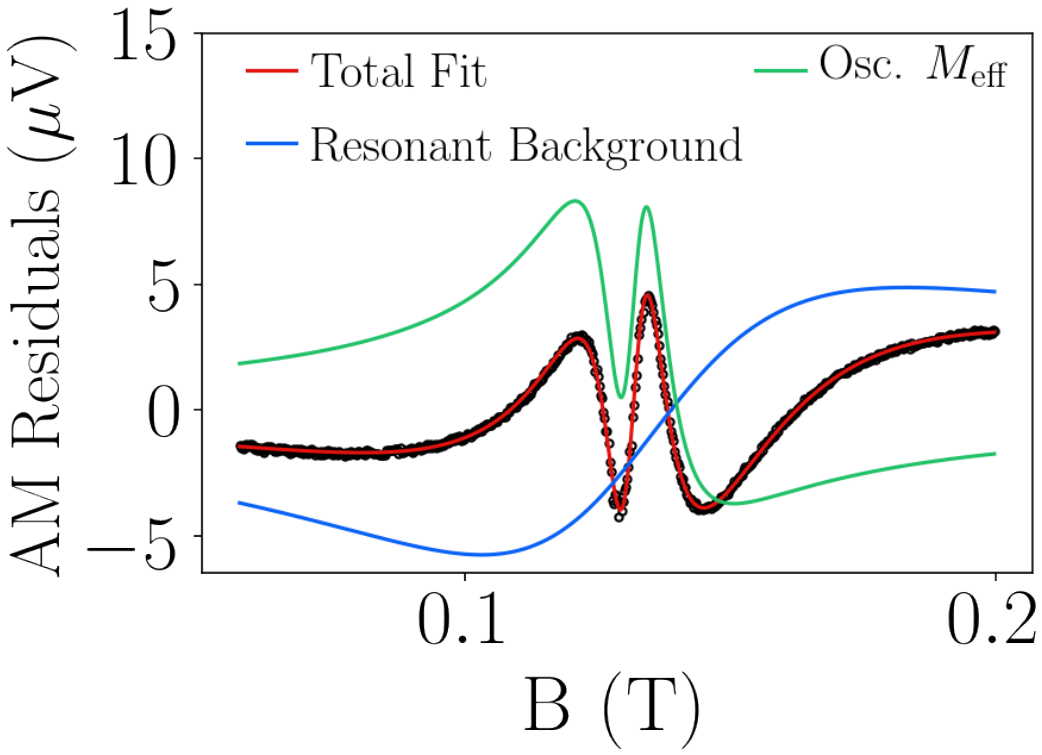

Figure 2.4: **(a)** Measured fit residuals for an AM measurement of a Py(3 nm) sample taken at zero DC bias, with a fit to the sum of contributions from a heating-induced oscillation of M_{eff} and a large-Δ resonant background. The linewidth of the primary resonance for Py(3 nm) samples is greater than for Py(5 nm) samples, so the range of magnetic field shown here still corresponds to $[B_0 - 15\Delta,\ B_0 + 15\Delta]$ for the primary resonance.

the two contributions (red curve) fits the residuals very well. Based on direct measurements of M_{eff} versus temperature on the same device $[d(\mu_0 M_{\text{eff}})/dT = 8 \times 10^{-4}$ T/°C], the scale of the temperature oscillations needed to produce the oscillating-M_{eff} homodyne signal is approximately 1°C. V_S and V_A for the large-Δ resonance for the data in Fig. 2.2 are 12 μV and 7 μV, while for the primary resonance $V_S = 311$ μV and $V_A = 684$ μV.

We have considered two options for the origin of the large-Δ resonance: a region of increased damping (a) near the sample edges or (b) near a magnetic interface. If the origin were due to increased damping near the sample edges, we would expect the ratio of the amplitudes for the large-Δ and primary resonances to scale inversely with the sample width and to be approximately independent of the ferromagnetic-layer thickness. Instead, we find that this ratio is insensitive

to the sample width (a change of $< 10\%$ in the symmetric and $< 4\%$ in the antisymmetric component upon changing the sample width by a factor of 2), while it is sensitive to the ferromagnetic layer thickness as shown in Fig. 2.5.

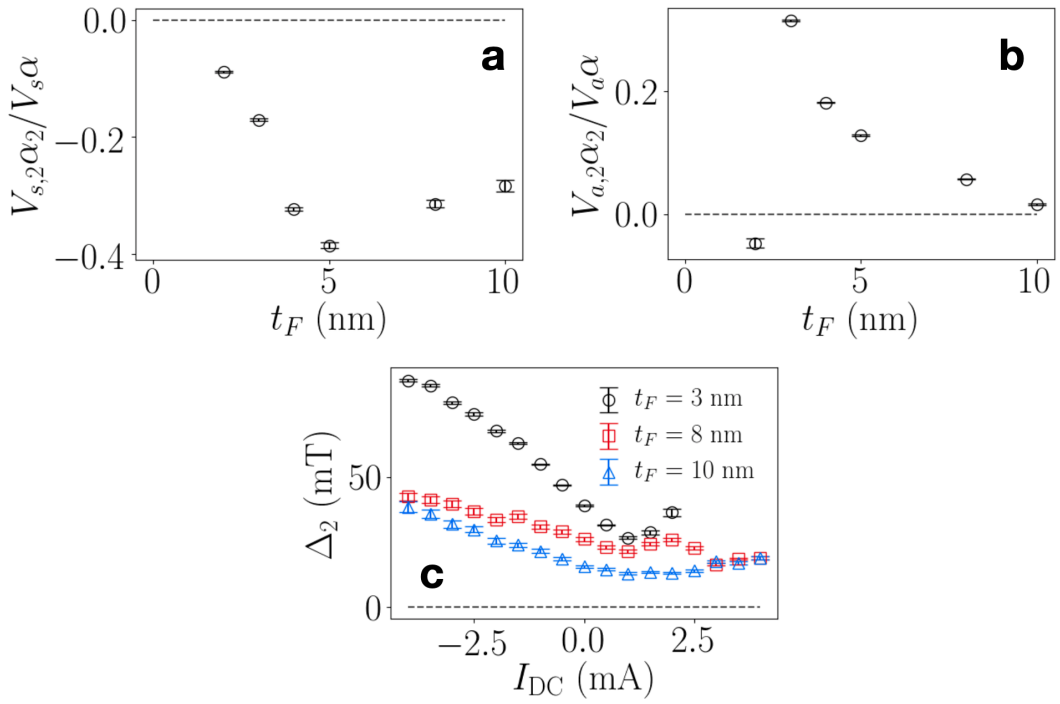

Figure 2.5: Measured and fitted parameters of the broad-linewidth resonance in the residual signal as a function of ferromagnet thickness and dc current. Subscript 2's indicate that the quantity is a result of the fit to the broad-resonance residual signal, while variables without a subscript 2 are from the primary, measured resonance.

This suggests that the portion of the sample with increased damping is an interfacial region. Additional evidence for an origin associated with the heavy-metal/ferromagnet interface in Fig. 2.5 comes from the fact that the large-Δ linewidth is very sensitive to applied DC current, consistent with a very thin and/or low-moment region under the influence of the spin current generated by the heavy metal.

Our observations might be related to recent findings from the IBM group of interfacial regions in CoFeB/MgO/CoFeB magnetic tunnel junctions whose dynamics can become partially decoupled from the bulk of the magnetic films [55, 56]. The two experiments differ, however, in that the IBM work deduced a difference in effective magnetic anisotropy (compared to the bulk of the mag-

netic film) for the interfacial layers at CoFeB/MgO interfaces, while in our devices the large-Δ resonance corresponds to an increased damping near a Pt/ferromagnet interface without a large difference in anisotropy.

We suggest that there are two reasons why the fit residuals for the FM measurements are reduced compared to the AM measurements. First, temperature oscillations at the modulation frequency will be smaller for the FM measurements because the magnitude of I_{RF} will be approximately constant in time, so Ohmic heating caused by I_{RF} will also be approximately constant rather than oscillating at the modulation frequency. Temperature oscillations will not be eliminated completely however, since FM near the resonance will cause the energy absorbed by resonant heating of the magnetic layer (energy transfer associated with magnetic excitation by the current-induced torques) to oscillate at the modulation frequency. We suggest that this resonant heating is likely the main cause of the small remaining systematic residuals near the resonance field in the fits to the FM data (Fig. 2.2(b)). Second, contributions from the large-Δ resonance to the FM measurements are reduced precisely because the linewidth is so broad, so this part of the signal is relatively insensitive to variations in applied frequency.

If one proceeds with the standard ST-FMR macrospin analysis – Eqs. (2.10), (2.11) – (ignoring the residuals for now) the resulting values of $1/\xi_{\mathrm{FMR}}$ for both the AM and FM measurements are shown in Fig. 2.6 for samples with ferromagnet layer thicknesses t_F varying from 2 nm to 10 nm.

The samples with the thickest ferromagnet layers ($t_F \geq 8$ nm) show deviations from a linear dependence of $1/\xi_{\mathrm{FMR}}$ vs. $1/t_F$ that can be understood as due to the effect of an inverse spin Hall voltage resulting from spin pumping or resonant heating [37, 11]. We therefore perform the linear fits only to the four samples with the thinnest F layers, extracting the values shown in Table 2.1. ξ_{DL} and ξ_{FL} are calculated from the y-intercept and slope of the fits, respectively, following the prescription of Eq. (2.11). The FM and AM methods

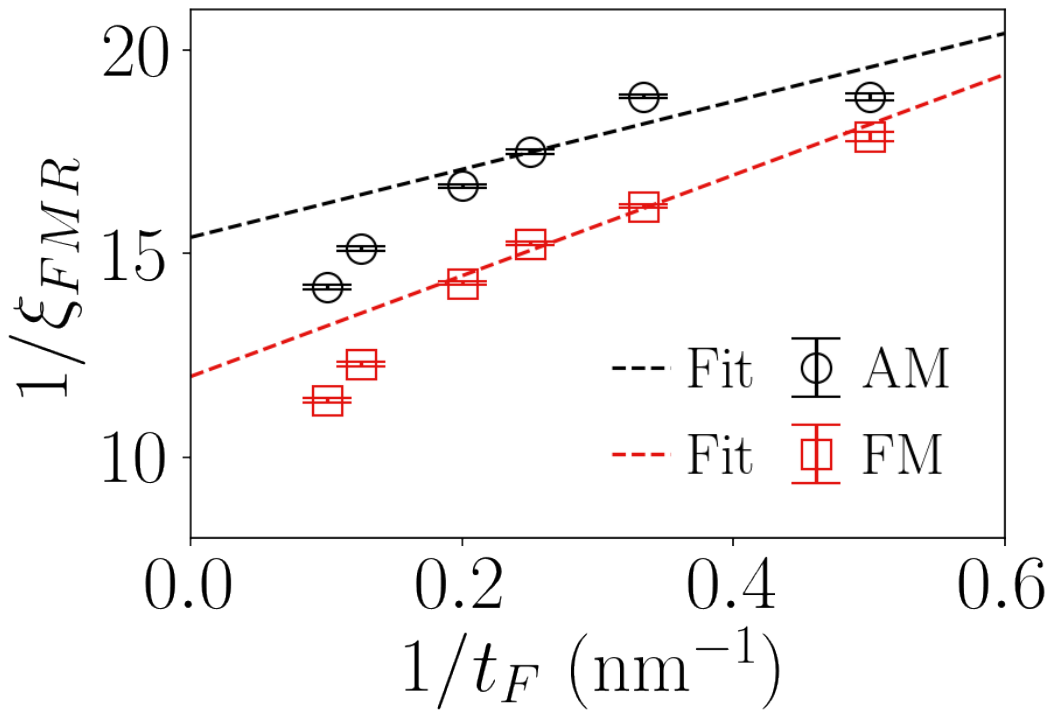

Figure 2.6: Fits to Eq. (2.11) to determine the spin torque efficiencies ξ_{DL} and ξ_{FL} from the lineshape analyses. The values of ξ_{FMR} plotted are calculated according to Eq. (2.10), corresponding to measurements of V_S and V_A done at 20 dBm, 10 GHz, $\phi_0 = 45°$, $f_m = 1.7$ kHz, and $I_{\mathrm{DC}} = 0$. The resonance fits are performed over the same window as the LW measurements: $[B_0 - 15\Delta, B_0 + 15\Delta]$. AM measurements are done with 100% AM-depth and FM measurements with $\delta f = 16$ MHz.

yield values for both ξ_{DL} and ξ_{FL} that differ by considerably more than the estimated statistical uncertainty in the results. The difference in the values of ξ_{DL} is about 30%, while for ξ_{FL} the FM result nearly double that of the AM.

	AM	FM
ξ_{DL}	0.0650(4)	0.0835(7)
ξ_{FL}	0.0050(2)	0.0094(2)

Table 2.1: ξ_{DL} and ξ_{FL} that result from the linear fits shown in Fig. 2.6.

We suggest that the differences between these AM and FM LS results can be explained by the neglect of the residual terms. If we take the values of ξ_{DL} and ξ_{FL} determined by the FM measurements and use them in fitting to the AM data, the result is a residual similar to that shown in Fig. 2.3 that can be fit just as well to a sum of a signal due to an oscillating value of M_{eff} plus a large-Δ resonance as shown in Fig. 2.7.

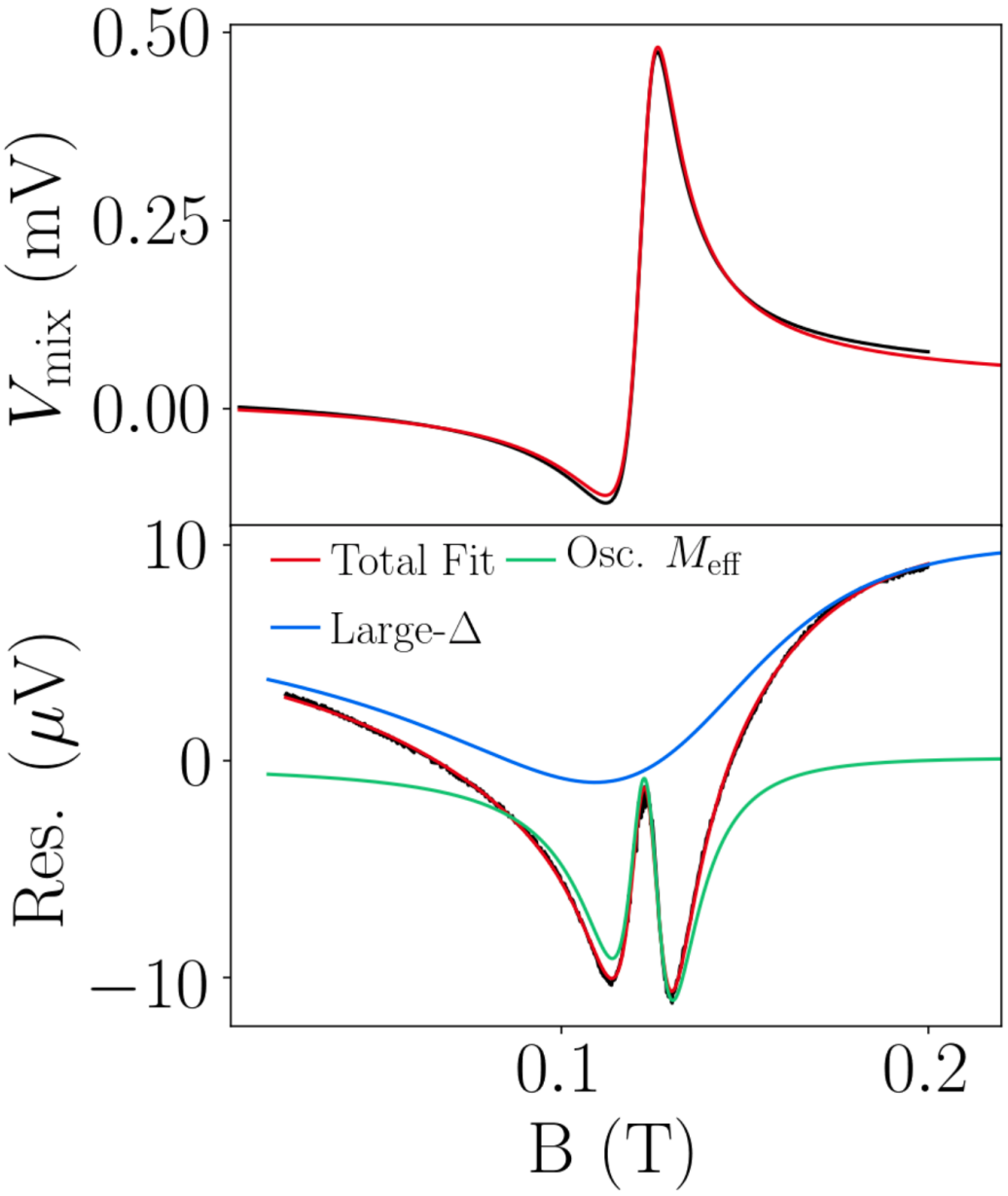

Figure 2.7: Fits to the AM measured resonance by forcing the ξ_{DL} and ξ_{FL} values of the AM measurement to be the same as those in the FM measurement. The fit quality is not severely reduced and the fit difference is absorbed into the fit residuals.

Fits to the AM data that include both the primary resonance and the two artifact contributions therefore possess near-degenerate fitting parameters, that can make determination of the spin-torque efficiencies imprecise.

2.3.2 Results of Linewidth Analyses

The LW measurement proceeds identically to the LS measurement, but for the application of a DC current parallel to the microwave current. A full resonance lineshape (e.g., Fig. 2.2) is collected for DC currents ranging from -4 mA to 4 mA and the resonances are fit to Eq. (2.6) for the AM measurements or Eq. (2.9) for the FM measurements to extract the linewidth, Δ (ignoring residuals for now). We find that the value of Δ that we get from the fits for the AM measurement depends strongly on whether and to what extent we include the tails of the resonance. Figure 2.8 shows the current dependence of linewidths for a Pt(6 nm)/Py(5 nm) sample extracted from fits over the field range $[B_0 - 15\Delta, B_0 + 15\Delta]$ (with Δ adjusted for each sample corresponding to the linewidth of the primary resonance at zero DC current). This is the largest fit window that is possible while consistently excluding artifacts associated with deviations from magnetic saturation at low field for all samples. The zero-current value of Δ is subtracted from each of the plots in Fig. 2.8 to highlight the difference in the slopes of the best-fit lines. We apply Eq. (2.12) to the slopes of the best-fit lines and get the results for ξ_{DL} shown in Table 2.2.

ξ_{DL}	AM	FM
45°	0.234(5)	0.082(2)
225°	0.237(5)	0.087(2)

Table 2.2: Table of ξ_{DL} values for a Pt(6 nm)/Py(5 nm) sample using the LW method. The values are extracted from the slopes of the best fit lines in Fig. 2.8 and Eq. (2.12).

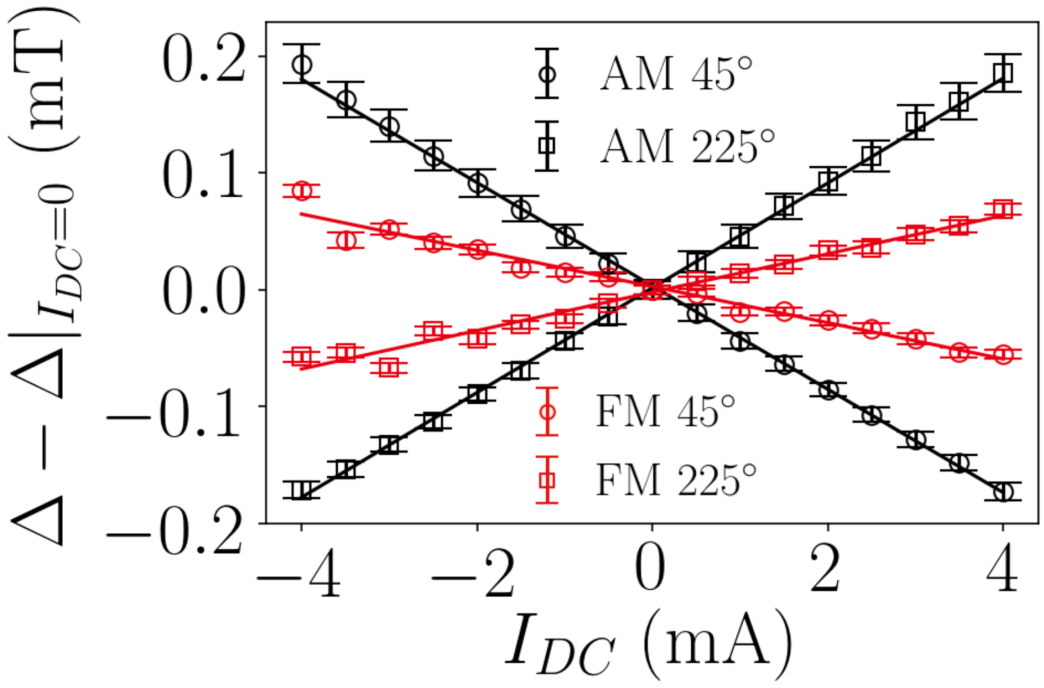

Figure 2.8: Dependence of the resonance linewidth (Δ) on I_{DC} for a Pt(6 nm)/Py(5 nm) sample based on fits to Eq. (2.6) for the AM measurements and Eq. (2.9) for the FM measurements, for data collected at 20 dBm, 10 GHz, $\phi_0 = 45°/225°$, $f_m = 1.7$ kHz. Linewidths are extracted using a fit window $[B_0 - 15\Delta,\ B_0 + 15\Delta]$. The zero-DC-current linewidths (5.27 mT for AM and 5.24 mT for FM) are subtracted. The solid lines are least-squares best fit lines to the data.

For this sample, we see that the FM LW measurements agree with the FM LS result within the experimental uncertainties (Table 2.2), while the AM LW measurements differ by more than a factor of 3 from both the FM results and the AM LS measurements. Figure 2.9 compares the results of similar LW analyses for all of the Pt(6 nm)/Py(t_{FM}) samples with different magnetic-layer thicknesses using the same fit window $[B_0 - 15\Delta,\ B_0 + 15\Delta]$. The AM LW measurements (black points) give far larger values for ξ_{DL} compared to any of the other techniques. The FM LW measurements are reasonably consistent with the FM LS value in the range t_F = 4 - 10 nm (with small deviations for t_F = 10 nm possibly due to the neglect of an inverse spin Hall voltage generated by spin pumping or a spin Seebeck effect), but the FM LW measurements also differ increasingly from the the LS results for Py thicknesses below 4 nm.

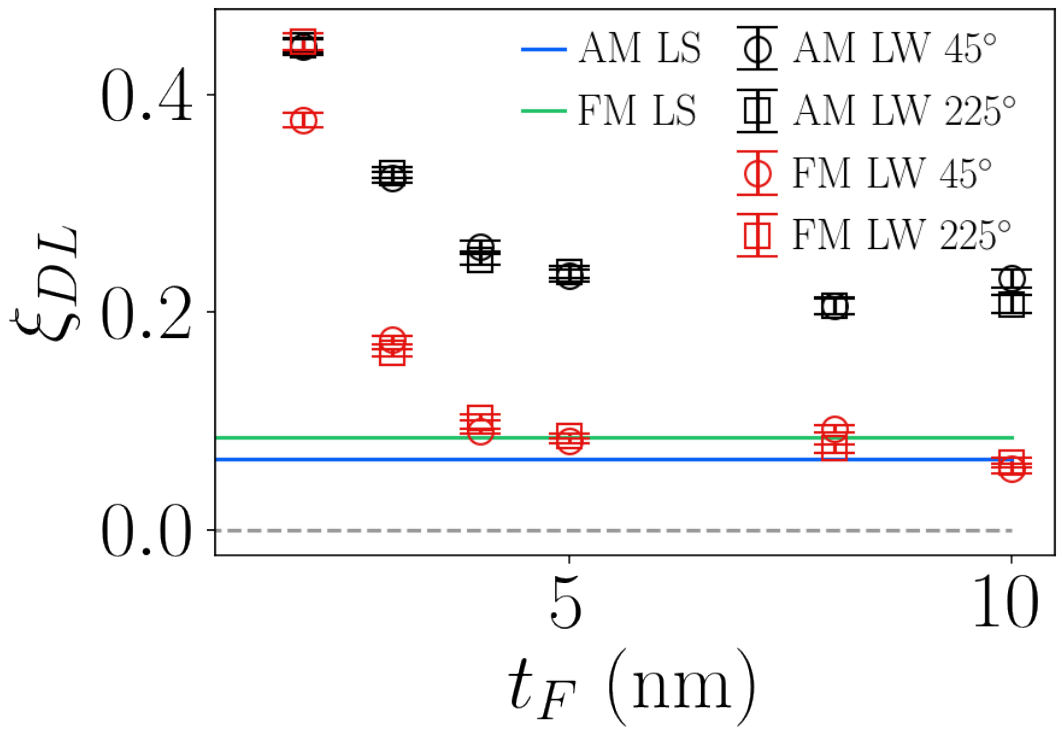

Figure 2.9: Extracted values of the damping-like spin-torque efficiency ξ_{DL} for samples with different ferromagnet layer thicknesses. Symbols show the results of the AM and FM linewidth analyses using fits over the field range $[B_0 - 15\Delta,\ B_0 + 15\Delta]$. The green and blue lines are the results of the lineshape analyses for the thickness series shown in Fig. 2.6.

In Fig. 2.10 we show the results of the same LW analysis using different

sizes for the window of magnetic field included in the fits. The panels on the left show the values of ξ_{DL} extracted for window sizes from $[B_0 - 15\Delta, B_0 + 15\Delta]$ to $[B_0 - 2\Delta, B_0 + 2\Delta]$. For both the AM and FM data sets, the extracted values of ξ_{DL} decrease with decreasing window size. We interpret this dependence as a clear indication that the LW analysis can be disrupted by the long tails of the residual terms that are not included as part of the standard linewidth analysis. For a fixed value of fit-window size, the disruption is most severe for magnetic layers thinner than 4 nm because the linewidth of the primary resonance increases for thin layers, making the primary resonance more difficult to disentangle from the large-linewidth residual signal.

The right panels of Fig. 2.10 show zoom-ins of the same LW results to better visualize the extrapolation of the measurements to zero linewidth. We find that this extrapolation brings the results of both the AM LW and FM LW analyses into reasonable quantitative agreement with the lineshape results.

We emphasize that the sensitive dependence on fit-window size shown by Fig. 2.10 occurs despite the fact that the individual fits look quite good by eye for any choice of window size. The LW analyses are based on quite subtle changes in the resonance lineshape, e.g. about a 2% change in linewidth over the full range of I_{DC} for the FM measurements shown in Fig. 2.8. Therefore, even small changes in V_{mix} associated with current-dependent residuals can affect the LW analysis – the small tails of the ST-FMR resonances can be substantially affected even if the overall magnitude of the residual signals near the resonance field is small. The large-Δ resonance in particular has a large effect on the LW analyses because its linewidth is strongly current dependent (see Fig. 2.5). This is why the windowed fitting works – as the window size is reduced the strong current dependence associated with the tails of the large-Δ residual signal is excluded.

We have tried fitting the AM resonances to a generalized Eq. 2.6 that includes the models for the residuals directly in the fit, but this is not able to pro-

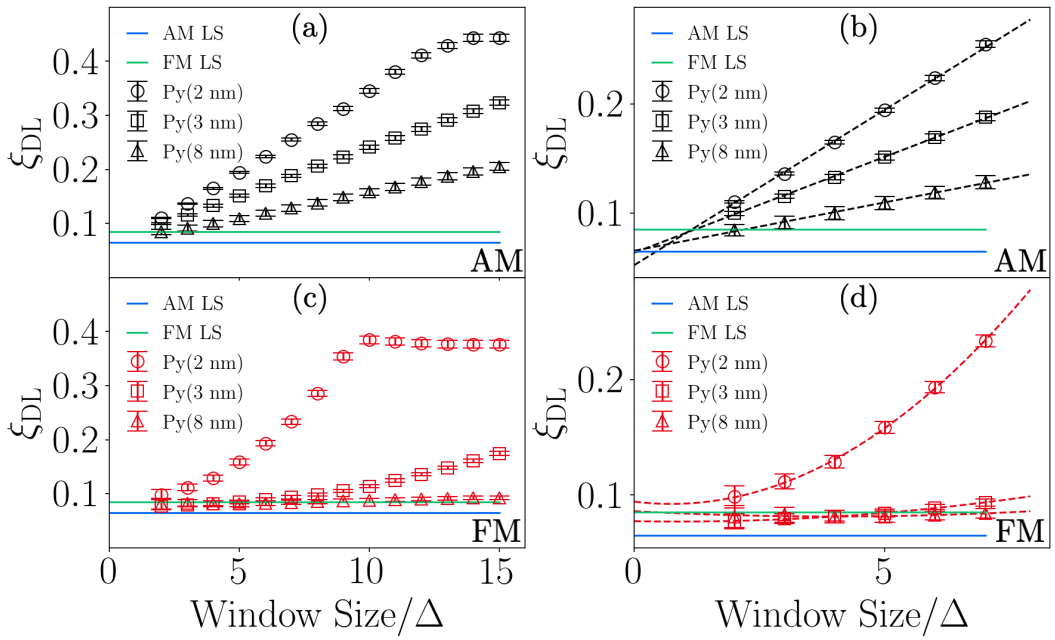

Figure 2.10: The DL-SOT efficiency, ξ_{DL}, vs. the size of the fit window (normalized by the resonance linewidth, Δ). All data in this figure is from the LW analysis method with $\phi_0 = 45°$. **(a)** The full range of fit windows with AM. **(b)** A zoomed view of the AM data with best-fit lines superimposed. ξ_{DL} is linear in the fit window and the y-intercept of the best-fit lines agrees well with the corresponding result of the AM LS analysis. **(c)** The full range of fit windows with FM. **(d)** A zoomed view of the FM data with best-fit second-degree polynomials superimposed. ξ_{DL} is quadratic in the fit window and the y-intercept of the best-fit lines agrees well with the corresponding result of the FM LS analysis.

vide improved quantitative results because of near-degenerate fit parameters. We therefore recommend the procedure depicted in Fig. 2.10 as the simplest approach to improving ST-FMR linewidth analyses – performing the standard ST-FMR fits using a series of different fit-window sizes and then extrapolating to small windows to minimize the influence of the large-linewidth residuals.

2.4 Conclusions

We have identified a cause of inconsistencies between measurements of spin-orbit torque determined via lineshape and linewidth analyses of ST-FMR data – that the standard model for analyzing ST-FMR data does not fully account for all of the magnetic dynamics that can affect the measurements. The standard

analysis leaves residuals that we identify as due to (i) current-induced excitation of a magnetic mode with larger damping than the bulk of the magnetic layer and also (ii) temperature oscillations (≈ 1 °C) associated with the modulation schemes employed for lock-in amplifier measurements. The residuals are not large, with amplitudes of order 1% of the primary resonance, but nevertheless they can affect the current dependence of the resonance tails sufficiently to disrupt an extraction of the anti-damping spin-orbit torque efficiency based on the current dependence of the ST-FMR linewidth. The influence of the large-linewidth residuals can be minimized by performing the standard lineshape analysis using different choices for the range of magnetic field values used to fit the ST-FMR resonances, and then extrapolating to zero fit window. We recommend this procedure for all future uses of the LW analysis. The effect of the residuals can also be reduced by performing ST-FMR using frequency modulation rather than amplitude modulation, but frequency modulation alone does not cure inconsistencies between the lineshape and linewidth results for our thinnest magnetic layers without extrapolation of the fit window to small values.

It remains an interesting open question what is the microscopic origin of the large-linewidth mode that contributes to the residual signal. Based on the scaling of signal amplitudes with the widths and thicknesses of our samples, we identify this mode with the heavy-metal/magnet interface rather than as due to increased damping at the lateral edges of our magnetic layers. It is therefore possible that this mode is due to an interface magnon or magnetic impurities caused by intermixing near the interface. We have also considered whether it might be due to a magnetic proximity layer within the platinum, but amplitude-modulated ST-FMR measurements on a W(3 nm)/Py(5 nm) sample also exhibit a contribution from a large-linewidth resonance as shown in Fig. 2.11. Since magnetic proximity effects should be negligible in W at room temperature, this argues against this mechanism as the dominant contribution

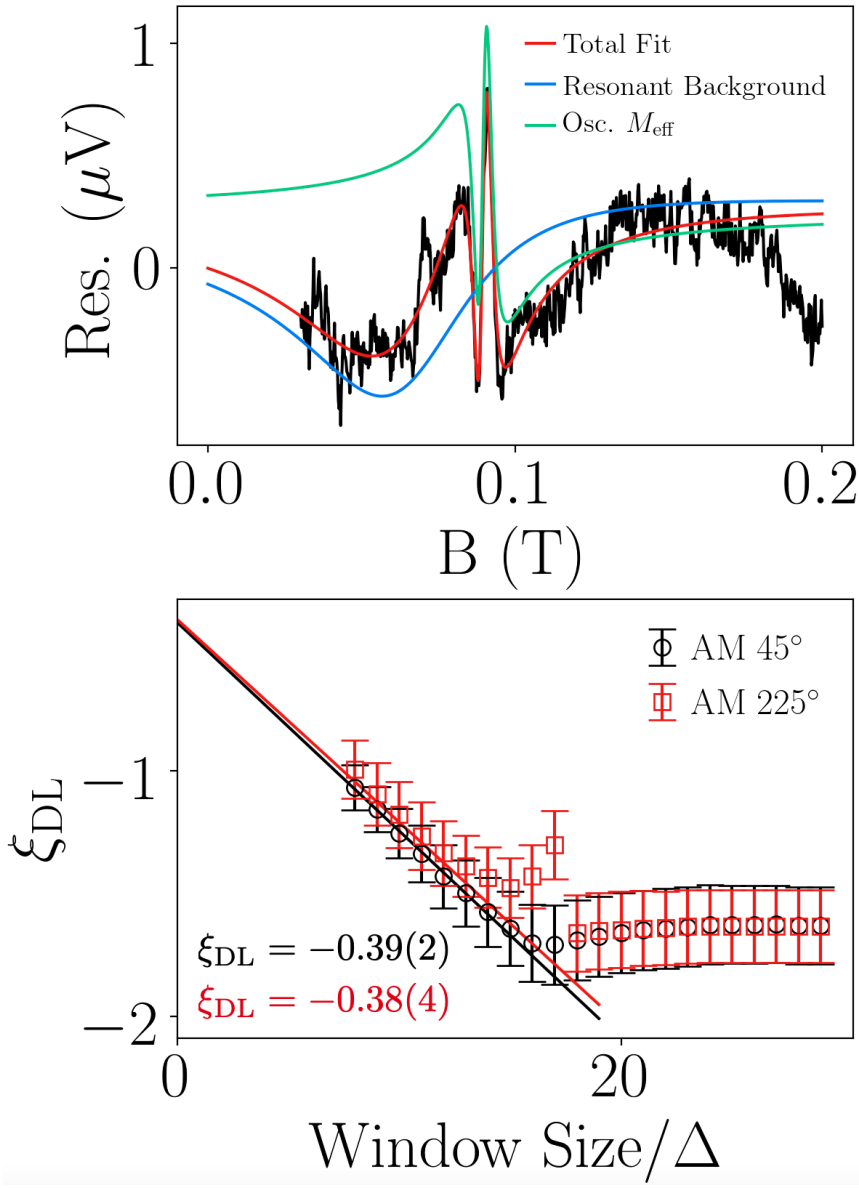

Figure 2.11: Residuals and window-size dependence of a W(3)/Py(5) sample.

in the Pt samples. Future experiments as a function of varying the interface structure or with the insertion of spacer layers might help to reveal the origin of the large-linewidth mode.

Chapter 3

Second-Harmonic Hall, Magneto-optic Kerr Effect (MOKE) Sagnac Interferometry, and the Planar Hall Correction

3.1 Introduction

The ST-FMR techniques desribed in the previous chapters are most easily and most often applied to HM/FM systems with easy-plane magnetic anisotropy. However, for technological applications, FMs with out-of-plane anisotropy (perpendicular magnetic anisotropy, PMA) have been shown to have better retention and stronger TMR effects, so they are often preferred over their easy-plane counterparts. The most common measurement technique used to quantify SOTs perturbatively is second harmonic Hall [33]. The idea is very similar to ST-FMR: an AC current is applied to a device, the magnetization is reoriented causing resistance oscillations, and a voltage is read out through the mixing of resistance and current oscillations. The difference from ST-FMR is that the AC current is now at a much smaller frequency (usually a few kHz), so now the magnetization is perturbed quasistatically and not driven into resonant

precession. The measurement technique begins with an out-of-plane magnetic moment; an AC current is applied and the Hall voltage is measured; meanwhile, an external magnetic field is applied in the plane of the device, which tilts the magnetization partly into the plane. The first harmonic voltage contains information about the magnetic-field-induced tilt and the second harmonic voltage contains information about the small tilts that are caused by SOTs acting on the magnetization. In the Hall measurement geometry, the AHE and PHE are measureable in the first harmonic voltage by tilting the magnetic moment by an external field, so to correctly quantify the SOTs, the second harmonic signal must be analyzed assuming that both the AHE and PHE contribute. This is based on the long-held assumption that a SOT's effect on the magnetization is indistinguishable from that of a magnetic field.

A very common issue with this technique is that it often gives unreasonable (strong disagreement with corroborating measurements) [57] or even unphysical (wrong *sign* of SOT) [58] when the correct analysis is performed. Additionally, it has been seen that if the PHE contribution to the second harmonic signal is ignored, then agreement between the technique and corroborating ones is restored [59]. Ignoring the PHE in this way is tantamount to claiming that SOTs affect the PHE differently than an external magnetic field does. An explanation or convincing verification of this prescription has not yet been offered, and we offer the latter in this chapter.

We design and build a MOKE Sagnac interferometer with remarkable sensitivity that is capable of optically measuring (for the first time) the small, quasistatic reorientations of the magnetic moment that occur during a second harmonic Hall measurement. We built the setup in such a way that the optical and harmonic Hall signals may be measured at the exact same time. This is a simultaneous corroborating measurement of the same magnetic dynamics using two different read out mechanisms, a gold-standard.

We find that when we perform and analyze the results of the optical and elec-

trical measurements on strongly-PMA stacks that the quantified SOTs disagree between the two methods. The disagreement between them is quite significant: about 60% in Pt/Co stacks and up to 1500% in Pd/Co stacks, with the harmonic Hall measurement resulting in an unreasonably large result for Pd/Co. In addition, we find that if we force a weakly-PMA Pt/Co stack to be fully in-plane and perform an in-plane second harmonic Hall measurement [28] that the results agree with the optical measurement on the strongly-PMA stacks. The harmonic Hall results performed on strongly-PMA samples are the outliers. We find that when the PHE contribution to the second harmonic signals is ignored, that agreement is achieved across all of the measurements. This suggests that SOTs and applied magnetic fields express differently through the PHE, but as of yet we have not determined the reason for this and it remains an open (and very interesting) question.

Much of the following is taken and adapter from ref. [60].

3.2 Harmonic Hall Tilting Derivation

In this section, we will derive the transport signals in a way that differs from ref. [33] but arrives at the same answer. We assume a magnetic layer with perpendicular magnetic anisotropy (PMA). The moment is tilted slightly in-plane ($\theta_0 > 0$) by varying the strength of an in-plane external magnetic field, H that is applied in the plane of the sample. During this external-field-induced tilting, an AC current is applied through the device and the first- and second-harmonic voltages are measured.

We begin the derivation by writing the equilibrium magnetic free energy

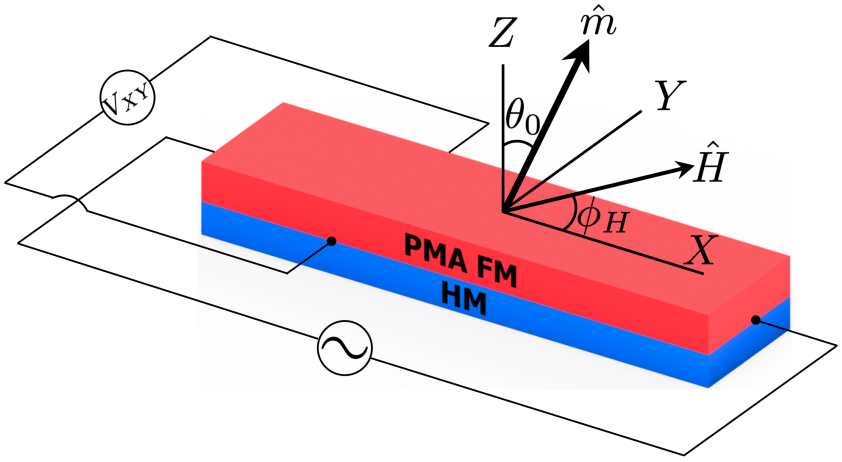

Figure 3.1: The device under consideration for the PMA harmonic Hall measurements. The coordinates match those in the derivation below.

divided by the total magnetic moment in the absence of any applied current

$$\begin{aligned}\frac{F_{\text{eq}}(\theta,\phi)}{M_s} &= -\mu_0 \mathbf{m}\cdot\mathbf{H} - \frac{\mu_0 M_{\text{eff}}}{2}(\mathbf{m}\cdot\hat{Z})^2 \\ &= -\mu_0 H \sin\theta \sin\theta_H \cos(\phi-\phi_H) - \frac{\mu_0}{2}\cos\theta(2H\cos\theta_H + M_{\text{eff}}\cos\theta).\end{aligned} \tag{3.1}$$

Here F_{eq} is the equilibrium free energy, M_s is the saturation magnetization, $\mathbf{m}$ is the vector magnetic moment, $\mathbf{H}$ is the vector external magnetic field, and $\mu_0 M_{\text{eff}} = 2K_\perp/M_s - \mu_0 M_s$ is the effective magnetization. PMA is indicated by a *positive* M_{eff}. The angles in the second line denote the direction of external applied magnetic field when subscripted with an H and refer to the the direction of the magnetic moment when they lack a subscript. Minimization of this free energy yields the equilibrium magnetic orientation θ_0,ϕ_0. As we apply a low frequency AC current the SOTs produced will act as effective fields that reorient the magnetic moment. This is a "slow" process ($\dot{\mathbf{m}} \ll \gamma|H|$) so it may be described as an effective modification of equilibrium free energy (equation 3.1). With the perturbation from a general, current-induced effective magnetic

field, $\Delta\mathbf{H}$ (assumed small compared to H), the free energy becomes

$$\begin{aligned}\frac{F(\theta,\phi)}{M_s} =& \frac{F_{\text{eq}}(\theta,\phi)}{M_s} - \mu_0 \mathbf{m}\cdot\Delta\mathbf{H} \\ \approx& \frac{F_{\text{eq}}(\theta_0,\phi_0)}{M_s} + \frac{1}{2M_s}\frac{\partial^2 F_{\text{eq}}}{\partial\theta^2}\Big|_{\theta_0,\phi_0}(\Delta\theta)^2 \\ &+ \frac{1}{2M_s}\frac{\partial^2 F_{\text{eq}}}{\partial\phi^2}\Big|_{\theta_0,\phi_0}(\Delta\phi)^2 \\ &+ \frac{1}{M_s}\frac{\partial^2 F_{\text{eq}}}{\partial\theta\partial\phi}\Big|_{\theta_0,\phi_0}\Delta\theta\Delta\phi \\ &- \mu_0(\sin\theta\cos\phi\Delta H_X + \sin\theta\sin\phi\Delta H_Y + \cos\theta\Delta H_Z).\end{aligned} \tag{3.2}$$

(The first derivatives of F_{eq} are zero when evaluated at the equilibrium orientation.) We have included the cross second derivative in this expression, but when evaluated it gives zero. The new magnetic orientation in the presence of the current-induced magnetic field can then be calculated as a minimization problem

$$\frac{\partial F}{\partial\theta} = \frac{\partial F}{\partial\phi} = 0. \tag{3.3}$$

We will henceforth assume that $\theta_H = \pi/2$ to match the experimental technique (the external magnetic field is applied in the plane of the device), so that $\sin\theta_0 = H/(M_{\text{eff}})$. We will also assume negligible within-plane anisotropy so that the in-plane projection of the equilibrium magnetic moment is aligned with the external field i.e. $\phi_0 = \phi_H$. The solutions of equation (3.3) to first order in the current-induced field yield

$$\Delta\theta = \frac{\Delta H_Z \sin\theta_0 - \cos\theta_0(\Delta H_X\cos\phi_H + \Delta H_Y\sin\phi_H)}{M_{\text{eff}}\cos 2\theta_0 + H\sin\theta_0} \tag{3.4}$$

$$\Delta\phi = \frac{\Delta H_X\sin\phi_H - \Delta H_Y\cos\phi_H}{H}. \tag{3.5}$$

To get from the above equations to the full expected transport signal (equations (3) and (4) in the main text) we begin with the the expression for the

Hall resistance

$$R_{XY} = R_{\mathrm{PHE}} m_X m_Y + R_{\mathrm{AHE}} m_Z \tag{3.6}$$

$$= \frac{R_{\mathrm{PHE}}}{2} \sin^2\theta \sin 2\phi + R_{\mathrm{AHE}} \cos\theta. \tag{3.7}$$

(Note that our definition of R_{AHE} is equal to $\Delta R_A/2$ as defined in ref. [33].)

We let θ and ϕ each consist of an equilibrium contribution due to the external magnetic field and a time-dependent contribution due to the AC-current-induced spin-orbit fields: $\theta \to \theta_0 + \Delta\theta$ and $\phi \to \phi_0 + \Delta\phi$ with $\Delta\theta, \Delta\phi \ll 1$ and then Taylor expand

$$R_{XY} \approx \frac{R_{\mathrm{PHE}}}{2} \left(\sin^2\theta_0 + \Delta\theta \sin 2\theta_0\right) \left(\sin 2\phi_0 + 2\Delta\phi \cos 2\phi_0\right) + R_{\mathrm{AHE}} \left(\cos\theta_0 - \Delta\theta \sin\theta_0\right). \tag{3.8}$$

We disregard the second-order terms (e.g. $\propto \Delta\theta\Delta\phi$)

$$\begin{aligned} R_{XY} \approx & R_{\mathrm{PHE}} \left(\frac{1}{2} \sin^2\theta_0 \sin 2\phi_0 + \Delta\phi \sin^2\theta_0 \cos 2\phi_0 + \frac{1}{2}\Delta\theta \sin 2\theta_0 \sin 2\phi_0\right) \\ & + R_{\mathrm{AHE}} \left(\cos\theta_0 - \Delta\theta \sin\theta_0\right). \end{aligned} \tag{3.9}$$

Here we use that $\sin\theta_0 = H/M_{\mathrm{eff}}$ and $\phi_0 = \phi_H$, we substitute in the expressions for $\Delta\theta$ and $\Delta\phi$ that were derived previously, and we separate the first and second harmonics. For weak applied fields $H \ll M_{\mathrm{eff}}$ we get

$$V_{XY}^{\omega} = \left[\pm R_{\mathrm{AHE}} \left(1 - \frac{H^2}{2M_{\mathrm{eff}}^2}\right) + R_{\mathrm{PHE}} \frac{H^2}{2M_{\mathrm{eff}}^2} \sin 2\phi_H\right] \Delta I \tag{3.10}$$

$$\begin{aligned} V_{XY}^{2\omega} = & \frac{1}{2} \frac{H}{M_{\mathrm{eff}}^2} \Delta w e \left[\left(\pm R_{\mathrm{AHE}} - R_{\mathrm{PHE}} \sin 2\phi_H\right) \left(\Delta H_X \cos\phi_H + \Delta H_Y \sin\phi_H\right)\right. \\ & \left. + R_{\mathrm{PHE}} \cos 2\phi_H \left(\Delta H_X \sin\phi_H - \Delta H_Y \cos\phi_H\right)\right]. \end{aligned} \tag{3.11}$$

The latter expression can be simplified to

$$V_{XY}^{2\omega} = \frac{1}{2}\frac{H}{M_{\text{eff}}^2}\Delta we\left[\pm R_{\text{AHE}}\left(\Delta H_X\cos\phi_H + \Delta H_Y\sin\phi_H\right)\right.$$
$$\left. - R_{\text{PHE}}\left(\Delta H_X\sin\phi_H + \Delta H_Y\cos\phi_H\right)\right]. \tag{3.12}$$

These previous equations are valid for arbitrary angles ϕ_H for the orientation of the in-plane applied magnetic field. When evaluated for $\phi_H = 0$ and $\pi/2$, they are equivalent to the final expressions in ref. [33] taking into account the difference in notation: $R_{\text{AHE}} = \Delta R_A/2$.

3.2.1 Calculating the Torques: Conventional Means

Following the lead of [33], we calculate the effective fields (and therefore, ξ_{DL} and ξ_{FL} in the main text) with the following expressions

$$\Delta H_{X(Y)}^{\text{no PHC}} = -2\Delta B_{X(Y)} = -2\times\frac{dV_{XY}^{2\omega}}{dH_{X(Y)}}\left(\frac{d^2V_{XY}^{\omega}}{dH_{X(Y)}^2}\right)^{-1}. \tag{3.13}$$

We also account for the PHC using the procedure in ref. [33]

$$\Delta H_{X(Y)}^{\text{PHC}} = -2\frac{\Delta B_{X(Y)} \pm \epsilon\Delta B_{Y(X)}}{1-\epsilon^2} \tag{3.14}$$

where $\epsilon = R_{\text{PHE}}/R_{\text{AHE}}$.

3.2.2 Calculating the Torques: Overconstrained linear system

We may also calculate the torques in more balanced way that reduces the errorbar of the result. Eqs. (14) and (15) may be recast into an overconstrained

linear system

$$CH = S \implies \tag{3.15}$$

$$\begin{pmatrix} -C_{\mathrm{AHE}} & C_{\mathrm{PHE}} \\ -C_{\mathrm{AHE}} & C_{\mathrm{PHE}} \\ C_{\mathrm{PHE}} & -C_{\mathrm{AHE}} \\ -C_{\mathrm{PHE}} & C_{\mathrm{AHE}} \end{pmatrix} \begin{pmatrix} \Delta H_X \\ \Delta H_Y \end{pmatrix} = \begin{pmatrix} S_X^+ \\ S_X^- \\ S_Y^+ \\ S_Y^- \end{pmatrix} \tag{3.16}$$

where $S^{\pm}_{X(Y)} = dV^{2\omega}/dH_{X(Y)}\big|_{\pm M}$ and $C_{\mathrm{AHE(PHE)}} = -\frac{\Delta w e R_{\mathrm{AHE(PHE)}}}{2M_{\mathrm{eff}}^2}$. We can solve this system for H by taking the psuedoinverse $H = C^+S$ where $C^+ = (C^TC)^{-1}C^T$.

3.3 Introduction to the Sagnac Interferometer

Conventional methods of measuring the magneto-optic Kerr effect (MOKE) lack the sensitivity to measure small-angle magnetic tilting in PMA heterostructures in a way that is analogous to the standard PMA harmonic Hall measurement [33]. Indeed, small-angle magnetization tilts in the PMA harmonic Hall measurement account for a few mRad of magnetization oscillation, and typical optical couplings to magnetic signals are again a few parts in a thousand, so one would have to measure a signal of a few μRad. A more sensitive measurement apparatus is needed. The Sagnac MOKE interferometer boasts a very high sensitivy as it was first developed to (successfully) measure spins in superconductors [61, 62]. The Sagnac MOKE interferometer works by translating the effect of MOKE into a phase difference between two beams that travel the same physical path back and forth as shown in Fig. 3.2.

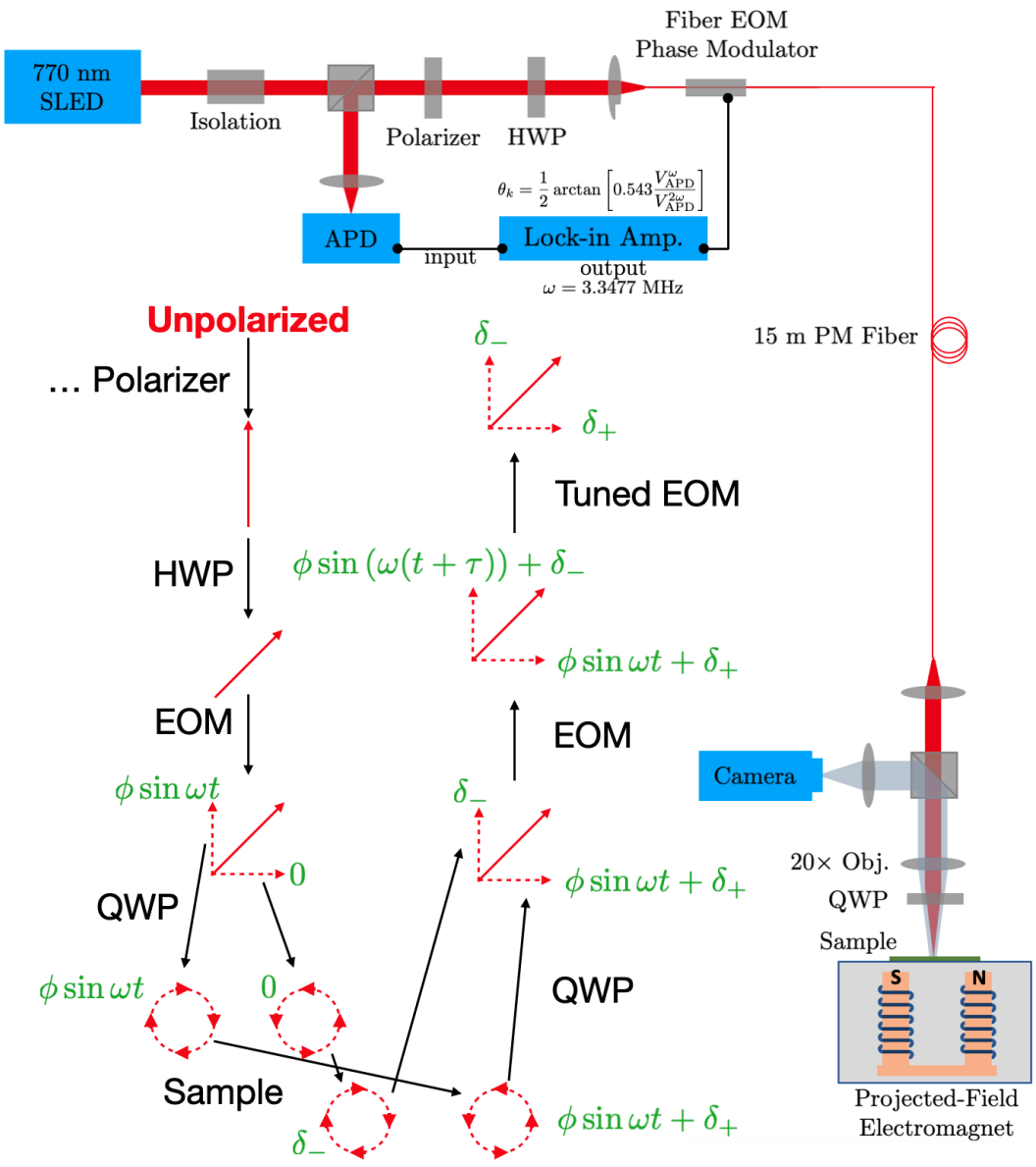

Figure 3.2: A diagram of the beamline of the Sagnac MOKE interferometer along with a cartoon of the beam polarization optics as the beam follows the Sagnac path. In the cartoon the black arrows and labels indicate the beams interaction with an optical element; everything in red indicates the state of the beam with arrows indicating linear polarization and circles indicating circular polarization; the green labels indicate the phase of the component beam to which the green label is closest.

This Sagnac MOKE interferometer is modeled after those in refs. [61, 63], mixing elements from each of these two works. The beamline begins with a 770 nm superluminescent diode (SLED). The beam goes through a pair of Faraday isolators that provide > 65 dB of backward isolation and prevent back-reflections into the diode that would cause intensity fluctuations and other source instabilities. Next, the beam goes through a beam splitter, polarizer, and half-wave plate (HWP) that prepare the beam polarization to be 45° with respect to the slow axis of a polarization-maintaining (PM) fiber into which it is focused. The beam will henceforth be discussed as an equal linear combination of two separate beams of linearly-polarized light: one polarized along the slow axis and one polarized along fast axis of the PM fiber. A fiber electro-optic phase modulator (EOM) applies time-dependent phase to the beam traveling along the slow axis: $\phi_m \sin \omega t$. The beam then travels along 15 meters of PM fiber, whereupon it is collimated and focused by a long-working-distance objective through a quarter-wave plate (QWP) and onto a sample. The QWP is oriented such that one beam is converted to left-circularly-polarized light and the other is converted to right-circularly-polarized light. The beams then reflect off of a sample, exchanging the handedness of the beams and, if the sample is magnetic, imparting both the effects of circular dichroism and circular birefringence (the $\delta_\pm$); the latter is equivalent to a Kerr rotation of linearly-polarized light and the two beams are now exchanged. Upon reflection, the two beams (now exchanged) backpropagate and the previously-unphased beam is now phased by $\phi_m \sin(\omega(t+\tau))$ where τ is the time it takes for the light to make the round trip back to the EOM. The driving frequency ω is chosen such that the EOM phases are nearly equal between the two beams ($\omega = \pi/\tau$ [61]) and so the two beams are nearly coherent again ($\delta_\pm$ is small) and interfere to produce homodyne intensity oscillations at the EOM frequency. The backpropagating beams are then routed by the beam splitter and focused into a broadband avalanche photodetector (APD). The APD's output voltage is measured by a

lock-in amplifier that references the driving frequency of the EOM, ω. The frequency ω in this system turns out to be $[2\pi(3.3477\text{ MHz})]$. To maximize the Kerr rotation signal, the phase modulation depth ϕ_m is set by tuning the magnitude of AC voltage applied to the EOM to be $\phi_m = 0.92$ [63].

3.4 Some Details about the Sagnac's Construction

The work by Fried et al., Rev. Sci. Instrum. **85**, 103707 (2014) [63] is a great reference. This paper served as the most helpful resource when building and debugging our interferometer. The entire setup, including all of the optics, sample stage, and magnet are housed on a floating optic table and enclosed in a rigid polycarbonate box affixed with sound-proof foam to block air currents and external vibrations.

For the source, we use a 770 nm SLED, which has a broad ($\approx$ 15 nm) linewidth. In our original design we used a ultra-narrow-linewidth 780 nm diode, but we found that the broad-linewidth source reduced our noise by about a factor of two; this is because the small-linewidth source has a long beam coherence length. Therefore, the forward-going beam remained coherent with the reflected beam upon cycling through the apparatus, which gave them the opportunity to interfere and produce spurious interference signals not related to the Kerr rotation. The diode and most of its pigtailed fiber are stored inside a closed styrofoam box within the polycarbonate box to further prevent temperature fluctuations and air currents.

We use two Faraday isolators that provide $>$ 65 dB of isolation to protect the diode from backreflections. The EOSpace fiber electro-optic phase modulator (EOM) is driven by a 50-MHz-bandwidth Zurich Instruments HF2LI lock-in amplifier and all of the signals (transport and optics) are detected on the same lock-in using its multiple demodulators. Our EOM is permanently pigtailed

with a 5 m fiber and we append a 10 m fiber to it for a total length of 15 m. Both the EOM and the fiber are stored inside a closed styrofoam box (not the same box as the diode) within the polycarbonate box.

Upon exiting the fiber, the beam is collimated by a screw-on FC/APC lens adapter to a beam diameter of about 8 mm. We choose such a large beam diameter to maximize the filling of the back aperture of the objective lens and reduce our beam spot size on the sample. The beamsplitter after the collimating lens is retractable and it is illuminated with white light and inserted only to align the desired sample properly under the beam. The beam does not go through this beamsplitter during measurement. For the objective we choose to use a 20× near-IR ultra-long-working-distance objective lens to minimize the spot size, maximize the numerical aperture and field-of-view, and leave enough room for probes to make contact to the sample. The quarter-wave plate (QWP) is placed *after* the lens so that light is still linearly polarized while going through the lens. Most lenses have non-negligible Verdet constants so this is very important for reducing the spurious Faraday rotation incurred by the beam while it traverses the lens.

Our beam spot size on the sample is approximately 6 μm and our power incident on the device is < 70 μW. We find that optical powers exceeding a few hundred μW can begin to show local heating effects on the sample as indicated, e.g., as a change in the magnetic coercivity. To accommodate such a low-power beam, we detect the signal with a 50-MHz-bandwidth avalanche photodiode (APD) because it maintains a very low noise equivalent power (NEP) while sacrificing its saturation power, which we remain safely below.

3.5 Images and Tour of the Actual Apparatus

In Fig. 3.3, we show an image of the sample area of the Sagnac apparatus.

1. Camera for imaging the device

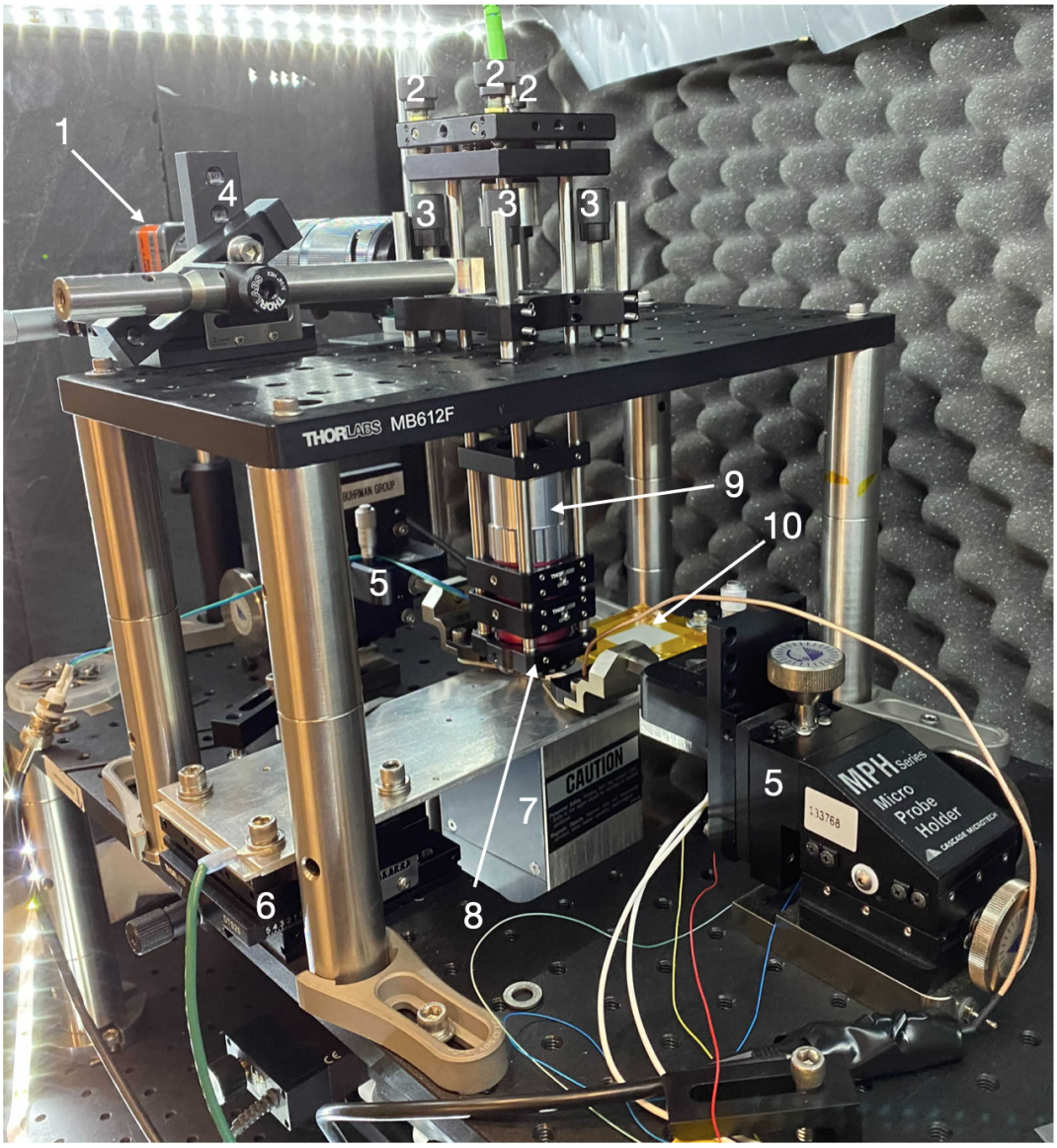

Figure 3.3: Image of the sample area of the Sagnac apparatus.

2. Tilt knobs for the fiber collimator. These knobs should not be touched unless the beam direction is seriously messed up.

3. Focus knobs that adjust the lens position relative to the sample stage. This is a really awesome design for this heavy lens. We really only have to have two out of the four knobs in contact with the Thorlabs MB612F table. Focusing should be done for each sample/device and the focusing strategy is this: unscrew the knobs a bit, push down on the X-shaped cage holder under the number 3's to bring the lens close to the sample, screw two of the knobs in simultaneously while looking at the Zurich lock-in

readout on the computer, turn the knobs until the demodulator tracking the 2ω (ω is the EOM frequency) is maximized, stop. The retractable beamsplitter can change the focus a little, so make sure it is *out* before settling on a final focus.

4. Mount for the retractable beamsplitter. Push it in by hand and use a 1-inch optics post to hold it there when imaging a device on the camera. Take the beamsplitter out when focusing and doing measurements.

5. Probe holders. The probes just barely fit under the QWP (8), so be very careful when raising them.

6. X-Y motion stages for fine sample translation. These are connected to the metal diving-board, which is where the sample sits. Do rough positioning by hand when the motion stages are around the center of their travel.

7. Projected-field electromagnet.

8. Quarter-wave plate (QWP). This mount can be rotated to change the orientation of the QWP, but we should not have to do this unless it gets messed up. The relative rotation of QWP should be matched to the principal axes of the fiber at the top of the cage so that the QWP converts the linerly polarized light into circularly polarized light.

9. 20× ultra-long working distance, near-infrared objective lens.

10. Resistive heater connected to a LakeShore temperature controller. The temperature of the metal diving board actually makes a difference because the focus depth of the lens is small and thermal expansion/contraction of the metal stage can affect focus. The temperature is able to be held constant very well when the polycarbonate box is closed.

In Fig. 3.4, we show the optical components of the Sagnac apparatus with labels for each component.

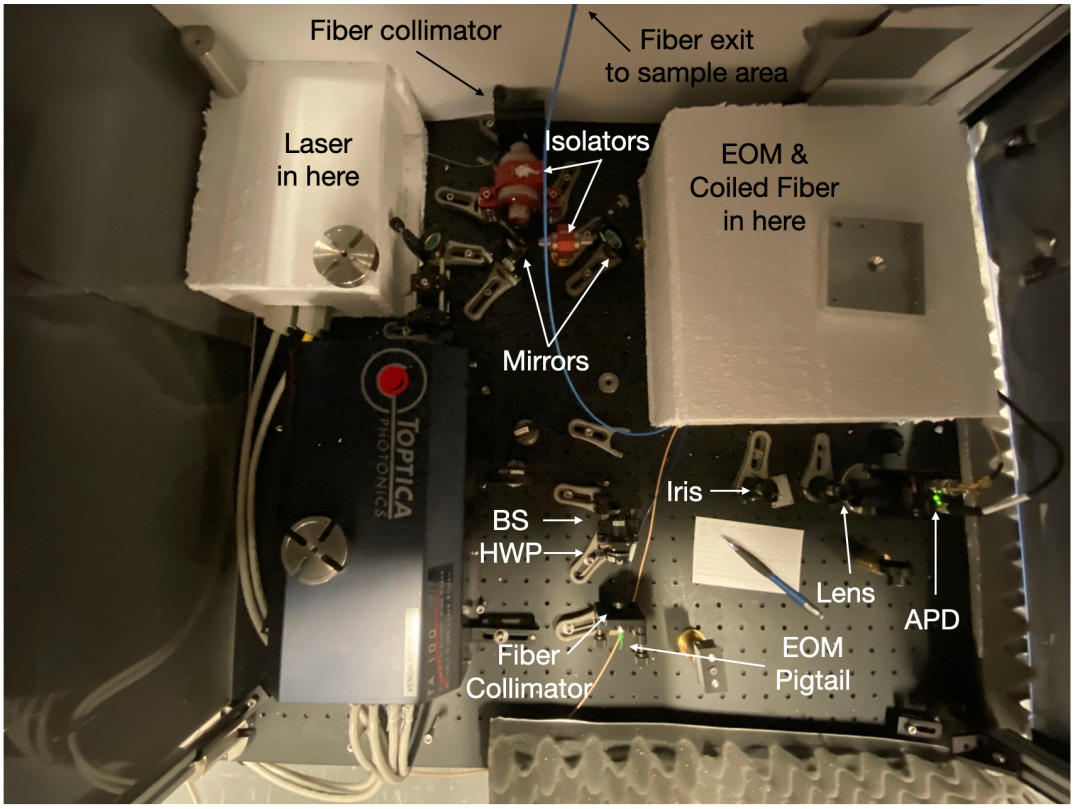

Figure 3.4: Image of the optics of the Sagnac apparatus with labels overlayed.

In Fig. 3.5, we show the optical components of the Sagnac apparatus with the beam path drawn on.

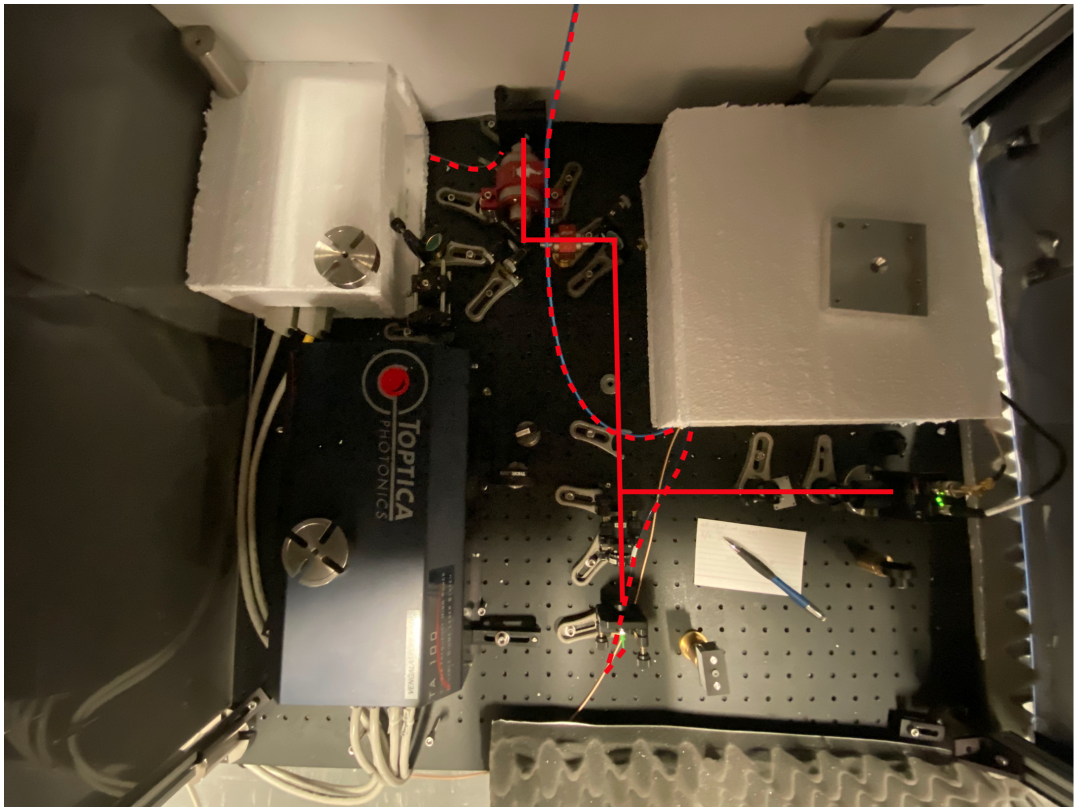

Figure 3.5: Image of the optics of the Sagnac apparatus with the beam overlayed. Solid lines mean the beam is in free space, while dashed lines indiciate the beam is in fiber.

3.6 Polarization-Maintaining Fiber

Polarization-maintaining (PM) fiber is actually a misnomer. PM fiber does not maintain the polarization of beams that enter it, except under very specific circumstances. Ordinary fiber does not maintain the polarization of input light at all because fiber has strong birefringence and that birefringence can change if the fiber is bent, heated etc. PM fiber solves this problem to some degree by making a fiber that has two unique axes with vastly different degrees of birefringence. When linearly polarized light is sent along one of these axes, the phase of that light changes dramatically so as to be incoherent with any other modes of polarization that would come from the intrinsic, inexorable birefringence of the fiber. The PM fiber we use is usually of the "Panda" variety as shown in Fig. 3.6. In this sort of fiber there are the unique fast and

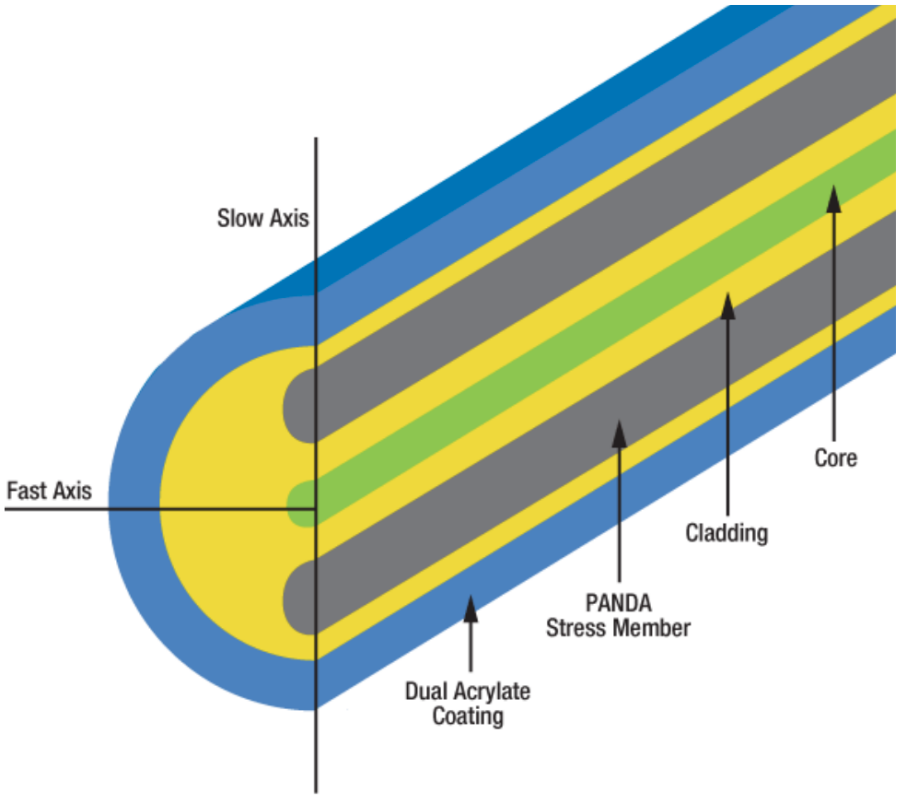

Figure 3.6: Panda PM fiber. Image taken from ThorLabs.

slow axes. Linearly-polarized light will maintain its polarization if it is sent in polarized along one of these axes.

3.6.1 Aligning it

We need to send linearly polarized light into these axes in a way that maintains the polarization for our Sagnac interferometer. To do this, we have to orient the HWP and QWP in a way that matches with the axes of the PM fiber that they couple light to. In particular, the HWP must be aligned such that the light that enters the PM fiber is linearly polarized at 45° with respect to the fast/slow axes, and the QWP must be aligned such that the two independent beams of linearly polarized light that exit the PM fiber are perfectly converted to LCP/RCP light. The problem is that there is no easy way to know how the fast and slow axes are oriented for a given PM fiber. On all of the ThorLabs fiber patch cables we use, the connector key notch is aligned with the slow axis, but we need more precision than that. It turns out that if we just carry out the math below of the Sagnac signal assuming misalignments of the HWP and QWP, we get some factors that diminish the measured 2ω (ω is the EOM drive frequency) signal by the angles of misalignment. The diminishment is actually exactly what one would expect from the symmetry of the optical element: the HWP diminishes the 2ω signal by $\cos^2\phi_{\text{mis}}$ and the QWP diminishes the 2ω signal by $\cos^4\phi_{\text{mis}}$ where ϕ_{mis} is the angle of misalignment. This means that rather than physically trying to determine and orient the fast/slow axes of the PM fiber, we can just set up the whole apparatus and turn the HWP and QWP to maximize the 2ω signal in the lock-in amplifier! This is the procedure that we should use if the HWP, QWP or PM fiber collimators are rotated in any way.

3.6.2 Getting Light Into it

Getting light to go from fiber to fiber is easy, just use a premade fiber-fiber coupler. Getting light to go from free space to fiber is hard. The fiber core (green part of Fig. 3.6) is a few μm in diameter. To get light to go into the fiber, we have to focus free space light into the core of the fiber and do it so that the light goes straight in and is not reflected very much. Thankfully, there are screw-on lenses called "fiber collimators" with carefully-designed focal lengths to make life a little easier. To choose one with the proper focal length, we use the following equation:

$$f = \frac{\pi D_{\mathrm{MF}} w}{4\lambda} \tag{3.17}$$

where D_{MF} is the "mode field diameter" of the fiber (we can find this on the fiber spec sheet, for our 780 nm fibers it is 5.3 $\pm$ 1 μm), w is the diameter of the free space beam that we want to get into the fiber, and λ is the beam's wavelength. Actually getting the light into the fiber is difficult to explain. We ourselves learned how by using this YouTube video (https://www.youtube.com/watch?v=kQvhbJbDG0M&ab_channel=ManojPeiris for paper readers) that we used to learn how to get light into the fiber. Hopefully it still exists. If not, I will describe the procedure poorly below:

1. Get your free-space laser that you intend on shining into the fiber and also get a separate fiber-coupled laser.

2. Screw on the proper fiber collimator onto one end of your fiber and put the fiber collimator in a holder on a post secured to an optical table. Adjust the height to be roughly the height of your free-space beam.

3. Screw the other end of the fiber into the fiber-coupled laser. Light should come out of the fiber collimator now because the fiber-coupled laser is good at shining light into the entrance of the fiber.

4. Get two mirrors onto posts and adjust their height so that their center is roughly the same height as the fiber collimator lens. Don't secure them yet.

5. Place the two mirrors such that you roughly get the free space laser to bounce into the fiber collimator lens. Secure them a bit.

6. Use some paper somewhere in between the mirror and the fiber collimator to find both beams (one from the free space, one exiting the fiber that comes from the fiber-coupled laser).

7. Adjust the mirrors such that these two beams overlap as best as you can. Secure the mirrors when you are done.

8. Unscrew the fiber end connected to the fiber-coupled laser and point that end into a sensitive optical power meter. You should have some optical power coming through the fiber at this point that is due to the free space laser making into the fiber, but unless you're very lucky, it will be small.

9. Make small adjustments to the mirror knobs to maximize the power reading on the power meter.

The video did something called "walking the beam," which is essentially a systematic detuning and retuning of the optical power to its maximum, but we found this doesn't usually improve things very much.

3.7 Derivation of the Sagnac Signal

Now that we understand how the Sagnac apparatus ought to work and we know how to set it up, we can move forward and find what we expect the resulting signals to actually be.

3.7.1 Measurement of the Kerr rotation angle θ_k in the absence of applied current

We will use the language of Jones matrices to derive the Sagnac MOKE signal following the beam path and cartoon laid out in Fig. 3.2. First, we define some general Jones matrices:

$$\mathrm{P}(\theta) = \begin{pmatrix} \cos^2\theta & \sin\theta\cos\theta \\ \sin\theta\cos\theta & \sin^2\theta \end{pmatrix} \tag{3.18}$$

$$\mathrm{WP}(\theta,\phi) = \begin{pmatrix} \cos\frac{\phi}{2} + i\sin\frac{\phi}{2}\cos 2\theta & i\sin\frac{\phi}{2}\sin 2\theta \\ i\sin\frac{\phi}{2}\sin 2\theta & \cos\frac{\phi}{2} - i\sin\frac{\phi}{2}\cos 2\theta \end{pmatrix} \tag{3.19}$$

$$\mathrm{EOM}(t) = \begin{pmatrix} e^{i\phi_\parallel \sin\omega t} & 0 \\ 0 & e^{i\phi_\perp \sin\omega t} \end{pmatrix} \tag{3.20}$$

$$\mathrm{S} = \frac{1}{2}\begin{pmatrix} \frac{e^{-i\delta_+}}{r_+} + \frac{e^{-i\delta_-}}{r_-} & i\left(\frac{e^{-i\delta_+}}{r_+} - \frac{e^{-i\delta_-}}{r_-}\right) \\ -i\left(\frac{e^{-i\delta_+}}{r_+} - \frac{e^{-i\delta_-}}{r_-}\right) & \frac{e^{-i\delta_+}}{r_+} + \frac{e^{-i\delta_-}}{r_-} \end{pmatrix}. \tag{3.21}$$

Here, our Jones vectors are in the basis of the laboratory: P(θ) is a polarizer oriented at an angle θ. WP(θ,ϕ) is a ϕ-wave plate oriented at an angle θ. EOM is the electro-optical phase modulator that applies a voltage-dependent phase ($\phi_\perp$ or $\phi_\parallel$ depending on whether the polarization of the incoming beam is along or perpendicular-to the optical axis of the EOM crystal) at a frequency of ω. In the main text we say that the EOM only applies the phase to the beam traveling along the slow axis of the fiber; this is how the EOMs are designed, but our Jones matrix is more general to account for some phase shifts in the fast-axis beam, as well. Our final result is unchanged by this. S is the effect of the sample, which quite generally, has left- and right-circularly polarized light as its eigenvectors and applies an unequal phase ($\delta_+ \neq \delta_-$; "circular birefringence") and an unequal Fresnel reflectance ($r_+ \neq r_-$; "circular dichroism") to each of the two helicities of light. The effect of the sample reflectance exchanging the handedness of circularly polarized light is not captured by S, but will rather be

accomplished by a complex conjugation later.

At the start of the beam path for the interferometer, unpolarized light exits our laser and encounters a polarizer, P, oriented such the power lost through cross-polarization of the source beam is minimized (the source diode outputs partially-polarized light). We will assume without loss of generality that polarizer angle is 0° so the starting point for our Jones calculus is

$$v = \begin{pmatrix} 1 \\ 0 \end{pmatrix}.$$

From our beam path we can simply apply the time-ordered Jones matrices of our optical components:

$$\mathrm{P}(0)\mathrm{WP}(\pi/8,\pi)\mathrm{EOM}(t+\tau)\mathrm{WP}(\pi/4,\pi/2)\left[\mathrm{S}\,\mathrm{WP}(\pi/4,\pi/2)\mathrm{EOM}(t)\mathrm{WP}(\pi/8,\pi)v\right]^{*}. \tag{3.22}$$

In words, we begin with linearly-polarized light that is polarized at 0° (v), the beam goes a half-wave plate that rotates the polarization of the beam to 45°, then goes through an EOM at time t, then through a quarter-wave plate, reflects from the sample, the LCP and RCP beams exchange due to the reflection (this is captured by the complex conjugation), goes through the quarter-wave plate again, through the EOM at a (now later) time $t+\tau$, and finally through the polarizer. We define τ as the time it takes for the beam to travel from the EOM to the sample and back. The result of the above matrix product is

$$\frac{ie^{-i(\delta_+ + \delta_-)}\left(r_- e^{i(\delta_- + \phi_\perp \sin\omega t + \phi_\parallel \sin[\omega(t+\tau)]} + r_+ e^{i(\delta_+ + \phi_\parallel \sin\omega t + \phi_\perp \sin[\omega(t+\tau)]}\right)}{2\,r_+ r_-} \begin{pmatrix} 1 \\ 0 \end{pmatrix}. \tag{3.23}$$

In our experiment, we specifically tune EOM frequency, ω, such that $\tau = \pi/\omega$

[61, 63]; this results in a substantial simplification:

$$\left(\frac{ie^{-i\delta_- + i\phi_m \sin\omega t}}{2\,r_-} + \frac{ie^{-i\delta_+ - i\phi_m \sin\omega t}}{2\,r_+}\right)\begin{pmatrix}1\\0\end{pmatrix} \tag{3.24}$$

where $\phi_m = \phi_\parallel - \phi_\perp$. We detect the time-averaged intensity of light so we take half of the complex square of the above to get:

$$\frac{1}{8\,r_-^2} + \frac{1}{8\,r_+^2} + \frac{1}{8\,r_-r_+}\left(e^{i(\delta_+ - \delta_-)}e^{2i\phi_m \sin\omega t} + e^{-i(\delta_+ - \delta_-)}e^{-2i\phi_m \sin\omega t}\right). \tag{3.25}$$

We then apply the Jacobi-Anger expansion to the exponentials and let $2\theta_k = \delta_+ - \delta_-$

$$\frac{1}{8\,r_-^2} + \frac{1}{8\,r_+^2} + \frac{1}{8\,r_-r_+}\left(e^{2i\theta_k}\sum_{n=-\infty}^{\infty} J_n(2\phi_m)e^{in\omega t} + e^{-2i\theta_k}\sum_{n=-\infty}^{\infty} J_n(2\phi_m)e^{-in\omega t}\right). \tag{3.26}$$

To measure the first harmonic signal, we use a lock-in amplifier to isolate the component proportional to $\sin(\omega t)$

$$\begin{aligned}
I^\omega =& \frac{1}{T}\int_T dt\left[\frac{1}{8\,r_-^2} + \frac{1}{8\,r_+^2}\right.\\
&\left. + \frac{1}{8\,r_-r_+}\left(e^{2i\theta_k}\sum_{n=-\infty}^{\infty} J_n(2\phi_m)e^{in\omega t} + e^{-2i\theta_k}\sum_{n=-\infty}^{\infty} J_n(2\phi_m)e^{-in\omega t}\right)\right]\sin\omega t\\
=& \frac{1}{2iT}\int_T dt\left[\frac{1}{8\,r_-r_+}\left(e^{2i\theta_k}\sum_{n=-\infty}^{\infty} J_n(2\phi_m)e^{in\omega t} + e^{-2i\theta_k}\sum_{n=-\infty}^{\infty} J_n(2\phi_m)e^{-in\omega t}\right)\right]\\
&\qquad \times\left[e^{i\omega t} - e^{-i\omega t}\right]\\
=& \frac{1}{2iT}\int_T dt\left[\frac{1}{8\,r_-r_+}\left(e^{2i\theta_k}\sum_{n=-\infty}^{\infty} J_n(2\phi_m)\left(e^{i(n+1)\omega t} - e^{i(n-1)\omega t}\right)\right.\right.\\
&\qquad\left.\left. + e^{-2i\theta_k}\sum_{n=-\infty}^{\infty} J_n(2\phi_m)\left(e^{-i(n-1)\omega t} - e^{-i(n+1)\omega t}\right)\right)\right].
\end{aligned} \tag{3.27}$$

The only terms in the sums that will survive the integration are those for which

the complex time-dependent exponentials are identically 1 (i.e. when $n+1=0$ or $n-1=0$):

$$\begin{aligned} I^{\omega} &= \frac{1}{2iT}\int_T dt\left[\frac{1}{8\,r_-r_+}\left[e^{2i\theta_k}\left(J_{-1}(2\phi_m)-J_1(2\phi_m)\right)+e^{-2i\theta_k}\left(J_1(2\phi_m)-J_{-1}(2\phi_m)\right)\right]\right] \\ &= \frac{1}{T}\int_T dt\frac{1}{8\,r_-r_+}\left[\sin 2\theta_k\left(J_{-1}(2\phi_m)-J_1(2\phi_m)\right)\right] \\ &= \frac{1}{8\,r_-r_+}\left[\sin 2\theta_k\left(J_{-1}(2\phi_m)-J_1(2\phi_m)\right)\right] \\ &= -\frac{\sin 2\theta_k J_1(2\phi_m)}{4\,r_-r_+}. \end{aligned} \tag{3.28}$$

Here we have used properties of the Bessel-J functions that $J_{-n}(x)=(-1)^nJ_n(x)$. We can compute the second harmonic (the $\cos 2\omega t$ component) using an analogous procedure (just by going back to the part where we introduced the $\sin\omega t$ and replacing that with a $\cos 2\omega t$ instead)

$$I^{2\omega} = -\frac{\cos 2\theta_k J_2(2\phi_m)}{4\,r_-r_+}. \tag{3.29}$$

Now we can calculate θ_k and also normalize out all of the dependences on the Fresnel amplitude coefficients (r_+ and r_-) by simply taking the ratio of the two signals:

$$\theta_k = \frac{1}{2}\arctan\left[\frac{J_2(2\phi_m)I^{\omega}}{J_1(2\phi_m)I^{2\omega}}\right]. \tag{3.30}$$

This is the MOKE signal with no MCD contribution and also no contribution from laser intensity fluctuations due to the normalization. Because we canceled the Fresnel amplitudes and normalized the laser intensity, this is the actual Kerr rotation in real units. Most conventional MOKE shown in the literature report Kerr rotation signals in a.u. For our measurements, we maximize the first harmonic signal ($\propto\theta_k$) by tuning ϕ_m to maximize $J_1(2\phi_m)$; this results in $\phi_m=0.92$ [63] and $J_2(2\phi_m)/J_1(2\phi_m)\approx 0.543$. The final expression that we use

to measure the Kerr rotation is

$$\theta_k = \frac{1}{2}\arctan\left[0.543\frac{I^{\omega}}{I^{2\omega}}\right]. \tag{3.31}$$

3.7.2 Measurement of changes in the Kerr angle $\Delta\theta_k$ due to current-induced magnetic deflections

To derive a similar result with an AC applied current, we can begin at equation (3.26) with an added oscillation from a time-dependent θ_k that results from current-induced tilting of the magnetic moment at the current frequency ω_e:

$$\frac{1}{8\,r_-r_+}\left(e^{2i(\theta_k+\Delta\theta_k\sin\omega_e t)}\sum_{n=-\infty}^{\infty}J_n(2\phi_m)e^{in\omega t}+e^{-2i(\theta_k+\Delta\theta_k\sin\omega_e t)}\sum_{n=-\infty}^{\infty}J_n(2\phi_m)e^{-in\omega t}\right). \tag{3.32}$$

We can apply the Jacobi-Anger expansion again

$$\frac{1}{8\,r_-r_+}\left(e^{2i\theta_k}\sum_{n,m=-\infty}^{\infty}J_n(2\phi_m)J_m(2\Delta\theta_k)e^{i(n\omega+m\omega_e)t}\right. \tag{3.33}$$

$$\left.+e^{-2i\theta_k}\sum_{n,m=-\infty}^{\infty}J_n(2\phi_m)J_m(2\Delta\theta_k)e^{-i(n\omega+m\omega_e)t}\right). \tag{3.34}$$

Now we demodulate this signal at the sideband frequency $\omega\pm\omega_e$. We will only show the $\omega+\omega_e$ derivation for sign simplicity, but the result is identical for the

upper and lower sidebands:

$$
\begin{aligned}
I^{\omega+\omega_e} =& \frac{1}{T}\int_T dt \frac{1}{8\,r_- r_+}\left(e^{2i\theta_k}\sum_{n,m=-\infty}^{\infty} J_n(2\phi_m)J_m(2\Delta\theta_k)e^{i(n\omega+m\omega_e)t}+\right.\\
&\left. e^{-2i\theta_k}\sum_{n,m=-\infty}^{\infty} J_n(2\phi_m)J_m(2\Delta\theta_k)e^{-i(n\omega+m\omega_e)t}\right)\times\cos\left(\omega t+\omega_e t\right)\\
=& \frac{1}{2T}\int_T dt \frac{1}{8\,r_- r_+}\left(e^{2i\theta_k}\sum_{n,m=-\infty}^{\infty} J_n(2\phi_m)J_m(2\Delta\theta_k)e^{i(n\omega+m\omega_e)t}+\right.\\
&\left. e^{-2i\theta_k}\sum_{n,m=-\infty}^{\infty} J_n(2\phi_m)J_m(2\Delta\theta_k)e^{-i(n\omega+m\omega_e)t}\right)\\
&\times\left(e^{\omega t+\omega_e t}+e^{-\omega t-\omega_e t}\right)
\end{aligned}
\tag{3.35}
$$

Again, to first order, the only complex exponentials that will survive integration are the ones where the exponent is identically zero. This leaves us with:

$$
\begin{aligned}
I^{\omega+\omega_e} =& \frac{1}{16\,r_- r_+}\left[e^{2i\theta_k}\left(J_{-1}(2\phi_m)J_{-1}(2\Delta\theta_k)+J_1(2\phi_m)J_1(2\Delta\theta_k)\right)+\right.\\
&\left. e^{-2i\theta_k}\left(J_{-1}(2\phi_m)J_{-1}(2\Delta\theta_k)+J_1(2\phi_m)J_1(2\Delta\theta_k)\right)\right]\\
=& \frac{1}{4\,r_- r_+}\cos 2\theta_k J_1(2\phi_m)J_1(2\Delta\theta_k).
\end{aligned}
\tag{3.36}
$$

In our experiments $\Delta\theta_k$ is very small so we use that $J_1(x)\approx x/2$ for small x

$$
I^{\omega+\omega_e} = \frac{\cos 2\theta_k J_1(2\phi_m)}{4\,r_- r_+}\Delta\theta_k. \tag{3.37}
$$

Finally, we take the ratio of this signal with the second harmonic (at ω) derived earlier to reach a simple expression for the current-induced change in the Kerr signal

$$
\Delta\theta_k = \frac{J_2(2\phi_m)I^{\omega+\omega_e}}{J_1(2\phi_m)I^{2\omega}}. \tag{3.38}
$$

Again we use $\phi_m = 0.92$, which results in the final expression we use to calculate $\Delta\theta_k$ is

$$\Delta\theta_k = 0.543\frac{I^{\omega+\omega_e}}{I^{2\omega}}. \tag{3.39}$$

3.8 Background and Definitions for this Chapter

3.8.1 Spin-Orbit Torques

For both the HH and Sagnac measurements, we again model the current-induced magnetic deflections using the Landau-Lifshitz-Gilbert-Slonczewski (LLGS) equation within a macrospin approximation [64]

$$\begin{aligned}\dot{\hat{m}} = \gamma\hat{m}\times\frac{dF}{d\hat{m}} \;+\; \alpha\hat{m}\times\dot{\hat{m}} \\ +\,\tau^0_{\mathrm{DL}}\hat{m}\times(\hat{\sigma}\times\hat{m}) \;+\; \tau^0_{\mathrm{FL}}\hat{\sigma}\times\hat{m}\end{aligned} \tag{3.40}$$

where $\hat{m}$ is the normalized magnetic moment of the FM, F is the free energy density of the FM, $\gamma = 2\mu_B/\hbar$ is the gyromagnetic ratio with μ_B the Bohr magneton, α is the Gilbert damping parameter, and $\hat{\sigma}$ is the direction of spin polarization impinging on the FM. The last two terms are a result of the SOT and can be written as

$$\tau^0_{\mathrm{DL(FL)}} = \xi_{\mathrm{DL(FL)}}\frac{\mu_B J_e}{eM_s t_{\mathrm{FM}}} \tag{3.41}$$

where $\xi_{\mathrm{DL(FL)}}$ is the dimensionless SOT efficiency for the damping-like (field-like) torque, J_e is the electric current density in the spin source layer applied in the X direction, M_s is the saturation magnetization of the FM, and t_{FM} is the thickness of the FM layer. The $\hat{X}$ and $\hat{Y}$ axes are defined as depicted in Figs. 3.1 & 3.7. In an amorphous-film system with high symmetry, we expect

$\sigma \parallel \hat{Y}$ for a current that goes in the X-direction; we will use this assumption throughout.

For samples with the magnetic moment oriented out-of-plane, the effects of current-induced torques can alternatively be expressed in terms of current-driven effective magnetic fields. The current-driven effective field in the X direction will correspond to the damping-like torque, $\mu_0 \Delta H_X = \mp \tau_{\mathrm{DL}}^0 / \gamma$, where the $\mp$ corresponds to the magnetic orientations $m_Z = \pm 1$. The current-induced effective field in the Y direction will be the sum of the field-like spin-orbit-torque contribution and the Ørstead field, $\mu_0 \Delta H_Y = \mu_0 H_{\mathrm{Oe}} \pm \tau_{\mathrm{FL}}^0 / \gamma$.

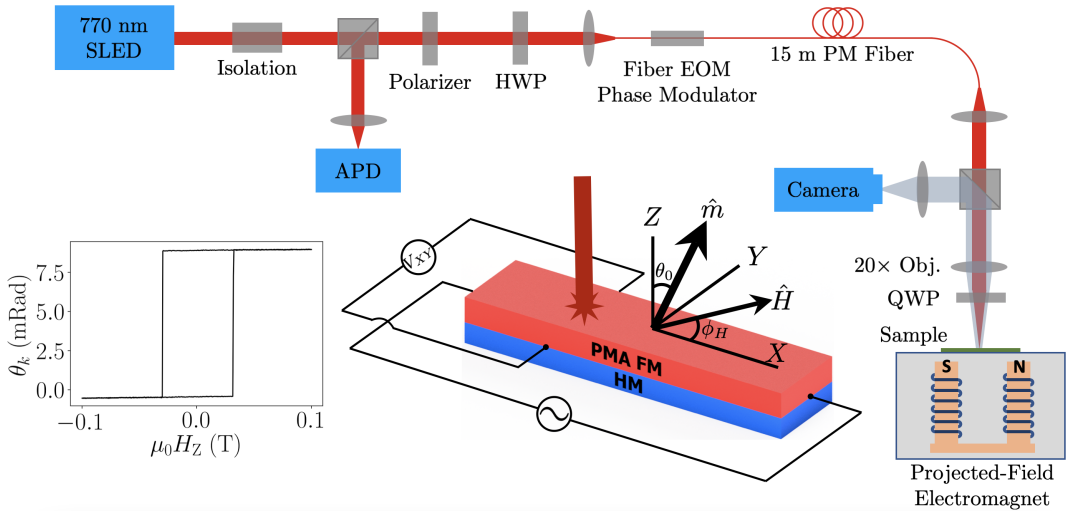

Figure 3.7: Schematic of the Sagnac interferometer. The left inset shows the Sagnac signal for magnetic-field-swept hysteresis of a Pt(4 nm)/Co(1.15 nm) device with $\mu_0 M_{\mathrm{eff}} \approx 0.42$ T; this is the same device for which we show data in Figs. 3.10 & 3.12. The right inset depicts the device structure and coordinate definitions. In our measurements, H is always applied in the XY -plane at $\phi_H = 0$ or $\pi/2$.

3.8.2 Harmonic Hall Measurement Technique

We consider harmonic Hall (HH) measurements for a spin-source/ferromagnet bilayer in which the magnet has PMA and is initially saturated along the $\pm Z$-axis. A small external magnetic field, H, is applied in-plane at an angle $\phi_H = 0$ or $\pi/2$ relative to the X-axis using a projected-field magnet. In the absence of applied current, the equilibrium polar angle (measured from Z-axis) of the magnetization, θ_0, can be written to good approximation as $\sin\theta_0 = H/M_{\text{eff}}$ where the effective magnetization, $\mu_0 M_{\text{eff}} = 2K_\perp/M_s - \mu_0 M_s$, is the out-of-plane anisotropy minus the saturation magnetization; with this definition M_{eff} is a *positive* quantity for a magnet with PMA. A low-frequency (non-resonant) AC voltage, $V(t) = \Delta I R_{XX} \sin\omega_e t$ [$\omega_e = 3137\ (2\pi)\text{s}^{-1}$ in our measurements], is applied to the device along the X-axis to generate deflections of the magnetic moment that can be characterized by current-induced effective fields ΔH_X and ΔH_Y. The Hall voltage along the Y-axis is measured.

For a system with a conducting magnet, the Hall resistance can depend on the magnetization orientation via both the anomalous Hall (AHE) and planar Hall effects (PHE), $R_{XY} = R_{\text{PHE}} m_X m_Y + R_{\text{AHE}} m_Z$. Given the AC current in the X direction, the Hall voltage will have a contribution at the drive frequency ω_e associated with the equilibrium magnetic orientation and a second-harmonic signal at $2\omega_e$ due to mixing between the AC current and the oscillations in R_{XY} produced by the magnetic deflections. For $\phi_H = 0$ or $\pi/2$, and within a small-angle approximation for θ_0 [33],

$$V_{XY}^{\omega} = \pm R_{\text{AHE}} \left(1 - \frac{H^2}{2M_{\text{eff}}^2}\right) \Delta I \tag{3.42}$$

$$\begin{aligned} V_{XY}^{2\omega} = &[\pm R_{\text{AHE}} (\Delta H_X \cos\phi_H + \Delta H_Y \sin\phi_H) \\ &- R_{\text{PHE}} (\Delta H_X \sin\phi_H + \Delta H_Y \cos\phi_H)] \\ &\times \frac{H}{2M_{\text{eff}}^2} \Delta I, \end{aligned} \tag{3.43}$$

where the $\pm$ accounts for magnetic saturation along the $\pm Z$-axis. The current-induced effective fields ΔH_X and ΔH_Y acting on the out-of-plane magnetic moment can then be calculated as [33]

$$\Delta H_X = -2\frac{D_0 \pm \epsilon D_{\pi/2}}{1-\epsilon^2} \tag{3.44}$$

$$\Delta H_Y = -2\frac{D_{\pi/2} \pm \epsilon D_0}{1-\epsilon^2} \tag{3.45}$$

where

$$D_{\phi_H} = \frac{dV_{XY}^{2\omega}(\phi_H)}{dH}\left(\frac{d^2V_{XY}^{\omega}(0)}{dH^2}\right)^{-1}. \tag{3.46}$$

and $\epsilon = R_{\mathrm{PHE}}/R_{\mathrm{AHE}}$. (These results are consistent with ref. [33] because our variable R_{AHE} is equal to $\Delta R_A/2$ in ref. [33] and hence our variable ϵ is equal to 2ξ in ref. [33].)

3.8.3 Sagnac MOKE Interferometry Technique

In our experiments we remain below the maximum values of $\theta_0 < 0.25$ Rad and $\Delta\theta < 10$ mRad. Given a typical value of the Kerr rotation angle upon full reversal of a 1 nm PMA Co film ($2\kappa = \theta_k(\pi) - \theta_k(0) \sim 9$ mRad, see Fig. 3.7) and that for small-angle-deflections from an out-of-plane configuration $\theta_k = \kappa m_Z$ so that the change in polar angle has a maximum value $|\Delta\theta_k| \approx \kappa \sin(\theta_0)\Delta\theta$, the oscillations in Kerr angle associated with the current-induced deflections are at most about 20 μRad. To achieve the sensitivity necessary to measure such small signals, we adapted a Sagnac interferometer design [61, 62, 65] able to measure Kerr rotation with noise less than 5 $\mu\mathrm{Rad}/\sqrt{\mathrm{Hz}}$. The design of the Sagnac MOKE apparatus is described in the preceding sections, and we compare the performance of conventional MOKE with our Sagnac apparatus in Fig. 3.8.

For measurements of current-induced torques with the Sagnac interferometer, we perform Sagnac and HH measurements simultaneously on the same

samples to make sure that any effects of the LED illumination do not cause differences between the two techniques. We therefore apply the same low-frequency AC voltage drive (at frequency ω_e) as in the HH experiments and detect the time-varying signal MOKE signal from the interferometer demodulated by a lock-in amplifier at both the driving frequency ω of the electro-optic phase modulator and (separately) at the lower-sideband frequency $\omega - \omega_e$ (see preceding sections). The signals at these frequencies measure the DC Kerr rotation (θ_k) associated with the magnetic-field-induced equilibrium tilt angle (θ_0) and the oscillations in the Kerr signal ($\Delta\theta_k$) associated with current-induced tilt ($\Delta\theta$), respectively. The expected Sagnac signals have the form

$$\theta_k = \pm\kappa \left(1 - \frac{H^2}{2M_{\text{eff}}^2}\right) \tag{3.47}$$

$$\Delta\theta_k = \pm\kappa \left(\Delta H_X \cos\phi_H + \Delta H_Y \sin\phi_H\right) \frac{H}{M_{\text{eff}}^2}. \tag{3.48}$$

Here κ is the constant of proportionality that relates the out-of-plane component of magnetization to the Kerr rotation, analogous to R_{AHE} for the electrical measurement. There is no MOKE contribution that acts like the PHE in equation [3.43] because Sagnac signal has negligible dependence on the in-plane components on the magnetic moment as shown in Fig. 3.9.

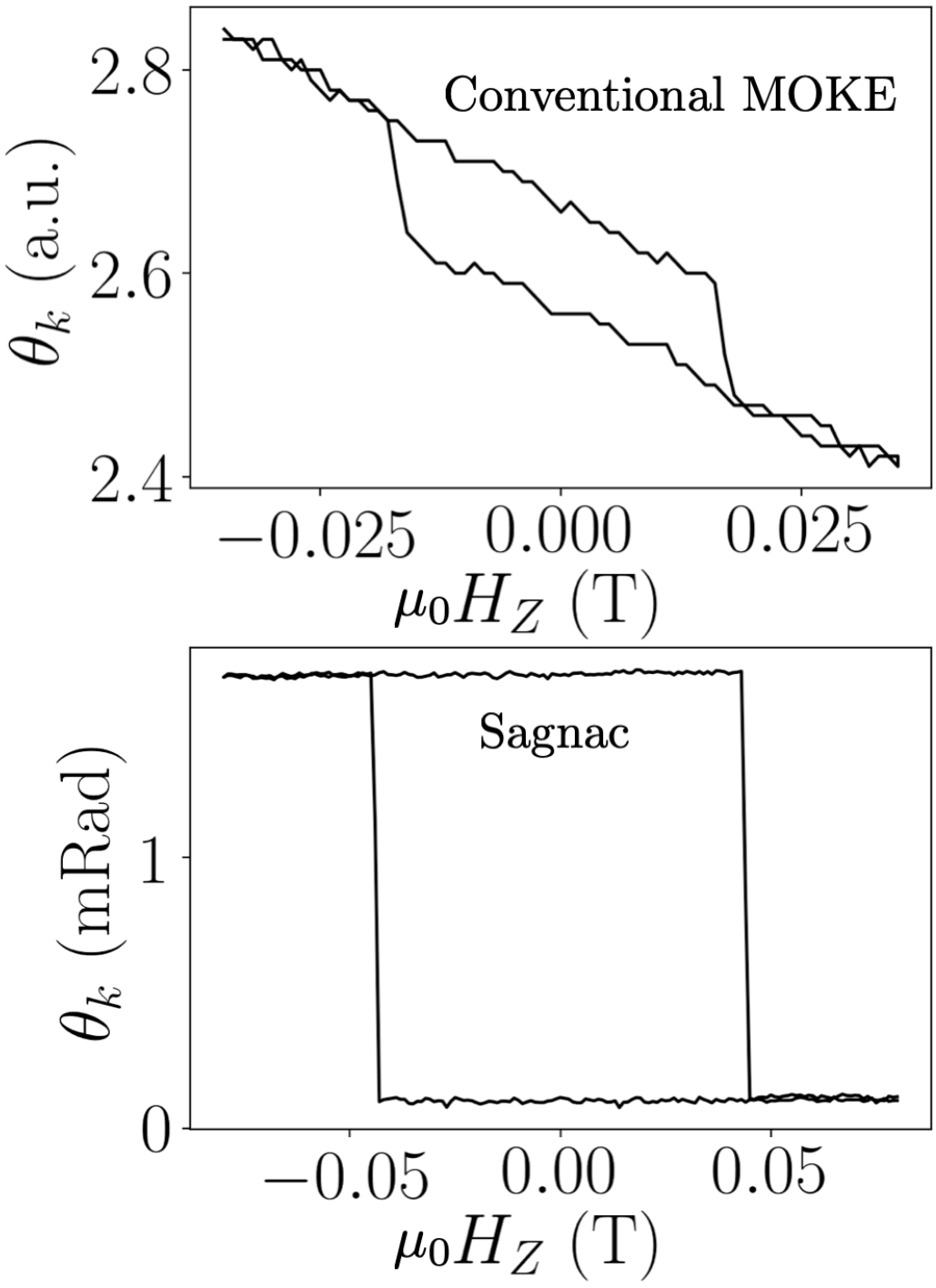

Figure 3.8: A comparison of a conventional MOKE measurement (top) and a Sagnac MOKE measurement (bottom). The conventional MOKE measurement is taken on a Ta(4 nm)/CoFeB(0.85 nm)/MgO sample, while the Sagnac MOKE measurement is taken on a Ta(4 nm)/CoFeB(0.65 nm)/MgO. The conventional MOKE measurement was taken with multiple back-and-forth averages (5 min measurement), so we estimate the noise equivalent power to be about 500 μRad/$\sqrt{\text{Hz}}$. The sagnac MOKE measurement was taken with one back-and-forth scan (15 second measurement), so we estimate the noise equivalent power to be about 5 μRad/$\sqrt{\text{Hz}}$.

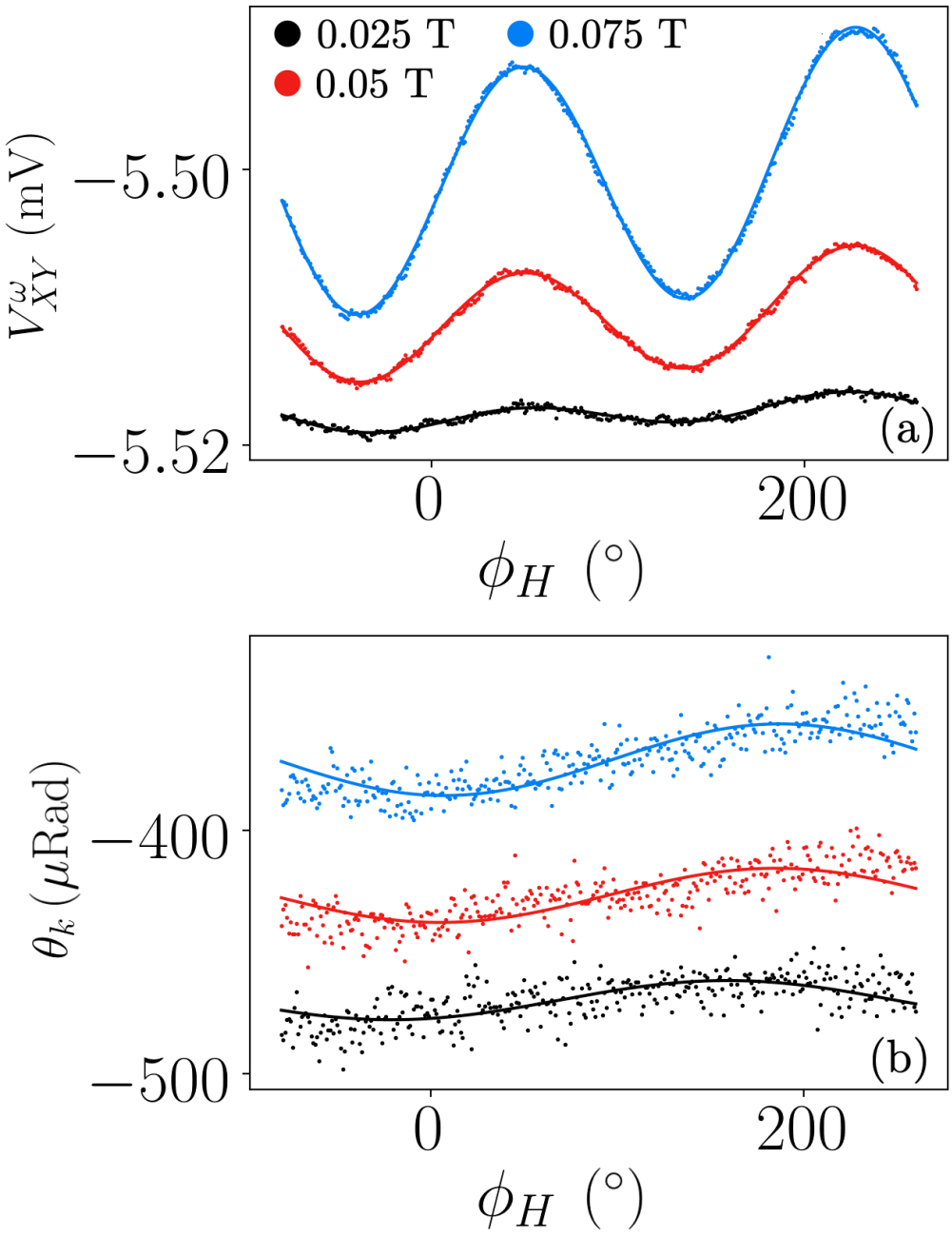

Figure 3.9: HH and Sagnac measurements as a function of the azimuthal angle (ϕ_H) of an in-plane-applied magnetic field with respect to the direction of applied current. **(a)** Measured first harmonic Hall voltage as a function of ϕ_H. **(b)** Measured Kerr rotation as a function of ϕ_H. The angle dependence of the Kerr rotation is very weak and does not have the proper symmetry expected from quadratic MOKE. The angle dependence of the Kerr rotation shown here is due to unintended out-of-plane stray magnetic field, which is also evident in the mismatched peaks in (a).

Based on these equations, for a PMA sample the component of the current-induced effective fields are simply

$$\Delta H_X = -\frac{d\Delta\theta_k(\phi_H = 0)}{dH}\left(\frac{d^2\theta_k}{dH^2}\right)^{-1} \tag{3.49}$$

$$\Delta H_Y = -\frac{d\Delta\theta_k(\phi_H = \pi/2)}{dH}\left(\frac{d^2\theta_k}{dH^2}\right)^{-1}. \tag{3.50}$$

3.9 Experimental Results

We will present measurements on two series of samples: Substrate/Ta(1.5)/Pt(4)/Co(0.85−1.3)/MgO(1.9)/Ta(2) and Substrate/Ta(1.5)/Pd(4)/Co(0.55−0.65)/MgO(1.9)/Ta(2) heterostructures where the numbers in parentheses are thicknesses in nanometers. Studying devices with different Co-layer thicknesses allows us to tune the strength of the out-of-plane magnetic anisotropy. The Hall-bar devices measured are 20 μm × 80 μm in size.

For each sample we calibrate the anomalous Hall coefficient R_{AHE} by measuring the change in Hall resistance upon magnetic switching as a function of out-of-plane magnetic field. The constant of proportionality κ relating m_Z to the Kerr-rotation angle is calibrated similarly (Fig. 1). To calibrate R_{PHE}, we rotate the field angle ϕ_H while applying a sequence of values of constant-strength in-plane magnetic field, and we measure the Hall voltage as shown in Fig. 3.10(a). We determine the magnetic anisotropy term $\mu_0 M_{\mathrm{eff}}$ from the first-harmonic Hall signal as a function of in-plane magnetic field swept along $\phi_H = 0$ or $\pi/2$ (see the discussion of Fig. 3.12(a,b) below) and then determine

R_{PHE} by fitting the measured dependence on ϕ_H to the form

$$\begin{aligned}\frac{V_{XY}^{\omega}}{\Delta I} =& R_{\mathrm{AHE}} \cos\left(\frac{H}{M_{\mathrm{eff}}}\right) \\ &+ R_{\mathrm{PHE}} \sin^2\left(\frac{H}{M_{\mathrm{eff}}}\right) \sin\phi_H \cos\phi_H \\ &+ R_{\mathrm{AHE}} \frac{H^2 \sin\theta_{\mathrm{off}}}{(M_{\mathrm{eff}})^2} \sin\left(\frac{H}{M_{\mathrm{eff}}}\right) \cos(\phi_H - \phi_{\mathrm{off}}),\end{aligned} \tag{3.51}$$

where the final term allows for a small misalignment of the applied field from the sample plane. The data fit well to this expected dependence – for the sample shown in Fig. 3.10 with an AC current amplitude $\Delta I = 9$ mA we determine $R_{\mathrm{PHE}} = 0.188(3)\ \Omega$ and $\theta_{\mathrm{off}} = 0.96(2)°$. Figure 3.10(b) shows that the amplitude of the planar-Hall voltage oscillations is proportional to H^2 as expected from equation [3.51]. The deflection angle induced over this range of applied magnetic field is in the range $\theta_0 < 15°$, the same range for which the SOT measurements are performed.

For the conversion from an effective field to spin-orbit torque efficiency (Eq. (3.41)), it is also necessary to calibrate the saturation magnetization M_s and the current density J_e in the spin-source layer. We measure M_s for each heterostructure using vibrating-sample magnetometry. We calculate J_e using a parallel-conduction model after determining the thickness-dependent conductivities of the different layers in the heterostructures as shown in Fig. 3.11.

3.9.1 Electrical Detection of SOT-induced tilting

The first- and second-harmonic Hall voltages measured for a Pt(4 nm)/Co(1.15 nm) device with a current amplitude $\Delta we = 15$ mA are shown in Fig. 3.12 for initial magnetic orientations both $m_Z = 1$ and -1.

We fit these data to Eqs. (3.42) & (3.43). From the curvature of the first harmonic we extract $\mu_0 M_{\mathrm{eff}} = 0.424(3)$ T, which is the result used in the calibration for R_{PHE}. The second-harmonic data in Fig. 3.12(c,d) fit well to straight lines, indicating that the effective fields ΔH_X and ΔH_Y are constant

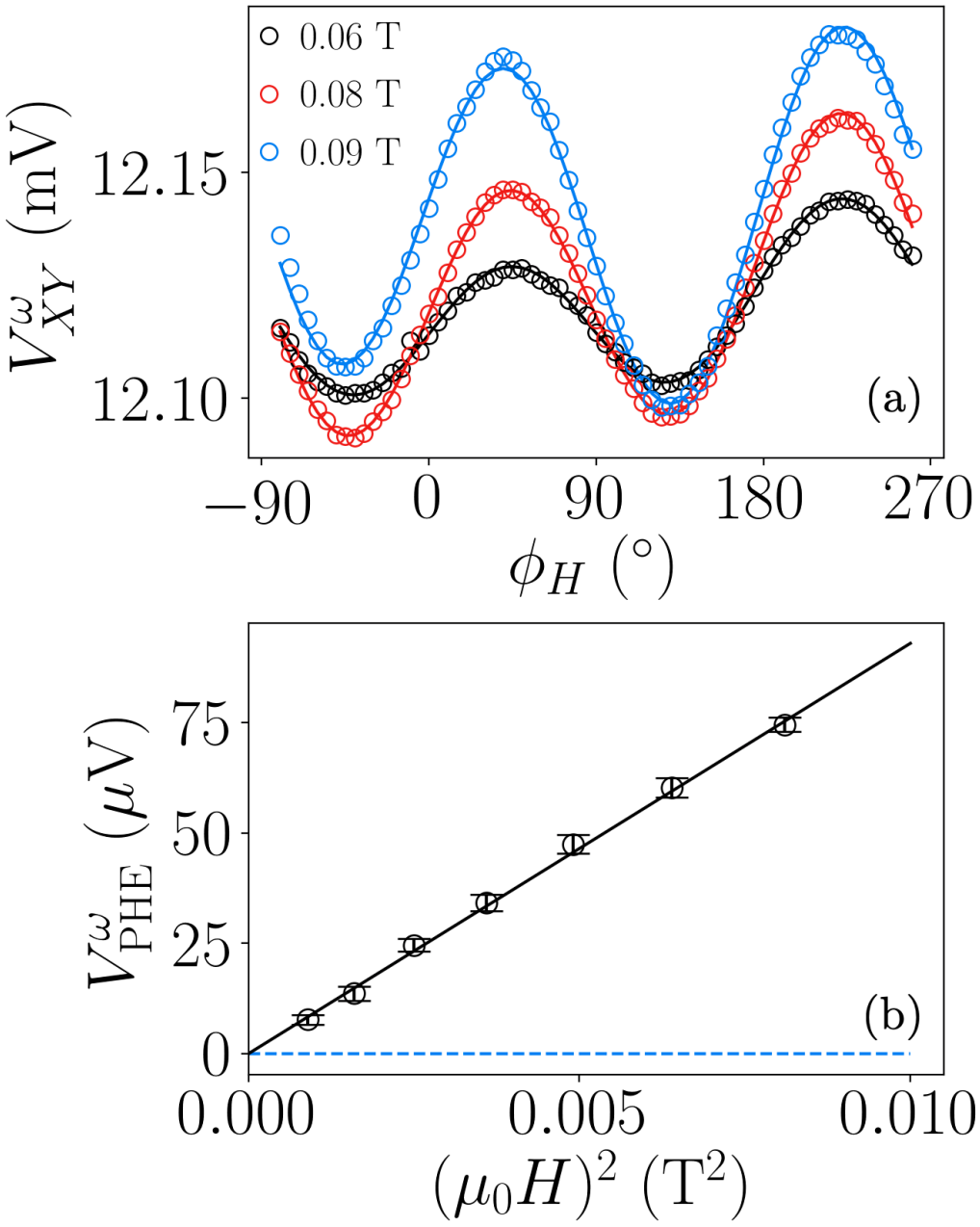

Figure 3.10: **(a)** First-harmonic PHE data measured on the Pt(4 nm)/Co(1.15 nm) device ($\mu_0 M_{\mathrm{eff}} \approx 0.42$ T). The lines overlayed are best fits to equation [3.51]. **(b)** The amplitude of the PHE signal in (a) vs. $(\mu_0 H)^2$. The line is a best fit that goes through the origin.

to a good approximation over the range of tilt angles in the measurement. From the slope of these lines and the curvature of the first harmonics, we use Eq. (3.46) to calculate that for $m_Z = -1$: $\mu_0 D_0 = -2.01(2)$ mT and $\mu_0 D_{\pi/2} = 0.62(1)$ mT, and for $m_Z = +1$: $\mu_0 D_0 = 2.21(2)$ mT and $\mu_0 D_{\pi/2} = 0.45(1)$ mT. Together with the values $R_{\mathrm{PHE}} = 0.188(3)\ \Omega$ and $R_{\mathrm{AHE}} = 0.355(6)\ \Omega$ calibrated

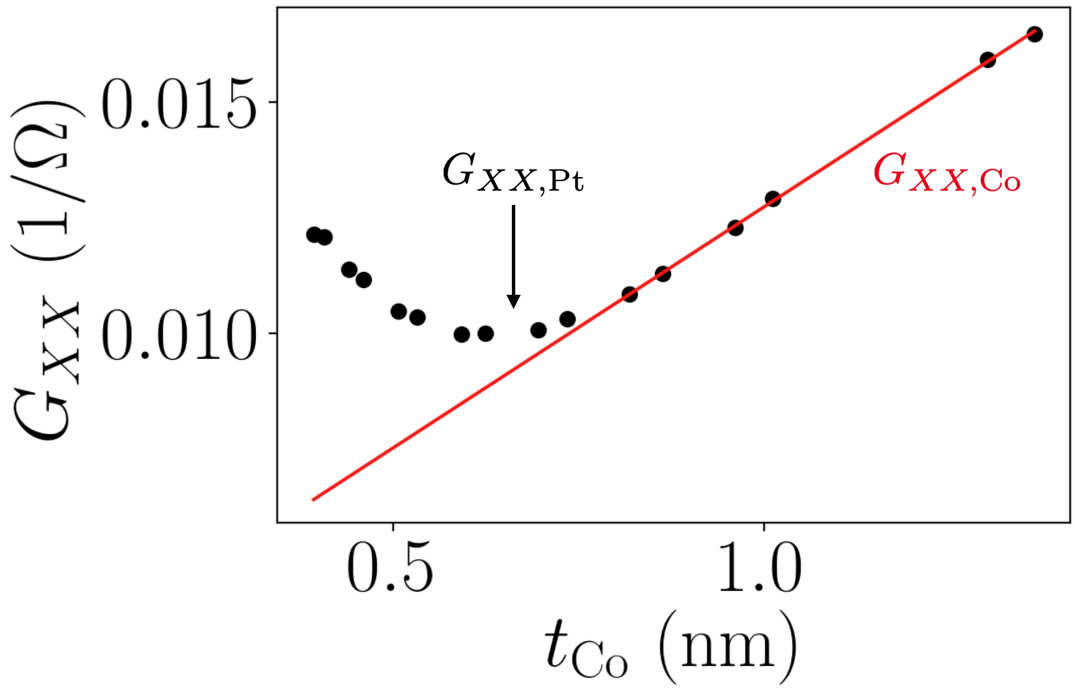

Figure 3.11: The measured conductance of the Pt(4 nm)/Co(t_{Co}) device stacks. All measurements were performed on the same wafer, which was grown as a Co wedge. The red line is a best fit to the thicker Co data.

as described, the standard HH analysis framework (equations (3.44) & (3.45)) then yields the effective fields $\mu_0\Delta H_X = 6.75(6)$ mT and $\mu_0\Delta H_Y = -4.94(3)$ mT for the $m_Z = -1$ initial state and $\mu_0\Delta H_X = -6.80(4)$ mT and $\mu_0\Delta H_Y = -4.33(3)$ mT for the $m_Z = +1$ configuration.

3.9.2 Optical Detection of SOT-Induced Tilting

The Sagnac MOKE readouts measured simultaneously with the HH data from Fig. 3.12(a-d) are shown in Fig. 3.12(e-h). The signal-to-noise ratio for $\Delta\theta_k$ in the Sagnac measurements is not quite as high as for $V_{XY}^{2\omega}$ in the HH measurements, but it is good enough to test inconsistencies between the results of the standard HH analysis on PMA samples and the spin-orbit-torque efficiencies determined by HH measurements on in-plane samples [66]. A fit of the parabolic dependence of θ_k to equation [3.48] yields $\mu_0 M_{\mathrm{eff}} = 0.418(3)$ T, in good agreement with value determined by HH. The values of the current-induced effective fields for this sample are determined from the slopes of the

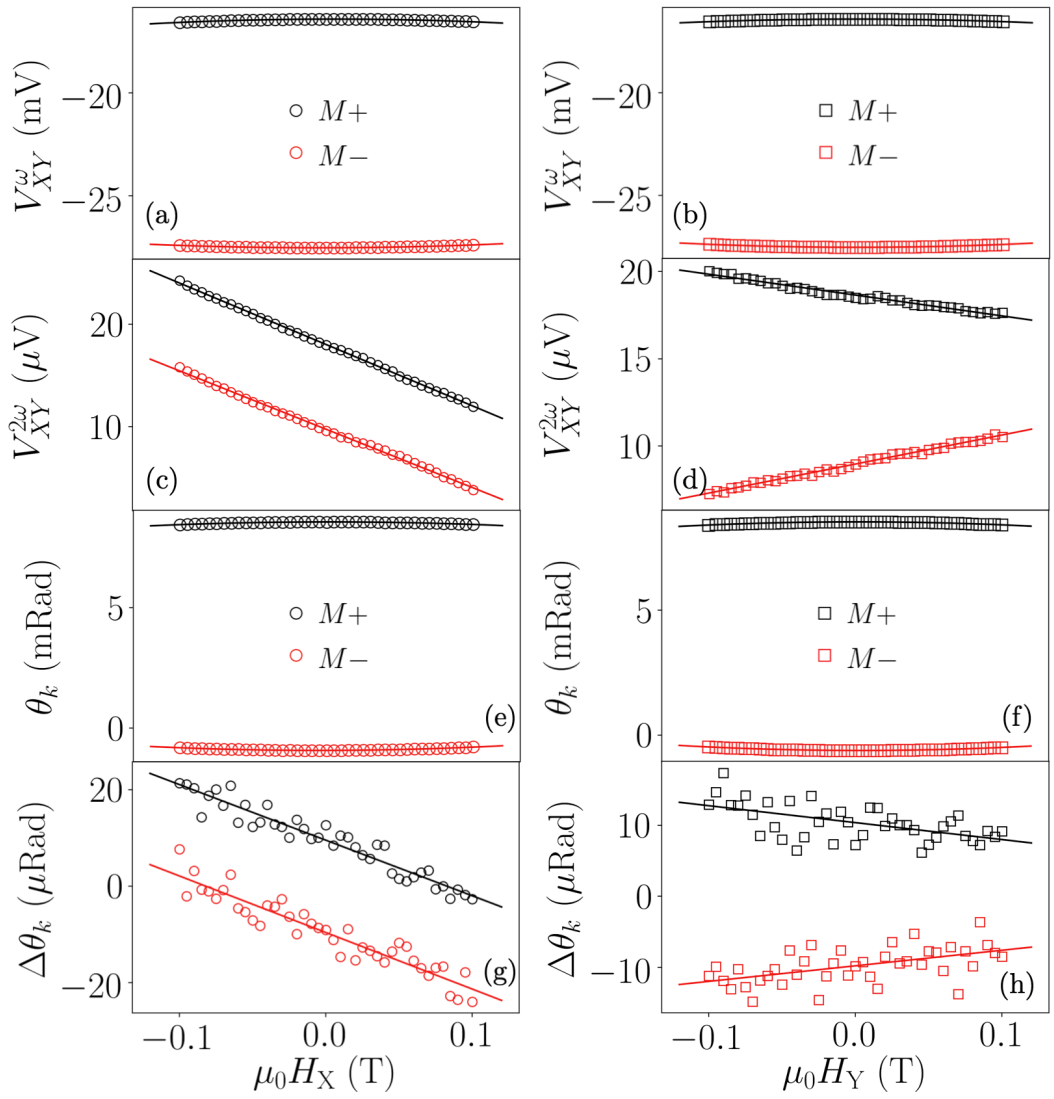

Figure 3.12: Measured HH and optical tilting data collected on a Pt(4 nm)/Co(1.15 nm) device with $\mu_0 M_{\text{eff}} \approx 0.42$ T and current amplitude $\Delta I = 15$ mA. First-harmonic Hall data as a function of magnetic field swept **(a)**: along the current direction and **(b)**: perpendicular to the current direction. Second-harmonic Hall data as a function of magnetic field swept **(c)**: along the current direction and **(d)**: perpendicular to the current direction. Equilibrium Kerr rotation θ_k as a function of magnetic field swept **(e)**: along the current direction and **(f)**: perpendicular to the current direction. Current-induced change in the Kerr rotation $\Delta\theta_k$ as a function of magnetic field swept **(g)**: along the current direction and **(h)**: perpendicular to the current direction. The second-harmonic Hall and $\Delta\theta_k$ data for the two different magnetic configurations are offset for clarity.

lines in Fig. 3.12(g,h) together with Eqs. (3.49) & (3.50). For a current of $\Delta I = 15$ mA we find $\mu_0 \Delta H_X = 5.1(3)$ mT and $\mu_0 \Delta H_Y = -0.9(2)$ mT for the $m_Z = -1$ initial state and $\mu_0 \Delta H_X = -5.0(3)$ mT and $\mu_0 \Delta H_Y = -0.9(2)$

mT for the $m_Z = +1$ configuration. These signs result in a positive DL SOT efficiency, ξ_{DL} (consistent with literature [66]) and a negative net FL torque, which indicates that there is a contribution from the FL torque counteracting the torque from the Ørsted field [67].

We have performed similar analyses for two series of Pt/Co/MgO and Pd/Co/MgO samples with different Co thicknesses. The final results for the effective fields measured by Sagnac interferometry normalized by current density flowing through the Pt or Pd are shown by the symbols in Fig. 3.13. To obtain these values, for each sample we measured ΔH_X and ΔH_Y for a sequence of applied voltage amplitudes and fit to a linear dependence (see Eq. (3.41)). We compare these Sagnac results to values determined by the HH technique, for both the standard analysis that takes into account the planar Hall signal using the measured value of ϵ (filled lines) and, following the suggestion of Zhu et al. [66] to arbitrarily set $\epsilon = 0$ in equations (3.44) & (3.45) (empty lines). The width of each line indicates the 1-σ error bar for that sample. (Note in Fig. 3.14 that for the $t_{\mathrm{Co}} = 1.25$ nm sample we do not present a value for the conventional HH analysis or $\mu_0 \Delta H_Y / J_e$. Because of the relatively-weak PMA of this sample, to prevent domain formation during sweeps of in-plane magnetic field it was necessary to apply simultaneously a small constant out-of-plane magnetic field. Our projected-field magnet was capable of performing this measurement for $\phi_H = 0$ but not for $\phi_H = \pi/2$ without moving the sample.)

From Fig. 3.13 we see that for both the Pt/Co and Pd/Co samples the Sagnac results are very different from the results of the standard HH analysis that takes into account the expected planar Hall signal. They are in much better agreement with the HH results if one assumes that the planar Hall effect somehow makes a negligible contribution to the second-harmonic Hall voltage. For the Pt/Co samples (for which $\epsilon = R_{\mathrm{PHE}}/R_{\mathrm{AHE}} \approx 0.5$), the standard HH analysis determines a value of $\mu_0 \Delta H_X / J_e$ that is is approximately 60% larger than the other values, while for the Pd/Co samples (for which $\epsilon = 0.7$ - 0.9), the

standard HH framework can overestimate $\mu_0 \Delta H_X / J_e$ by as much as a factor of 15.

For the Pt/Co samples, the values of the field-like component $\mu_0 \Delta H_Y / J_e$ extracted by the standard HH analysis are also in stark disagreement with the Sagnac results, while the HH analysis with ϵ arbitrarily set to 0 again agrees much better with the Sagnac values. For the Pd/Co samples, $\mu_0 \Delta H_Y / J_e$ is sufficiently weak that the uncertainties in the Sagnac measurements are comparable to the measured values, so we do not show them.

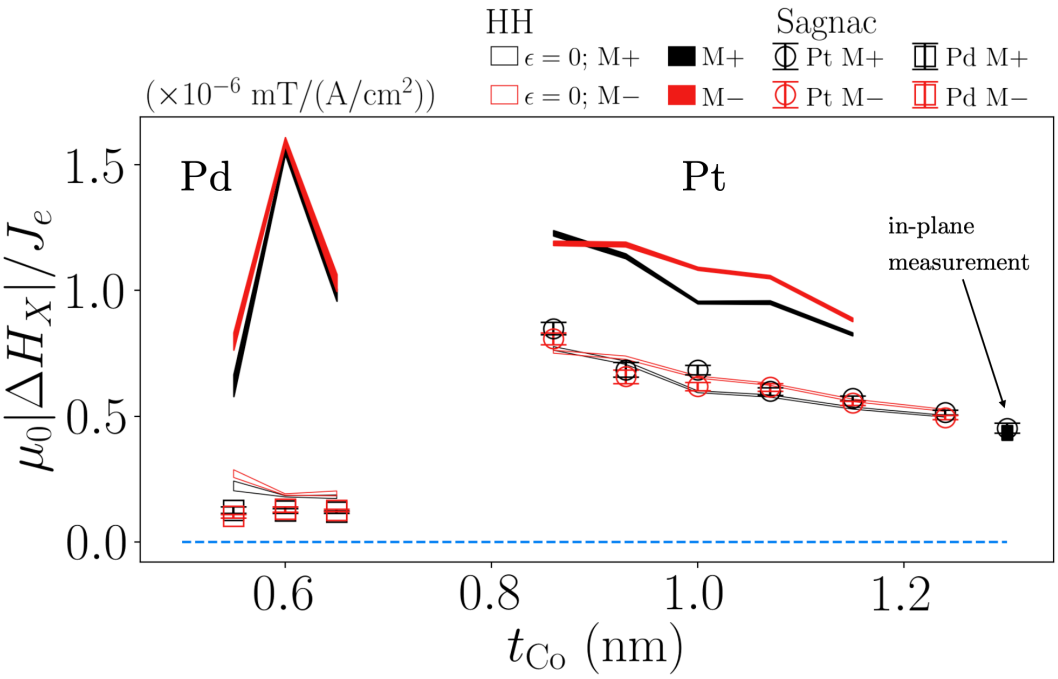

Figure 3.13: Calculated current-induced effective fields normalized by the current density in the Pt or Pd layer. **(a)**: $\mu_0 |\Delta H_X| / J_e$ across seven devices on the Pt/Co wafer and three devices on the Pd/Co wafer. The data points are results from the Sagnac optical measurements. Filled lines are results from the conventional HH analysis. Empty lines are results of a HH analysis assuming arbitrarily that $\epsilon = 0$ in equations (5) and (6). The thicknesses of the lines denote 1σ error bars.

3.9.3 Electrical and Optical Measurements on a PMA Sample Tilted In-Plane

Our results so far have demonstrated that the conventional HH analysis gives results inconsistent with the Sagnac measurements, but they do not prove which

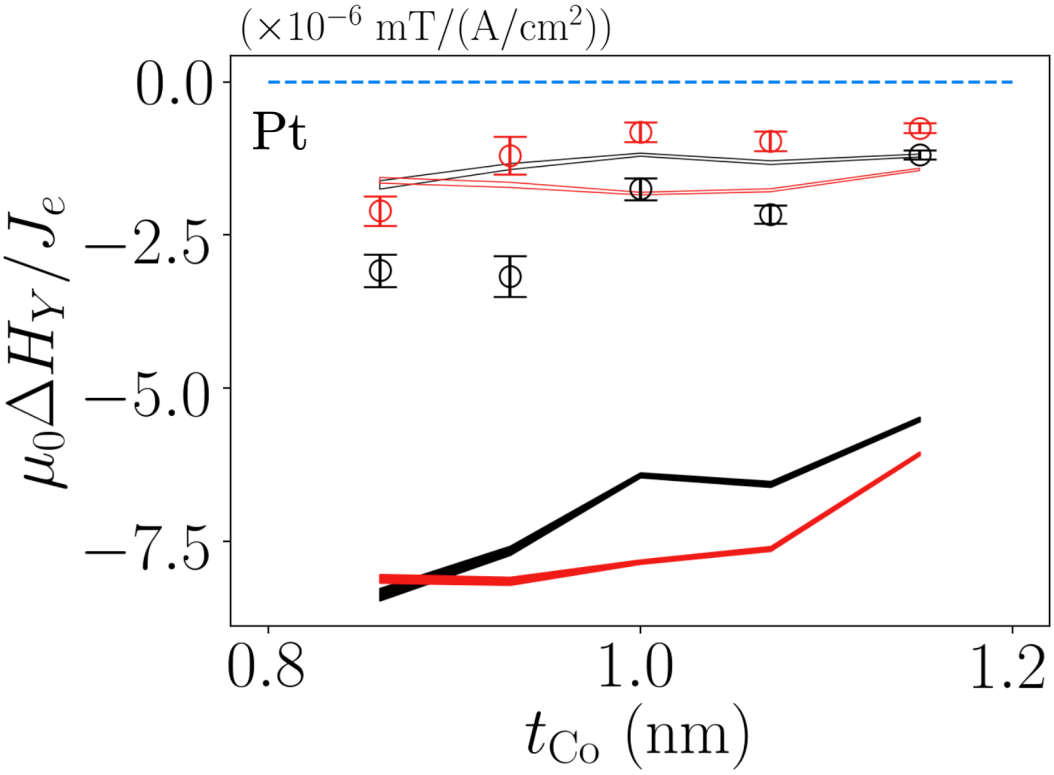

Figure 3.14: Calculated current-induced effective fields normalized by the current density in the Pt or Pd layer. $\mu_0 \Delta H_Y / J_e$ for devices on the Pt/Co wafer. The data points are results from the Sagnac optical measurements. Filled lines are results from the conventional HH analysis. Empty lines are results of a HH analysis assuming arbitrarily that $\epsilon = 0$ in equations (5) and (6). The thicknesses of the lines denote 1σ error bars.

technique is incorrect. For that we consider additional measurements on a sample from the same wafer as our other Pt/Co/MgO devices, but with a sufficiently-thick Co layer that the PMA is weak – specifically, we measure a Pt(4 nm)/Co(1.3 nm) sample with $\mu_0 M_{\mathrm{eff}} = 0.05$ T. This weak value of PMA allows us to force the magnetization in-plane with a sufficiently-large in-plane magnetic field, and perform in-plane HH measurements as a function of the field angle ϕ_H. In this geometry, the current-induced damping-like effective field points out-of-plane, and it can be measured with no confusion about contributions from the planar Hall effect to first order.

Figure 3.15 shows both Sagnac MOKE and second-harmonic Hall data as a function of ϕ_H for this Pt(4 nm)/Co(1.3 nm) sample with a current amplitude $\Delta I = 13$ mA, subject to a constant magnitude of magnetic field ($\mu_0 H = 0.1$,

0.15, and 0.2 T).

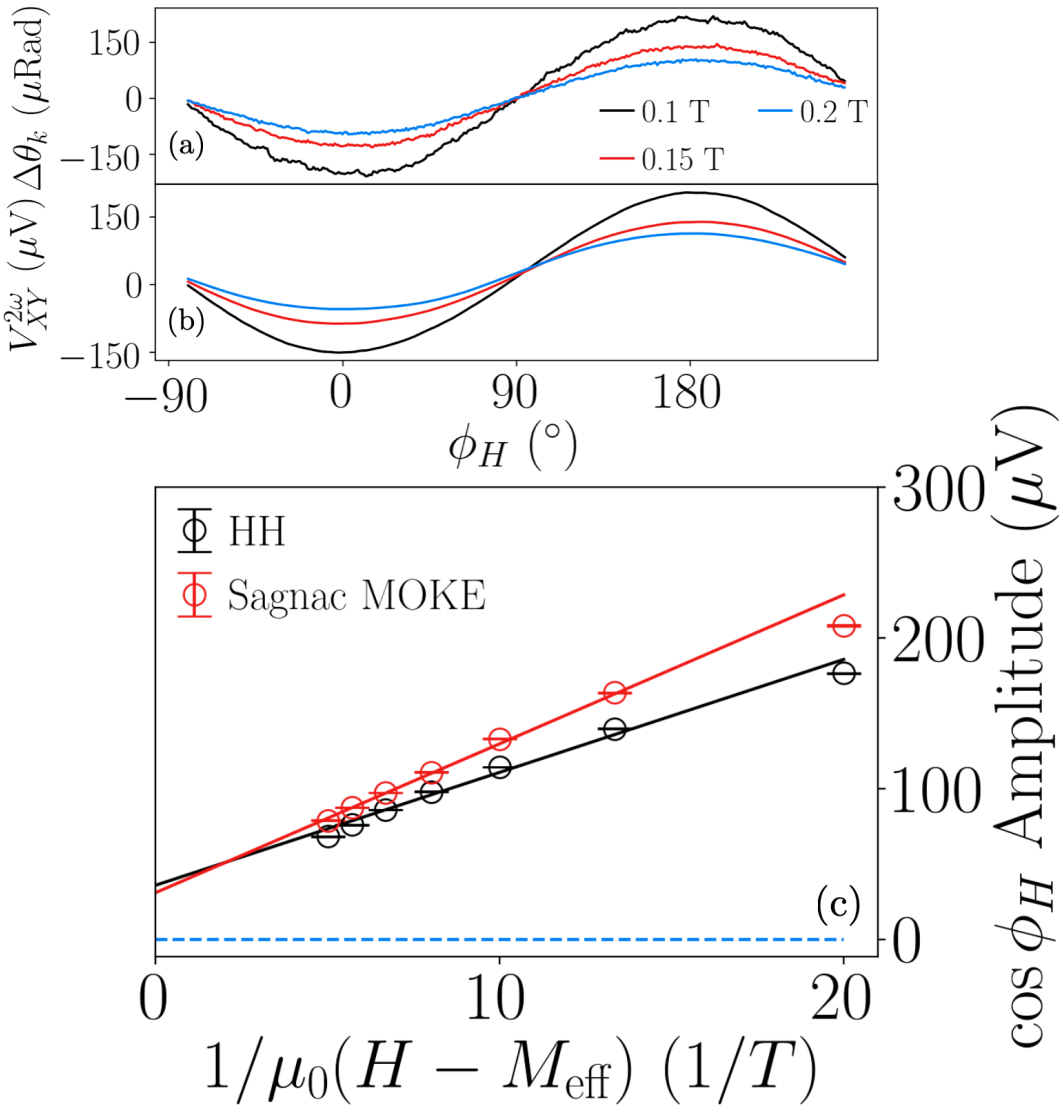

Figure 3.15: **(a)** Second-harmonic Hall voltage ($V_{XY}^{2\omega}$) and **(b)** differential Kerr rotation ($\Delta\theta_k$) measured as a function of the angle of magnetic field, ϕ_H for a weakly PMA Pt/Co/MgO device with $\mu_0 M_{\text{eff}} = 0.05$ T with an applied current of $\Delta I = 13$ mA. **(c)** Amplitude of the $\cos\phi_H$ components in both measurements with linear fits to to equations (3.52) and (14).

We fit to the form of the signals expected for small-angle deflections in the case of an in-plane equilibrium angle [33, 28, 53]

$$\Delta\theta_k = -\frac{\kappa\Delta H_{\mathrm{DL}}\cos\phi_H}{H - M_{\mathrm{eff}}} \tag{3.52}$$

$$\begin{aligned} V_{XY}^{2\omega} =& (V_{\mathrm{AHE}}^{2\omega} + V_{\mathrm{ANE}}^{2\omega})\cos\phi_H + V_{\mathrm{PHE}}^{2\omega}\cos\phi_H\cos 2\phi_H \\ =& -\frac{\Delta I R_{\mathrm{AHE}}\Delta H_{\mathrm{DL}}\cos\phi_H}{2(H - M_{\mathrm{eff}})} + V_{\mathrm{ANE}}^{2\omega}\cos\phi_H \\ & - \frac{\Delta I R_{\mathrm{PHE}}\Delta H_{\mathrm{FL}}\cos\phi_H\cos 2\phi_H}{2H}, \end{aligned} \tag{3.53}$$

where $V_{\mathrm{ANE}}^{2\omega}$ is a voltage contribution from the anomalous Nernst effect. To isolate the signals due to ΔH_{DL}, we plot the amplitude of $\cos\phi_H$ components as a function of $1/\mu_0(H - M_{\mathrm{eff}})$ and perform linear fits as shown in Fig. 3.15(c). We find $\mu_0\Delta H_X/J_e = 4.3(3)$ ($\times 10^{-14}$ T/(A/m^2)) from the HH measurement and $\mu_0\Delta H_X/J_e = 4.5(2)$ ($\times 10^{-14}$ T/(A/m^2)) from the Sagnac MOKE measurement. These points are included in the overall summary plot in Fig. 3.13 with the arrow indicating "in-plane measurement." We observe no significant $\cos\phi_H\cos 2\phi_H$ component in the HH data for this sample. This could be because ΔH_{FL} might simply be small for this sample due to accidental cancellation between the Ørsted field and the field-like torque, so we do not draw any conclusions about the contribution of the planar Hall effect to the output signal for this particular sample. For other samples with fully-in-plane anisotropy, the planar Hall effect does contribute unambiguously to give strong $\cos\phi_H\cos 2\phi_H$ signals for in-plane second-harmonic Hall measurements (see, e.g., [11]).

The results of the in-plane HH and Sagnac measurements for the weakly-PMA device agree well with one another. They are also consistent with the extrapolation of the Sagnac measurements from the PMA samples to a Co thickness of 1.3 nm, but they are considerably less than expected from an extrapolation of the conventional HH analysis for the PMA samples (Fig. 3.13).

Based on this we argue that the conventional HH analysis that includes the expected contribution from the planar Hall effect is incorrect. We also note that if we arbitrarily ignore the expected planar Hall contribution to the HH experiment by seting $\epsilon = 0$ in Eqs. (3.44) and (3.45), then the results of the PMA HH measurements become reasonably consistent with all of the other measurement techniques.

To be more quantitative, we compare the measured values of the damping-like torque efficiency ξ_{DL} between different samples and different measurement techniques. Unlike the current-induced effective fields, ξ_{DL} is expected to be approximately independent of t_{Co}, and indeed we find this to be the case for the strong-PMA samples as shown in Fig. 3.16.

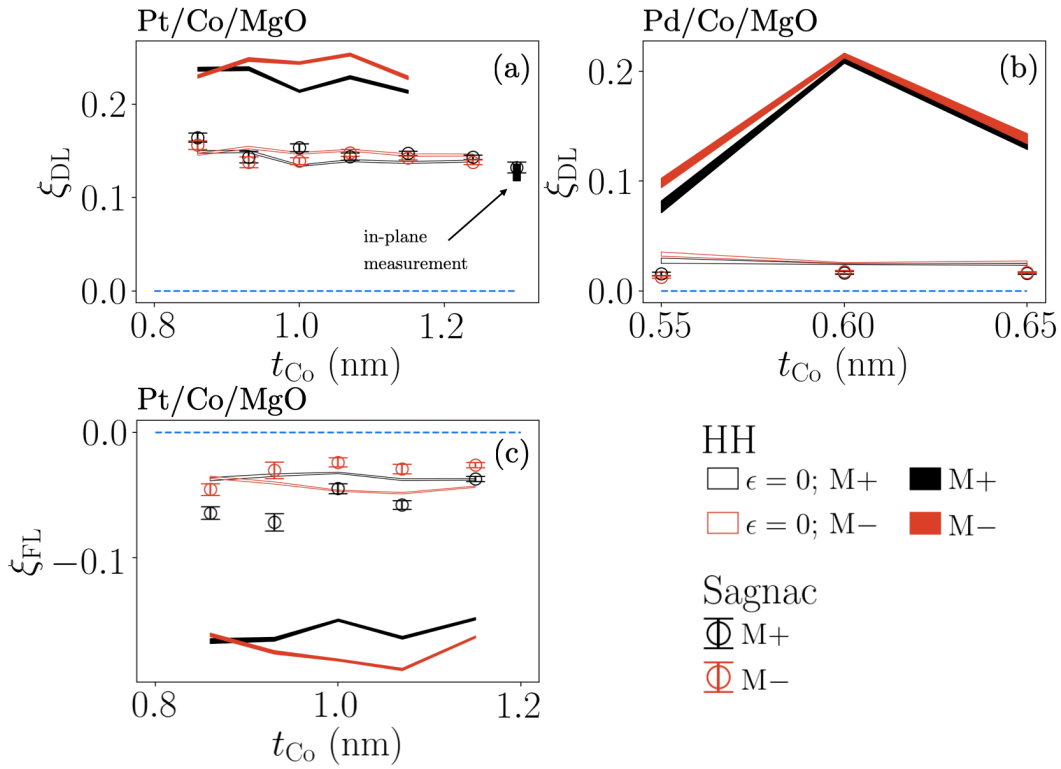

Figure 3.16: ξ_{DL} and ξ_{FL} as a function of Co thickness in both Pt/Co and Pd/Co stacks. These are the same data as those shown in Figs. 3.13 & 3.14, with the y-axis rescaled from effective fields to unitless SOT efficiencies.

Table 3.1 compares the average value of ξ_{DL} extracted from the HH measurements on the strong-PMA samples (using both the measured value of ϵ and then arbitrarily setting $\epsilon = 0$) to the Sagnac-MOKE measurements on the

strong-PMA samples, as well as to the HH and Sagnac-MOKE measurements on the weakly-PMA sample. Clearly, the outlier is the conventional HH analysis that includes the expected signal from the planar Hall effect.

ξ_{DL}	HH	Sagnac MOKE
strong-PMA tilting	0.23(1)	0.146(8)
strong-PMA tilting ($\epsilon = 0$)	0.145(6)	–
weak-PMA angle-dependence	0.127(7)	0.132(6)

Table 3.1: Comparison of the dampinglike spin-orbit torque efficiencies ξ_{DL} measured on strong-PMA devices using small-angle tilting from an initial out-of-plane magnetic orientation (Fig. 3.13 and Fig. 3.16) with values measured on a weakly-PMA sample using small-angle tilting from in-plane initial configurations (Fig. 3.15).

3.9.4 Discussion

What is wrong about the standard framework for analyzing HH measurements of PMA samples, that it yields values for the current-induced effective fields that differ from the other techniques? Why does arbitrarily ignoring the expected planar Hall signal (i.e., arbitrarily setting $\epsilon = 0$ in Eqs (3.44) & (3.45) in the HH analysis) give results in better agreement with these other methods?

We have considered whether the form of the current-induced effective fields might differ from the standard assumption that ΔH_X and ΔH_Y are approximately constant in the neighborhood of equilibrium tilt angles near $\theta_0 = 0$. If the current-induced effective fields were purely polar, so that there was no in-plane component to the current-induced magnetic deflections, this could explain the lack of a contribution to the second-harmonic Hall voltages from the planar Hall effect for $\phi_H = 0$ and $\pi/2$. However, we believe that this is unphysical. The HH results on the strongly-PMA samples imply that current-induced effective fields extrapolate to non-zero values at $\theta_0 = 0$, so if they were purely polar this would require a an unphysical discontinuity. A purely-polar effective field would furthermore alter the dependence of the HH measurements on ϕ_H for values other than 0 and $\pi/2$, making them inconsistent with our

angle-dependent measurements.

We have also considered whether the PMA samples might possess a nonlinear-in-current Hall effect not associated with magnetic dynamics that might largely cancel the signal expected from the PHE read-out of the current-excited magnetic dynamics. Nonlinear-in-current Hall effects have been detected in topological-insulator-based devices [68, 69] and might also arise from heating-induced Nernst signals. We suggest that this possibility deserves further analysis for heavy-metal-based structures, but we would find it a curious coincidence if a mechanism of this sort could approximately cancel the planar-Hall readout signal of spin-orbit torques in both the Pt/Co and Pd/Co devices.

We therefore conclude that the error in the standard HH analysis is most likely in the read-out mechanism involving the planar Hall effect. Our experiments suggest that for our PMA samples magnetic deflection induced by an applied current does not produce the same change in planar Hall resistance as the same magnetic deflection produced by an applied magnetic field. We do not claim that the contribution of the planar Hall effect to HH signals of current-induced magnetic deflection in PMA samples is necessarily exactly zero, but it does appear to be far smaller than expected based on calibration of the planar Hall effect using magnetic-field-induced magnetic deflection – and negligible to a good approximation.

We do not yet have a good microscopic explanation for why the planar Hall effect should not contribute to second-harmonic Hall signals for PMA samples while it does for samples with in-plane anisotropy [11]. We can speculate that magnetic tilting associated with spin-orbit torques will involve non-equilibrium spin-accumulations that are not present for magnetic-field-induced magnetic tilting, and that perhaps such spin accumulations might affect the Hall signal. In any case, this puzzle highlights that we still lack a basic understanding about fundamental aspects of interactions among charge currents, spin currents, and ferromagnets.

3.10 Conclusion

We have shown measurements of current-induced torques in PMA Pt/Co/MgO and Pd/Co/MgO samples performed by simultaneously detecting small-angle current-induced magnetization tilting using both harmonic Hall (HH) measurements and Sagnac MOKE interferometry. We find that the conventional HH analysis, which takes into account the expected read-out signals due to the planar Hall effect, is inconsistent with the Sagnac MOKE results. The Sagnac measurements for the damping-like torque in the PMA samples are, however, consistent with both harmonic Hall and Sagnac measurements on a weakly-PMA sample forced to an initial in-plane orientation by an applied magnetic field. These results indicate that the conventional harmonic Hall analysis for PMA samples, used in hundreds of published papers, gives incorrect values for spin-orbit torques in samples for which the planar Hall effect is significant. (For materials in which the magnetic-field-induced planar Hall effect is negligible, we do not claim any problem.) We find phenomenologically that the conventional HH analysis for PMA samples can be improved, yielding results in better agreement with other measurement techniques, by arbitrarily ignoring the expected signal from the planar Hall effect (i.e., arbitrarily setting ϵ equal to zero in equations (3.44) & (3.45)). Our findings help to explain previous reports of apparently-unphysical results from the conventional HH analysis [57, 58, 70, 71, 59, 66]. We do not yet have a microscopic understanding of why current-induced magnetization tilting produces a negligible planar Hall signal in PMA samples, while the same magnetization tilting produced by an applied magnetic field does generate a planar Hall effect.

Chapter 4

Concluding Remarks

The current suite of SOT measurement techniques leaves something to be desired: consistency. Consistency is needed to demonstrate the viability of the SOT mechanism for technologies; without it, industries cannot trust the numbers and will not dedicate funding to pursue SOT technology. Therefore, studying the measurements, metrology, is an important pursuit for the community. Relitigating the measurements that we (the community) use every day through the lens of metrology can teach us from where the discrepancies arise and how to fix them. Metrology is also a unique epistemological direction from which to discover new physics – found artifacts in measurements can be interesting themselves.

Bibliography

[1] M. L. Rieger, "Retrospective on VLSI value scaling and lithography," *Journal of Micro/Nanolithography, MEMS, and MOEMS*, vol. 18, p. 1, Nov. 2019.

[2] C. Kittel, "On the theory of ferromagnetic resonance absorption," *Physical Review*, vol. 73, pp. 155–161, Jan 1948.

[3] F. Keffer and C. Kittel, "Theory of antiferromagnetic resonance," *Phys. Rev.*, vol. 85, pp. 329–337, Jan 1952.

[4] D. MacNeill, J. T. Hou, D. R. Klein, P. Zhang, P. Jarillo-Herrero, and L. Liu, "Gigahertz frequency antiferromagnetic resonance and strong magnon-magnon coupling in the layered crystal $CrCl_3$," *Phys. Rev. Lett.*, vol. 123, p. 047204, Jul 2019.

[5] "Zurich instruments white paper: Principles of lock-in detection and the state of the art," *Zurich Instruments White Paper: Principles of lock-in detection and the state of the art.*

[6] A. Okada, Y. Takeuchi, K. Furuya, C. Zhang, H. Sato, S. Fukami, and H. Ohno, "Spin-pumping-free determination of spin-orbit torque efficiency from spin-torque ferromagnetic resonance," *Phys. Rev. Applied*, vol. 12, p. 014040, Jul 2019.

[7] K. Lee, A. H. Dismukes, E. J. Telford, R. A. Wiscons, J. Wang, X. Xu, C. Nuckolls, C. R. Dean, X. Roy, and X. Zhu, "Magnetic order and symme-

try in the 2d semiconductor CrSBr," *Nano Letters*, vol. 21, pp. 3511–3517, Apr 2021.

[8] L. Liu, T. Moriyama, D. C. Ralph, and R. A. Buhrman, "Spin-torque ferromagnetic resonance induced by the spin Hall effect," *Phys. Rev. Lett.*, vol. 106, p. 036601, Jan 2011.

[9] Y. Tserkovnyak, A. Brataas, and G. E. W. Bauer, "Enhanced Gilbert damping in thin ferromagnetic films," *Phys. Rev. Lett.*, vol. 88, p. 117601, Feb 2002.

[10] O. Mosendz, V. Vlaminck, J. E. Pearson, F. Y. Fradin, G. E. W. Bauer, S. D. Bader, and A. Hoffmann, "Detection and quantification of inverse spin Hall effect from spin pumping in permalloy/normal metal bilayers," *Phys. Rev. B*, vol. 82, p. 214403, Dec 2010.

[11] S. Karimeddiny, J. A. Mittelstaedt, R. A. Buhrman, and D. C. Ralph, "Transverse and longitudinal spin-torque ferromagnetic resonance for improved measurement of spin-orbit torque," *Physical Review Applied*, vol. 14, Aug 2020.

[12] X. Fan, H. Celik, J. Wu, C. Ni, K.-J. Lee, V. O. Lorenz, and J. Q. Xiao, "Quantifying interface and bulk contributions to spin-orbit torque in magnetic bilayers," *Nature Communications*, vol. 5, no. 1, p. 3042, 2014.

[13] A. Tulapurkar, Y. Suzuki, A. Fukushima, H. Kubota, H. Maehara, K. Tsunekawa, D. Djayaprawira, N. Watanabe, and S. Yuasa, "Spin-torque diode effect in magnetic tunnel junctions," *Nature*, vol. 438, pp. 339–342, November 2005.

[14] J. C. Sankey, P. M. Braganca, A. G. F. Garcia, I. N. Krivorotov, R. A. Buhrman, and D. C. Ralph, "Spin-transfer-driven ferromagnetic resonance of individual nanomagnets," *Phys. Rev. Lett.*, vol. 96, p. 227601, Jun 2006.

[15] Y. Tserkovnyak, A. Brataas, and G. E. W. Bauer, "Spin pumping and magnetization dynamics in metallic multilayers," *Phys. Rev. B*, vol. 66, p. 224403, Dec 2002.

[16] A. Azevedo, L. H. Vilela-Leão, R. L. Rodríguez-Suárez, A. F. Lacerda Santos, and S. M. Rezende, "Spin pumping and anisotropic magnetoresistance voltages in magnetic bilayers: Theory and experiment," *Phys. Rev. B*, vol. 83, p. 144402, Apr 2011.

[17] K.-i. Uchida, H. Adachi, T. Ota, H. Nakayama, S. Maekawa, and E. Saitoh, "Observation of longitudinal spin-Seebeck effect in magnetic insulators," *Applied Physics Letters*, vol. 97, no. 17, p. 172505, 2010.

[18] J. Lustikova, Y. Shiomi, and E. Saitoh, "Vector spectroscopy for spin pumping," *Phys. Rev. B*, vol. 92, p. 224436, Dec 2015.

[19] M. B. Jungfleisch, A. V. Chumak, A. Kehlberger, V. Lauer, D. H. Kim, M. C. Onbasli, C. A. Ross, M. Kläui, and B. Hillebrands, "Thickness and power dependence of the spin-pumping effect in $Y_3Fe_5O_{12}$/Pt heterostructures measured by the inverse spin Hall effect," *Phys. Rev. B*, vol. 91, p. 134407, Apr 2015.

[20] H. Nakayama, K. Ando, K. Harii, T. Yoshino, R. Takahashi, Y. Kajiwara, K. Uchida, Y. Fujikawa, and E. Saitoh, "Geometry dependence on inverse spin Hall effect induced by spin pumping in $Ni_{81}Fe_{19}$/Pt films," *Phys. Rev. B*, vol. 85, p. 144408, Apr 2012.

[21] S. M. Rezende, R. L. Rodríguez-Suárez, R. O. Cunha, A. R. Rodrigues, F. L. A. Machado, G. A. Fonseca Guerra, J. C. Lopez Ortiz, and A. Azevedo, "Magnon spin-current theory for the longitudinal spin-Seebeck effect," *Phys. Rev. B*, vol. 89, p. 014416, Jan 2014.

[22] J. Holanda, O. Alves Santos, R. L. Rodríguez-Suárez, A. Azevedo, and S. M. Rezende, "Simultaneous spin pumping and spin Seebeck experiments

with thermal control of the magnetic damping in bilayers of yttrium iron garnet and heavy metals: YIG/Pt and YIG/IrMn," *Phys. Rev. B*, vol. 95, p. 134432, Apr 2017.

[23] N. Roschewsky, E. S. Walker, P. Gowtham, S. Muschinske, F. Hellman, S. R. Bank, and S. Salahuddin, "Spin-orbit torque and Nernst effect in Bi-Sb/Co heterostructures," *Phys. Rev. B*, vol. 99, p. 195103, May 2019.

[24] E. Saitoh, M. Ueda, H. Miyajima, and G. Tatara, "Conversion of spin current into charge current at room temperature: Inverse spin-Hall effect," *Applied Physics Letters*, vol. 88, no. 18, p. 182509, 2006.

[25] R. Iguchi and E. Saitoh, "Measurement of spin pumping voltage separated from extrinsic microwave effects," *Journal of the Physical Society of Japan*, vol. 86, no. 1, p. 011003, 2017.

[26] K. Kondou, H. Sukegawa, S. Kasai, S. Mitani, Y. Niimi, and Y. Otani, "Influence of inverse spin Hall effect in spin-torque ferromagnetic resonance measurements," *Applied Physics Express*, vol. 9, p. 023002, Jan 2016.

[27] A. Kumar, S. Akansel, H. Stopfel, M. Fazlali, J. Åkerman, R. Brucas, and P. Svedlindh, "Spin transfer torque ferromagnetic resonance induced spin pumping in the Fe/Pd bilayer system," *Phys. Rev. B*, vol. 95, p. 064406, Feb 2017.

[28] C. O. Avci, K. Garello, M. Gabureac, A. Ghosh, A. Fuhrer, S. F. Alvarado, and P. Gambardella, "Interplay of spin-orbit torque and thermoelectric effects in ferromagnet/normal-metal bilayers," *Phys. Rev. B*, vol. 90, p. 224427, Dec 2014.

[29] A. Bose, S. Dutta, S. Bhuktare, H. Singh, and A. A. Tulapurkar, "Sensitive measurement of spin-orbit torque driven ferromagnetic resonance detected by planar Hall geometry," *Applied Physics Letters*, vol. 111, no. 16, p. 162405, 2017.

[30] S. Keller, J. Greser, M. R. Schweizer, A. Conca, V. Lauer, C. Dubs, B. Hillebrands, and E. T. Papaioannou, "Relative weight of the inverse spin-Hall and spin-rectification effects for metallic polycrystalline py/pt, epitaxial Fe/Pt, and insulating YIG/Pt bilayers: Angular dependent spin pumping measurements," *Physical Review B*, vol. 96, Jul 2017.

[31] M. Harder, Y. Gui, and C.-M. Hu, "Electrical detection of magnetization dynamics via spin rectification effects," *Physics Reports*, vol. 661, pp. 1–59, Nov 2016.

[32] N. Vlietstra, J. Shan, V. Castel, B. J. van Wees, and J. Ben Youssef, "Spin-Hall magnetoresistance in platinum on yttrium iron garnet: Dependence on platinum thickness and in-plane/out-of-plane magnetization," *Phys. Rev. B*, vol. 87, p. 184421, May 2013.

[33] M. Hayashi, J. Kim, M. Yamanouchi, and H. Ohno, "Quantitative characterization of the spin-orbit torque using harmonic Hall voltage measurements," *Phys. Rev. B*, vol. 89, p. 144425, Apr 2014.

[34] S. Mizukami, Y. Ando, and T. Miyazaki, "The study on ferromagnetic resonance linewidth for NM/80NiFe/NM (NM=Cu, Ta, Pd and Pt) films," *Japanese Journal of Applied Physics*, vol. 40, pp. 580–585, Feb 2001.

[35] A. Brataas, Y. Tserkovnyak, G. E. W. Bauer, and P. J. Kelly, "Spin pumping and spin transfer," *arXiv:1108.0385*, 2011.

[36] T. Kikkawa, K. Uchida, Y. Shiomi, Z. Qiu, D. Hou, D. Tian, H. Nakayama, X.-F. Jin, and E. Saitoh, "Longitudinal spin Seebeck effect free from the proximity Nernst effect," *Phys. Rev. Lett.*, vol. 110, p. 067207, Feb 2013.

[37] C.-F. Pai, Y. Ou, L. H. Vilela-Leão, D. C. Ralph, and R. A. Buhrman, "Dependence of the efficiency of spin Hall torque on the transparency of Pt/ferromagnetic layer interfaces," *Phys. Rev. B*, vol. 92, p. 064426, Aug 2015.

[38] M. Schreier, G. E. W. Bauer, V. I. Vasyuchka, J. Flipse, K. ichi Uchida, J. Lotze, V. Lauer, A. V. Chumak, A. A. Serga, S. Daimon, T. Kikkawa, E. Saitoh, B. J. van Wees, B. Hillebrands, R. Gross, and S. T. B. Goennenwein, "Sign of inverse spin Hall voltages generated by ferromagnetic resonance and temperature gradients in yttrium iron garnet platinum bilayers," *Journal of Physics D: Applied Physics*, vol. 48, p. 025001, Dec 2014.

[39] X. Fan, J. Wu, Y. Chen, M. J. Jerry, H. Zhang, and J. Q. Xiao, "Observation of the nonlocal spin-orbital effective field," *Nature Communications*, vol. 4, no. 1, p. 1799, 2013.

[40] T. Nan, S. Emori, C. T. Boone, X. Wang, T. M. Oxholm, J. G. Jones, B. M. Howe, G. J. Brown, and N. X. Sun, "Comparison of spin-orbit torques and spin pumping across NiFe/Pt and NiFe/Cu/Pt interfaces," *Physical Review B*, vol. 91, Jun 2015.

[41] L. Zhu, D. C. Ralph, and R. A. Buhrman, "Effective spin-mixing conductance of heavy-metal–ferromagnet interfaces," *Phys. Rev. Lett.*, vol. 123, p. 057203, Aug 2019.

[42] M.-H. Nguyen, D. C. Ralph, and R. A. Buhrman, "Spin torque study of the spin Hall conductivity and spin diffusion length in platinum thin films with varying resistivity," *Phys. Rev. Lett.*, vol. 116, p. 126601, Mar 2016.

[43] R. Iguchi, K. Ando, R. Takahashi, T. An, E. Saitoh, and T. Sato, "Spin pumping without three-magnon splitting in polycrystalline $Bi_1Y_2Fe_5O_{12}$/Pt bilayer structure," *Japanese Journal of Applied Physics*, vol. 51, p. 103004, Oct 2012.

[44] K.-U. Demasius, T. Phung, W. Zhang, B. P. Hughes, S.-H. Yang, A. Kellock, W. Han, A. Pushp, and S. S. P. Parkin, "Enhanced spin–orbit

torques by oxygen incorporation in tungsten films," *Nature Communications*, vol. 7, Feb 2016.

[45] J.-W. Xu and A. D. Kent, "Charge-to-spin conversion efficiency in ferromagnetic nanowires by spin torque ferromagnetic resonance: Reconciling lineshape and linewidth analysis methods," *Physical Review Applied*, vol. 14, Jul 2020.

[46] S. Karimeddiny and D. C. Ralph, "Resolving discrepancies in spin-torque ferromagnetic resonance measurements: Lineshape versus linewidth analyses," *Phys. Rev. Applied*, vol. 15, p. 064017, Jun 2021.

[47] L. Liu, C.-F. Pai, Y. Li, H. W. Tseng, D. C. Ralph, and R. A. Buhrman, "Spin-torque switching with the giant spin Hall effect of tantalum," *Science*, vol. 336, no. 6081, pp. 555–558, 2012.

[48] A. M. Gonçalves, I. Barsukov, Y.-J. Chen, L. Yang, J. A. Katine, and I. N. Krivorotov, "Spin torque ferromagnetic resonance with magnetic field modulation," *Applied Physics Letters*, vol. 103, p. 172406, Oct 2013.

[49] W. Skowroński, T. Nozaki, Y. Shiota, S. Tamaru, K. Yakushiji, H. Kubota, A. Fukushima, S. Yuasa, and Y. Suzuki, "Perpendicular magnetic anisotropy of Ir/CoFeB/MgO trilayer system tuned by electric fields," *Applied Physics Express*, vol. 8, p. 053003, Apr 2015.

[50] C. J. Safranski, Y.-J. Chen, I. N. Krivorotov, and J. Z. Sun, "Material parameters of perpendicularly magnetized tunnel junctions from spin torque ferromagnetic resonance techniques," *Applied Physics Letters*, vol. 109, p. 132408, Sep 2016.

[51] C. Safranski, E. A. Montoya, and I. N. Krivorotov, "Spin–orbit torque driven by a planar Hall current," *Nature Nanotechnology*, vol. 14, pp. 27–30, Oct 2018.

[52] Y.-J. Chen, H. K. Lee, R. Verba, J. A. Katine, I. Barsukov, V. Tiberkevich, J. Q. Xiao, A. N. Slavin, and I. N. Krivorotov, "Parametric resonance of magnetization excited by electric field," *Nano Letters*, vol. 17, pp. 572–577, Dec 2016.

[53] D. MacNeill, G. M. Stiehl, M. H. D. Guimarães, N. D. Reynolds, R. A. Buhrman, and D. C. Ralph, "Thickness dependence of spin-orbit torques generated by WTe_2," *Physical Review B*, vol. 96, Aug 2017.

[54] M. Harder, Z. X. Cao, Y. S. Gui, X. L. Fan, and C.-M. Hu, "Analysis of the line shape of electrically detected ferromagnetic resonance," *Phys. Rev. B*, vol. 84, p. 054423, Aug 2011.

[55] J. Z. Sun, "Resistance-area product and size dependence of spin-torque switching efficiency in CoFeB-MgO based magnetic tunnel junctions," *Phys. Rev. B*, vol. 96, p. 064437, Aug 2017.

[56] C. Safranski and J. Sun, "Interface moment dynamics and its contribution to spin-transfer torque switching process in magnetic tunnel junctions," *Phys. Rev. B*, vol. 100, p. 014435, Jul 2019.

[57] S. Woo, M. Mann, A. J. Tan, L. Caretta, and G. S. D. Beach, "Enhanced spin-orbit torques in Pt/Co/Ta heterostructures," *Applied Physics Letters*, vol. 105, no. 21, p. 212404, 2014.

[58] J. Torrejon, J. Kim, J. Sinha, S. Mitani, M. Hayashi, M. Yamanouchi, and H. Ohno, "Interface control of the magnetic chirality in CoFeB/MgO heterostructures with heavy-metal underlayers," *Nature Communications*, vol. 5, p. 4655, Aug 2014.

[59] L. Zhu, D. C. Ralph, and R. A. Buhrman, "Spin-orbit torques in heavy-metal–ferromagnet bilayers with varying strengths of interfacial spin-orbit coupling," *Phys. Rev. Lett.*, vol. 122, p. 077201, Feb 2019.

[60] S. Karimeddiny, T. M. Cham, D. C. Ralph, and Y. K. Luo, "Sagnac interferometry for high-sensitivity optical measurements of spin-orbit torque," 2021.

[61] J. Xia, P. T. Beyersdorf, M. M. Fejer, and A. Kapitulnik, "Modified Sagnac interferometer for high-sensitivity magneto-optic measurements at cryogenic temperatures," *Applied Physics Letters*, vol. 89, no. 6, p. 062508, 2006.

[62] J. Xia, Y. Maeno, P. T. Beyersdorf, M. M. Fejer, and A. Kapitulnik, "High resolution polar kerr effect measurements of Sr_2RuO_4: Evidence for broken time-reversal symmetry in the superconducting state," *Phys. Rev. Lett.*, vol. 97, p. 167002, Oct 2006.

[63] A. Fried, M. Fejer, and A. Kapitulnik, "A scanning, all-fiber Sagnac interferometer for high resolution magneto-optic measurements at 820 nm," *Review of Scientific Instruments*, vol. 85, no. 10, p. 103707, 2014.

[64] D. Ralph and M. Stiles, "Spin transfer torques," *Journal of Magnetism and Magnetic Materials*, vol. 320, no. 7, pp. 1190–1216, 2008.

[65] C. Gong, L. Li, Z. Li, H. Ji, A. Stern, Y. Xia, T. Cao, W. Bao, C. Wang, Y. Wang, Z. Q. Qiu, R. J. Cava, S. G. Louie, J. Xia, and X. Zhang, "Discovery of intrinsic ferromagnetism in two-dimensional van der Waals crystals," *Nature*, vol. 546, pp. 265–269, Jun 2017.

[66] L. Zhu, K. Sobotkiewich, X. Ma, X. Li, D. C. Ralph, and R. A. Buhrman, "Strong damping-like spin-orbit torque and tunable dzyaloshinskii–moriya interaction generated by low-resistivity Pd_{1-x} Pt_x alloys," *Advanced Functional Materials*, vol. 29, p. 1805822, Feb 2019.

[67] Y. Ou, C.-F. Pai, S. Shi, D. C. Ralph, and R. A. Buhrman, "Origin of fieldlike spin-orbit torques in heavy metal/ferromagnet/oxide thin film heterostructures," *Physical Review B*, vol. 94, Oct 2016.

[68] K. Yasuda, A. Tsukazaki, R. Yoshimi, K. Kondou, K. S. Takahashi, Y. Otani, M. Kawasaki, and Y. Tokura, "Current-nonlinear Hall effect and spin-orbit torque magnetization switching in a magnetic topological insulator," *Phys. Rev. Lett.*, vol. 119, p. 137204, Sep 2017.

[69] P. He, S. S.-L. Zhang, D. Zhu, S. Shi, O. G. Heinonen, G. Vignale, and H. Yang, "Nonlinear planar Hall effect," *Phys. Rev. Lett.*, vol. 123, p. 016801, Jul 2019.

[70] H.-R. Lee, K. Lee, J. Cho, Y.-H. Choi, C.-Y. You, M.-H. Jung, F. Bonell, Y. Shiota, S. Miwa, and Y. Suzuki, "Spin-orbit torque in a bulk perpendicular magnetic anisotropy Pd/FePd/MgO system," *Scientific Reports*, vol. 4, p. 6548, Oct 2014.

[71] Y.-C. Lau and M. Hayashi, "Spin torque efficiency of Ta, W, and Pt in metallic bilayers evaluated by harmonic Hall and spin Hall magnetoresistance measurements," *Japanese Journal of Applied Physics*, vol. 56, p. 0802B5, Jun 2017.